Neutral Kaon Correlations in Au-Au Collisions at Center of Mass Energy of 200 GeV per Nucleon Pair

DISSERTATION

Presented in Partial Fulfillment of the Requirements for

the Degree Doctor of Philosophy in the

Graduate School of The Ohio State University

By

SELEMON BEKELE, B. Sc., M. Sc.

* * * * *

The Ohio State University

2004

Dissertation Committee:

Professor Thomas J. Humanic, Adviser

Professor Michael A. Lisa

Professor Richard J. Furnstahl

Professor Richard D. Kass

Professor Steven A. Lavender

Approved by

Adviser

Department of Physics

ABSTRACT

A few microseconds after the Big Bang, the universe is believed to have existed in the form of a plasma composed of strongly interacting particles known as quarks and gluons. Although the quarks and gluons behave as asymptotically free particles in a Quark Gluon Plasma (QGP), free quarks and gluons have never been discovered in the laboratory. Experiments at the Relativistic Heavy Ion Collider (RHIC) aim to create conditions similar to the early universe by colliding heavy ions at the highest energies possible in the hope of observing a phase transition from a QGP into hadronic degrees of freedom.

The response of the space time structure of the hot reaction zone created in a heavy ion collision to a phase transition is one of the many observables being studied at RHIC. Making use of the techniques of two particle intensity interferometry, also known as the HBT effect, the RHIC experiments are studying the space-time structure and dynamical properties of the region from which particles are emitted. A large spatial size and long duration of particle emission are the predicted signals for a phase transition from a QGP to a hadronic phase.

In this thesis we present results on the first measurement of one dimensional $K^0_s K^0_s$ interferometry by the STAR experiment at RHIC in central (small impact parameter) Au-Au collisions at center of mass energy 200 GeV per nucleon pair. The λ parameter, which is a measure of the sources chaoticity, is found to be consistent with unity

confirming the fact that the source is mostly chaotic as measured by STAR using three particle correlations. Without taking into account the effect of the strong interaction, the invariant radius R_{inv} is found to be large for the mean transverse mass (M_t) of the pair, which is about 980 MeV/c, compared to expectations from charged pion correlations at the same M_t. Including the effect of the strong interactions makes the radius parameter for the $K^0_s K^0_s$ system fall within the charged pion M_t systematics. Our result serves as a valuable cross-check of charged pion measurements which are mainly affected by contributions from resonance decays and final state interactions. This is also an important first step towards a full three dimensional analysis of neutral kaon correlations as high statistics data from RHIC will be available in the near future.

Dedicated to my parents,

Ato Bekele Gadissa and W/ro Mulunesh Mekonnen

ACKNOWLEDGMENTS

I would like to thank, above all, God Almighty for seeing me through my studies and being with me through the ups and downs of my life. This work would not have been possible without the support and encouragement of may people.

My heartfelt thanks go to my family for their constant encouragement and advice and for keeping me in their prayers all these years. I owe my father, Ato Bekele Gadissa, for his dream twenty years ago that one day I would be where I am today.

Especial thanks go to members of the PENIEL Ethiopian Evangelical Church for their spiritual and social support throughout my stay in school. I extend my deepest gratitude to my dear friends of the Friday Prayer Group, Aklilu Kassa, Yeshi Negash, Tesfu Mesghenna, Meron Bereket, Elfaz Tekola, Zewdie Bachore, Azalech Gebreab, Anchinalu Arage and Naomi Yosef for their prayers, thoughtfulness and support making me feel at home and cope with my difficult times gracefully.

My warmest thanks go to all my friends, especially Negussie Tirfessa and Mesfin Tsige, for their encouragement, understanding and patience during my school days at OSU.

I am very grateful to members of the SVT group, each of whom contributed to my knowledge about the inner workings of the detector. It was a privilege working with Helen Caines and Marcelo Munhoz, Jun Takahashi and Robert Willson from whom I learned a lot while working on the data analysis software project for the SVT. Many

thanks go to Vladimir Rykov for his continual support while I was involved with the SVT group.

My deepest gratitude to my advisor, Tom Humanic, for keeping me motivated to study Heavy Ion Physics, for giving me his valuable time when I have questions and needed guidance. I offer my sincere thanks to Mike Lisa, Sergey Panitkin and other members of the HBT physics working group for their unreserved help while learning Intensity interferometry. I would also like to thank Lanny Ray for his input to my understanding of the theoretical aspects of neutral kaon correlations.

I also thank the people at the Van de Graff laboratory, Mary Smith, Florence Shanks, Howard Dike, Ivan Kotov, Bjorn Neilson. Special thanks to Mercedes Lopez Noriega and Randy Wells for making my stay in Smith Lab a wonderful experience.

VITA

May 16, 1967	Born -Addis Ababa, Ethiopia
1987	B. Sc. Physics Addis Ababa University Addis Ababa, Ethiopia
1995	M. Sc. Physics Addis Ababa University Addis Ababa, Ethiopia
1997-2000	Graduate Teaching Assistant Department of Physics The Ohio State University Columbus, OH
2001-present	Graduate Research Associate Department of Physics The Ohio State University Columbus, OH

PUBLICATIONS

Research Publications

Selemon Bekele (STAR Collaboration), "Charged and neutral kaon correlations in Au-Au collisions at $\sqrt{s_{NN}} = 130$ GeV. using the solenoidal tracker at RHIC (STAR)." *J. Phys. G: Nucl. Part. Phys*, **30** (2004), 229

STAR Collaboration (J. Adams et al.) "Azimuthally sensitive HBT in Au+Au collisions at $\sqrt{s_{NN}} = 200$ GeV." *Submitted to Physical Review Letters, (nucl-ex/0312009)*

STAR Collaboration (J. Adams et al.) "Production of Charged Pions and Hadrons in Au+Au Collisions at $\sqrt{(}s_N N) = 130$ GeV." *Submitted to Physical Review C, (nucl-ex/0311017)*

STAR Collaboration (J. Adams et al.) "Azimuthal anisotropy at RHIC: the first and fourth harmonics." *Submitted to Physical Review Letters, (nucl-ex/0310029)*

STAR Collaboration (J. Adams et al.) "Cross Sections and Transverse Single-Spin Asymmetries in Forward Neutral Pion Production from Proton Collisions at $\sqrt{s_{NN}} =$ 200 GeV." *Submitted to Physical Review Letters, (hep-ex/0310058)*

STAR Collaboration (J. Adams et al.) "Identified particle distributions in pp and Au+Au collisions at $\sqrt{s_{NN}} = 200$ GeV." *Submitted to Physical Review Letters, (nucl-ex/0310004)*

STAR Collaboration (J. Adams et al.) "Pion, kaon, proton and anti-proton transverse momentum distributions from p+p and d+Au collisions at $\sqrt{s_{NN}} = 200$ GeV." *Submitted to Physical Review Letters, (nucl-ex/0309012)*

STAR Collaboration (J. Adams et al.) "Event-by-Event (pt) fluctuations in Au-Au collisions at $\sqrt{s_{NN}} = 130$ GeV." *Submitted to Physical Review Letters, (nucl-ex/0308033)*

STAR Collaboration (J. Adams et al.) "Multi-strange baryon production in Au-Au collisions at $\sqrt{s_{NN}} = 130$ GeV." *Submitted to Physical Review Letters, (nucl-ex/0307024)*

STAR Collaboration (J. Adams et al.) "Pion-Kaon Correlations in Central Au+Au Collisions at $\sqrt{s_{NN}} = 130$ GeV ." *Phys. Rev. Lett.* , **91** (2003) 262302

STAR Collaboration (J. Adams et al.) "ρ^0 Production and Possible Modification in Au+Au and p+p Collisions at $\sqrt{s_{NN}} = 200$ GeV." *Submitted to Physical Review Letters, (nucl-ex/0307023)*

STAR Collaboration (J. Adams et al.) "Net charge fluctuations in Au+Au collisions at $\sqrt{s_{NN}} = 130$ GeV ." *Phys. Rev. C* , **68** (2003) 044905

STAR Collaboration (J. Adams et al.) "Rapidity and Centrality Dependence of Proton and Anti-proton Production from Au+Au Collisions at $\sqrt{s_{NN}} = 130$ GeV ." *Submitted to Physical Review Letters, (nucl-ex/0306029)*

STAR Collaboration (J. Adams et al.) "Three-Pion Hanbury Brown-Twiss Correlations in Relativistic Heavy-Ion Collisions from the STAR Experiment." *Phys. Rev. Lett.* , **91** (2003) 262301

STAR Collaboration (J. Adams et al.) "Evidence from d+Au measurements for final-state suppression of high pT hadrons in Au+Au collisions at RHIC." *Phys. Rev. Lett.* , **91** (2003) 072304

STAR Collaboration (J. Adams et al.) "Particle dependence of azimuthal anisotropy and nuclear modification of particle production at moderate pT in Au+Au collisions at $\sqrt{s_{NN}} = 200$ GeV." *Submitted to Physical Review Letters, (nucl-ex/0306007)*

STAR Collaboration (J. Adams et al.) "Transverse momentum and collision energy dependence of high pT hadron suppression in Au+Au collisions at ultra-relativistic energies ." *Phys. Rev. Lett.* , **91** (2003) 172302

STAR Collaboration (J. Adams et al.) "Narrowing of the Balance Function with Centrality in Au+Au Collisions at $\sqrt{s_{NN}} = 130$ GeV ." *Phys. Rev. Lett.* , **90** (2003) 172301

STAR Collaboration (J. Adams et al.) "Strange anti-particle to particle ratios at mid-rapidity in $\sqrt{s_{NN}} = 130$ GeV Au + Au collisions." *Phys. Lett. B* , **567** (2003) 167

STAR Collaboration (J. Adams et al.) "Disappearance of back-to-back high pT hadron correlations in central Au + Au collisions at $\sqrt{s_{NN}} = 200$ GeV *Phys. Rev. Lett.* , **90** (2003) 082302

STAR Collaboration (C. Adler et al.) "Centrality Dependence of High pT Hadron Suppression in Au + Au ." Collisions at $\sqrt{s_{NN}} = 130$ GeV ." *Phys. Rev. Lett.* , **89** (2002) 202301

STAR Collaboration (C. Adler et al.) "Kaon Production and Kaon to Pion Ratio in Au + Au Collisions at $\sqrt{s_{NN}} = 130$ GeV." *Submitted June 13, 2002 (nucl-ex/0206008)*

STAR Collaboration (C. Adler et al.) "Azimuthal Anisotropy and Correlations in the Hard Scattering Regime at RHIC." *Phys. Rev. Lett.* , **90** (2003) 032301

STAR Collaboration (C. Adler et al.) "Coherent Rho-zero Production in Ultra-Peripheral Heavy Ion Collisions." *Phys. Rev. Lett.* , **89** (2002) 272302

STAR Collaboration (C. Adler et al.) "Elliptic flow from two- and four-particle correlations in Au + Au collisions at $\sqrt{s_{NN}} = 130$ GeV." *Phys. Rev. C* , **66** (2002) 034904

STAR Collaboration (C. Adler et al.) "Azimuthal anisotropy of K0s and Lambda + Lambda bar production at mid-rapidity from Au+Au collisions at $\sqrt{s_{NN}} = 130$ GeV." *Phys. Rev. Lett.* , **89** (2002) 132301

STAR Collaboration (C. Adler et al.) "K*(892)0 Production in Relativistic Heavy Ion Collisions at $\sqrt{s_{NN}} = 130$ GeV." *Phys. Rev. C* , **66** (2002) 061901(R)

STAR Collaboration (C. Adler et al.) "Mid-rapidity Lambda and Lambda bar Production in Au + Au Collisions at $\sqrt{s_{NN}} = 130$ GeV." *Phys. Rev. Lett.* , **89** (2002) 092301

STAR Collaboration (C. Adler et al.) "Measurement of inclusive antiprotons from Au+Au collisions at $\sqrt{s_{NN}} = 130$ GeV." *Phys. Rev. Lett.* , **87** (2001) 262302

STAR Collaboration (C. Adler et al.) "Antideuteron and Antihelium production in Au+Au collisions at $\sqrt{s_{NN}} = 130$ GeV ." *Phys. Rev. Lett.* , **87** (2001) 262301

STAR Collaboration (C. Adler et al.) "Mid-rapidity phi production in Au+Au collisions at $\sqrt{s_{NN}} = 130$ GeV ." *Phys. Rev. C* , **65** (2002) 041901(R)

STAR Collaboration (C. Adler et al.) "Multiplicity distribution and spectra of negatively charged hadrons in Au+Au collisions at $\sqrt{s_{NN}} = 130$ GeV." *Phys. Rev. Lett.* , **87** (2001) 112303

STAR Collaboration (C. Adler et al.) "Pion Interferometry of $\sqrt{s_{NN}} = 130$ GeV Au+Au collisions at RHIC." *Phys. Rev. Lett.* , **87** (2001) 082301

STAR Collaboration (C. Adler et al.) "Identified Particle Elliptic Flow in Au+Au Collisions at $\sqrt{s_{NN}} = 130$ GeV." *Phys. Rev. Lett.* , **87** (2001) 182301

STAR Collaboration (C. Adler et al.) "Mid-rapidity Antiproton-to-Proton Ratio from Au+Au $\sqrt{s_{NN}} = 130$ GeV." *Phys. Rev. Lett.* , **86** (2001) 4778

STAR Collaboration (K.H. Ackermann et al.) "Elliptic Flow in Au+Au Collisions at $\sqrt{s_{NN}} = 130$ GeV ." *Phys. Rev. Lett.* , **86** (2001) 402

Major Field: Physics

Studies in Experimental Nuclear Physics: Professor Thomas J. Humanic

TABLE OF CONTENTS

LIST OF TABLES

LIST OF FIGURES

CHAPTER 1

INTRODUCTION

According to modern cosmology, the Universe is believed to have emerged from a singular space-time configuration and developed from this initial state with an extremely high energy density in a massive explosion known as the Big Bang [1, 2]. Backward extrapolation of the development of the universe comes to an end at the so-called Planck time $t_p = \sqrt{\hbar G/c^5} = 5.4X10^{-44}s$ when the temperature corresponded to the Plank mass $m_p = 1.2X10^{19}$ GeV$/c^2$ Current theories cannot describe events prior to this time which require a quantum theory of gravitation that is not yet available. A schematic diagram depicting the evolution of the universe is shown in Figure (1.1).

The energy density at the Planck time was so large that no symmetry breaking had yet occurred. The particles were all massless, or, at least, the masses at this early time could be neglected. One could then think of the universe as consisting of an ideal gas of massless particles in thermodynamic equilibrium. The interaction between the particles had just divided into gravitation and a GUT interaction which may be represented by an SU(5)(or higher) symmetry group. The decrease in thermal energy as a result of expansion led to symmetry breakings at different points in time in the universe's evolution. Every time a symmetry is broken particles obtained mass and

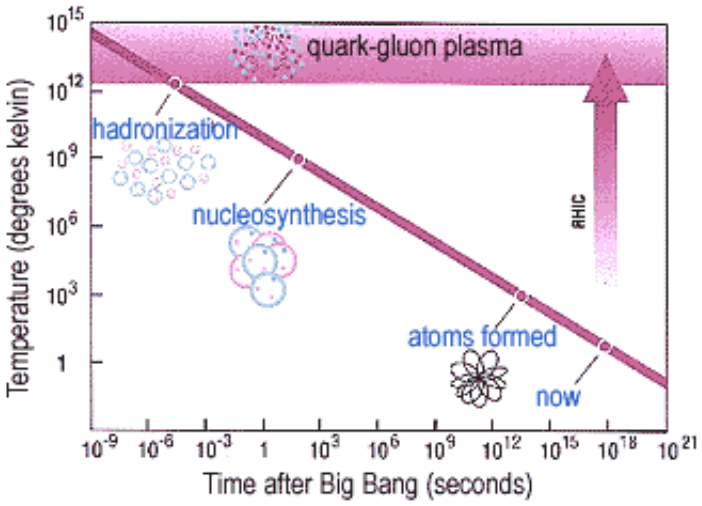

Figure 1.1: A schematic diagram showing the evolution of the universe from the Big bang time to the present.

froze out of thermodynamic equilibrium. For example, in the period between $10^{-36}s$ and $10^{-10}s$ after the Big Bang, the universe was considered to be a soup of massless leptons, quarks, W and Z bosons and photons, together with other hypothetical particles such as Higgs bosons etc. After $10^{-10}s$, the universe had already grown to a size of 10^{14} cm and cooled to an energy around 100 GeV, so that spontaneous breaking of the $SU(2)_L$ X $U(1)$ symmetry occurred. As a result of this, the massless particles mentioned above obtained their effective masses and the heavy W and Z bosons froze out of the thermodynamic equilibrium. After approximately $10^{-6}s$, the quark-gluon plasma which was present until then could no longer be supported by the thermal energy which was then $kT = 1$ GeV. A phase transition from a quark-gluon plasma to the quark confinement took place, i.e mesons and baryons were formed.

Ultra-relativistic heavy-ion collisions in accelerator experiments are being used to create matter with a very high energy density and study its properties. Of particular interest is the possibility of a phase transition into a quark gluon plasma(QGP). Over the past 20 years high energy nuclear and particle physicists have been using high energy collider experiments to recreate this kind of matter in the laboratory and a tremendous amount of theoretical and experimental research has been going to understand the equation of state of nuclear matter at high temperatures and densities.

Collider experiments usually employ several detector systems capable of taking data simulataneously or individually. One of the main tasks of experimental physicists is thus to make sure that their experimental apparatus work properly to meet their design objectives. Detector simulation is thus an integral part of the data analysis effort in high energy heavy ion collision experiments which rely on charged particle tracking beginning with the hits they leave behind on the detectors. This thesis presents results from C++ codes that have been developed for a SLOW SIMULATOR that generates hits and calculates the evolution of their signals and a CLUSTER FINDER which reconstructs the hits formed by a track crossing the Silicon Vertex Tracker (SVT) which is one of the subsystems of the STAR detector. The codes offer the capability to study tracking efficiency, position resolution, effects of diffusion, Coulomb repulsion, trapping and detrapping processes.

Once the detector properties are understood, the next step is to perform detailed data analysis studying observables pertinent to the experimental goals at hand. One of the many observables being studied by experiments at the Relativistic Heavy Ion Collider (RHIC) is the space time structure of the hot reaction zone and its response to a phase transition. A delayed expansion of the reaction zone as a result of a phase

transition into a hadronic phase, and hence a large spatial size and long duration of particle emission, is one of the many predicted signatures of QGP formation.

Two particle intensity interferometry provides a means of determining the space-time structure and dynamical properties of the region from which particles are emitted. The method relies on the symmetrization (anti-symmetrization) of the two particle wave function if the particles are bosons (fermions). In addition to the interference arising from this quantum statistics effect, correlations can come from final state interactions like Coulomb repulsion or strong interaction which complicates analysis of charged particle correlations.

Traditionally, charged pions have been used in correlation studies due to their abundance even though resonances contribute almost half of the pions produced in heavy ion collisions. Thus, resonance decays and final state Coulomb interaction make it difficult to extract the desired information about the space time structure of the particle source in heavy ion collisions. Neutral kaons, however, suffer less from resonance decays and Coulomb interaction is absent for them. As a result, it is expected that neutral kaon correlations give more reliable information than the pions.

This thesis presents the first measurement on neutral kaon ($K_s^0 K_s^0$) correlations in heavy ion collisions. Owing to a lack of sufficient statistics, only one dimensional correlations have been studied. The invariant radius parameter, R_{inv}, extracted from the data has been found to be large compared to what is expected from identical pion correlations at the same transverse momentum if one ignores the effect of the strong interaction. A simulation of the strong interaction effect indicates that the apparent source size obtained if one considers strong interaction is bigger than the size one would get by neglecting it. Indeed, taking into account the strong interaction, the

value of R_{inv} falls within the systematics of identical pion correlation measurements. The value of the chaoticity parameter, λ, has been found to be consistent with unity confirming the fact that the source is mostly chaotic as measured by the Solenoidal Tracker At RHIC (STAR) using three pion correlations [3]. This work lays the ground work for a full three dimensional analysis of $K_s^0 K_s^0$ interferometry with the coming high statistics data from RHIC. These results also serve as a valuable cross-check of charged pion measurements which are mainly affected by contributions from resonance decays and final state interactions.

The remainder of the thesis is organized as follows. A review of the quark model, the parton model and QCD is given Chapter 2. A brief discussion of some of the potential signatures for QGP formation is presented in Chapter 3. The thermodynamics of the QGP is considered in Chapter 4 along with some results from Lattice QCD regarding the phase transition from a QGP to a hadronic gas phase. In Chapters 5, the theoretical background to identical interferometry is provided and Chapter 6 gives the theory behind neutral kaon correlations. A brief introduction to sme of the detectors at Relativistic Heavy Ion Collider (RHIC) is given in Chapter 7. The work I have done for the SVT detector, is presented in Chapter 8. Chapter 9 gives results from my data analysis of the $K_s^0 K_s^0$ interferometry measurement at RHIC. Finally, a summary of results presented is given in chapter 10.

CHAPTER 2

QUARKS, PARTONS AND QCD

Understanding the internal structure of the nucleon is one of the most fundamental problem of strong interaction physics. The meson exchange picture was introduced in 1935 by the Japanese physicist Hideki Yukawa to describe the interaction between protons and neutrons in the atomic nucleus. A large number of mesons and baryons were discovered in the 1950s and 1960s. The mesons and baryons are collectively called "hadrons". The observed spectrum of hadrons and their static properties and studies of hadron properties in high energy collisions involving large momentum transfers indicated that the hadrons are composed of more elementary entities.

Until 1972, there was no real theory of strong interactions; there were several models (e.g. the quark model, the parton model [4, 5]), which were able to describe certain parts of the existing experimental data, but none of the models was able to give a consistent and overall description of the experimental results. The next three sections will review the quark model, the parton model and give an introductory discussion of the theory of the strong interactions known as Quantum Chromodynamics (QCD).

2.1 The Quark Model

In 1963 Gell-Mann and Zewig proposed a model that explained the spectrum of strongly interacting particles in terms of elementary constituents called quarks which were assumed to be spin 1/2 particles. Using the quarks as building blocks, it became possible to organize the existing mesons and baryons into a hadronic spectrum. The quark model treats mesons and baryons as states which transform like states made up of quark-antiquark ($q\bar{q}$) and three quarks (qqq) respectively. Even though the model was successful in predicting new hadronic states and explaining the strengths of electromagnetic and weak interaction transitions among the different hadrons, there was a serious problem with it. First, since the baryons are supposed to be made up of three quarks, each quark should have a fractional charge to explain the charge of the baryons. However, free charges with fractional charge have never been found. Second, the spectrum of the baryons required the assumption that the wave function of the three quarks be totally symmetric under the interchange of the spin and flavour quantum numbers, contradicting the expectation that the quarks, being spin 1/2 particles should obey Fermi-Dirac statistics. The delta isobar($\Delta^{++}(uuu), s = 3/2$), for example, was known to obey Fermi-Dirac statistics and hence needed a completely antisymmetric wave function to describe it. The quark model wave function for the delta isobar was predicted to be totally symmetric. In order to enforce an antisymmetric wave function which is required for a state composed of identical particles with spin 1/2, an additional degree of freedom, namely "color", was given to quarks. According to this picture, each quark exists in three versions or colors. Hadrons then had to be composed of quarks such that they are invariant under color transformations.

It was realized very soon that the quarks cannot be observed directly in experiments, but are confined in mesons and baryons.

2.2 The parton Model

The quark model of hadrons considers the quarks to be at rest and could not explain the so-called hard processes such as electron-positron annihilation into hadrons and deep inelastic electron-nucleon scattering which is characterized by large transfers of energy and momentum. The parton model [6] was developed around the end of the 1960s to describe experimental results obtained from deep inelastic scattering of electrons from protons [7, 8] where the proton is shattered and a system with a large number of hadrons is produced. In this model, a fast moving hadron can be regarded as a collection of many "partons" all of which travel in more or less the same direction as the parent hadron. A basic assumption of this model was that the partons are incapable of exchanging large momenta through the strong interaction and the time scale of the hard scattering process is very short compared to that of inter-parton interactions so that the other partons on the proton can be regarded as spectators in the scattering process. The scattering cross section is expressed in terms of the so-called structure functions which contain information about the dynamics of the strong interaction part of the process.

A very important prediction of the parton model is the scale invariance of the structure functions in the limit of large momentum and energy transfers. This has been confirmed experimentally and was taken as evidence for the existence of point-like constituents in the proton [9, 10]. Experimental results on the charge carried by partons agree with the parton model predictions if one assumes that the partons

have one third integer charges as in the quark model. The assumption that the momentum of the nucleon is divided among the partons implies that a summation over the fractional momentum contributions of the individual partons must give one. Experimental data, however, indicated that the partons carry only half the total momentum of the nucleon suggesting that there are further partons which carry the other half of the total momentum. These other partons must be neutral with respect to weak and electromagnetic interactions but are taken to be responsible for the strong interaction between quarks. The charged partons came to be identified with the valence quarks and a quark-antiquark "sea" [11, 12] and the neutral partons were identified with the gluons [13]

2.3 QCD Overview

Quantum Chromodynamics [14, 15] is a theory of the strong interactions binding quarks into the observed hadrons. It is a non-abelian gauge field theory [16] built on color and invariance under local $SU(3)_3$. Its only free parameters are the strong coupling strength α_s and the masses of the different quark flavors. The QCD Lagrangian is given by

$$
\begin{aligned}
L_{QCD} &= L_0 + L_1 + L_2 && (2.1)\\
L_0 &= -\bar{\psi}(\gamma_\mu \partial_\mu + M)\psi - \frac{1}{4} F^a_{\mu\nu} F^a_{\mu\nu} && (2.2)\\
L_1 &= \frac{i}{2} g \bar{\psi} \gamma_\mu \lambda^a \psi A^a_\mu(x) - \frac{g}{2} f^{abc} F^a_{\mu\nu} A^b_\mu A^c_\nu && (2.3)\\
L_2 &= -\frac{g^2}{4} f^{abc} f^{ade} A^b_\mu A^c_\nu A^d_\mu A^e_\nu && (2.4)
\end{aligned}
$$

where $F^a_{\mu\nu} = \partial_\mu A^a_\nu - \partial_\nu A^a_\mu$. The first term of L_0 gives the kinetic energy of quarks and while the second term gives the kinetic energy of the gluons. The first term in L_1 describes the interaction between a quark and a gluon and the second term represents three gluon self interactions. L_2 corresponds to four gluon self interactions. According to QCD, the potential between two heavy colored quarks is given by

$$V(r) = \frac{\alpha^s}{r} + \sigma r \tag{2.5}$$

where r is the separation between the two quarks. The first term is negligible at large distances. As a result the potential grows linearly with r implying that an infinite amount of energy is required to separate the quarks. This is one of the two remarkable properties of QCD known as confinement. It is an empirical fact that quarks and color are confined to the interior of hadrons. Lattice gauge theory calculations indicate that confinement is a dynamic property of QCD arising from the strong non-linear gluon couplings. The virtual gluon-gluon interactions cause the color field lines to concentrate into flux tubes, or strings as they are usually called, as the separation between the quarks increases. Since the potential energy in the string grows with distance, at a certain separation it becomes energetically possible to form a new quark-antiquark pair. The second property is the so-called asymptotic freedom which is related to the running coupling constant given by

$$\alpha_s = \frac{\alpha^s(\mu^2)}{1 + \frac{33-2f}{12\pi} \;\; \alpha^s(\mu^2) \;\; ln(\frac{Q^2}{\mu^2})} \tag{2.6}$$

where $\alpha^s(\mu^2)$ is the coupling constant at the reference momentum μ, Q is the four momentum transfer, and f is the number of quark flavors. This also arises from the nonlinear gluon couplings which make the renormalized coupling constant gets very small at very large momenta or equivalently at very short distances. At sufficiently

small distances α^s approaches zero faster than r, the force binding the quarks together vanishes and they become asymptotically free. This is what has been seen in deep-inelastic electron-nucleon scattering [10, 17] at SLAC. The effect arises from the anti-shielding of the color charge(as opposed to the shielding one has in QED). When the effective coupling constant is small, one can use perturbation theory [18, 19].

Due to asymptotic freedom, the strong interaction becomes weak for hard (short distance) processes which involve large momentum transfers. As part of the standard model, perturbative QCD provides a successful description of such hard phenomena. However, soft physics phenomena like color de-confinement, chiral symmetry restoration and the structure of the vacuum are not well understood from first principles in QCD. A system in which quarks and gluons exist in a de-confined state, such as a Quark Gluon Plasma (QGP), offers the possibility to study and gain an understanding of processes in the soft non-perturbative sector. Such a de-confined state might be created in the laboratory in heavy ion collisions at the highest possible energies.

At low energies, quarks are confined in groups of two or three making up nucleons and other hadrons. As matter is heated or compressed the quarks would be able to move freely over a volume that is large compared to that of a single hadron at high temperatures or densities. Colliding together beams of massive, highly relativistic nuclei generate matter with high energy and particle densities offering the possibility of observing a phase transition from normal hadronic matter to the quark gluon plasma. The transition between these two forms of matter may be abrupt (1^{st} order with a latent heat or 2^{nd} order without a latent heat) or only a smooth but rapid cross-over.

In the collision of nuclei at extremely high energies, the energy densities are expected to reach critical values forming an extended volume of quarks, antiquarks and gluons. These particles were originally assumed to interact relatively weakly with each other if the matter created in the collision is a QGP [20]. This idea is being revised following the new exciting results from the RHIC experiments [21, 22] which seem to indicate that the matter created is an equlibrated but strongly coupled QGP.

QCD calculations on the lattice predict that the system undergoes a phase transition from nuclear matter to a de-confined system of quarks and gluons at an energy density $\epsilon \approx 1$ GeV/fm^3 corresponding to a temperature of about 170 MeV [23].

CHAPTER 3

SIGNATURES OF A QUARK GLUON PLASMA

The collision between two nuclei may be considered a superposition of nucleon-nucleon (NN) collisions. In addition to the nucleons scattering with each other several times, the partons produced in different NN collisions also re-scatter with each other. The particle production per participating nucleon changes as a result of these scattering. It is ssumed that a state of local equilibrium is achieved through the re-scattering processes by redistributing the energy lost by the beams into statistically most probable configuration. The re-scattering gives rise to a thermodynamic pressure which acts against the outside vacuum leading to collective expansion of the reaction zone. The expansion dilutes the reaction fireball and the quarks and gluons get bound to form hadrons once the energy density falls below the critical value ϵ_c. The hadrons themselves will interact among themselves but their interaction ceases once their average distance exceeds the range of the strong interactions leading to a phenomenon known as freeze-out. The many interactions among the hadrons themselves before the freeze-out washs out much of the information about their original production processes. Thus, extracting information about the hot and dense early collision stage requires to exploit features which are either established early and survive the re-scattering and collective expansion or can be reliably back-extrapolated.

In the following sections, some of the signatures believed to provide information on QGP formation will be briefly discussed.

3.1 J/ψ suppression

In a Quark Gluon Plasma, the color charge of a quark is subject to screening due to the presence of gluons and other quarks and antiquarks. This phenomenon is called Debye screening, in analogy to the familiar Debye screening of an electric charge in QED. In Nucleus-Nucleus collisions, J/ψ particles are produced in the initial stages of the collision process, for example by hard scattering processes. If a QGP is formed in the region of J/ψ production, then the high gluon density and the abundant presence of the light quarks and antiquarks would debye screen the color interaction between c and $\bar{c}$ quarks produced during the initial nuclear impact, thus preventing the charm quarks from binding into J/ψ [24]. As a result, the final yield of J/ψ particles will be suppressed as compared to the case when there is no QGP. Therefore the suppression of J/ψ may be used as signature of QGP. J/ψ suppression was indeed observed at the SPS by the NA38/NA50 collaboration [25]. However, it is also possible that the production of J/ψ is suppressed due to inelastic interactions with dense hadronic matter created in the collision [26]. Normal nuclear effects such as transverse momentum broadening and nuclear shadowing are also predicted to lead to J/ψ suppression at high energies [27]. It is clear that a careful understanding of several effects that could explain the suppression of J/ψ production is necessary in order to use J/ψ suppression as a signature for the formation of a quark-gluon plasma.

3.2 Dileptons and direct photons

A photon produced in a QGP leaves the hot plasma with little interaction in the outer freeze-out region. It would keep memory of the temperature in which it was created and would therefore be a good signature of QGP formation. In order to see whether there are directly produced photons in the QGP we must study inclusive photon production and find out if there are some kinematical differences between the sample of selected inclusive photons and the photons which are known to originate from normal hadronic decays [29, 30]. In spite of the difficulties arising from large backgrounds, experiments at the SPS have searched for directly produced thermal radiation of photons and enhancements over hadronic decay backgrounds were reported. However, no unambiguous connection with thermal radiation has been established, in part because the predicted signal is marginal at the SPS [31, 32], given the accuracy of the experiments. To see the plasma shine, one needs the higher temperatures and longer plasma lifetimes. The suppression of π^0 production at high transverse momentum as measured by the PHENIX experiment [22] at RHIC allows for observation and study of direct photons from a QGP.

3.3 Strangeness enhancement

It has been suggested that one of the possible signatures of the QGP would be an enhancement of the production of strange particles relative to the production observed in nucleon-nucleon collisions [33]. In a QGP gluons are abundantly produced and many quark-antiquark pairs are created via gluon-gluon fusion. In this process, strange quark-antiquark pairs would be produced more frequently than in the nucleon-nucleon collisions because the coupling of gluons to strange quarks and to light quarks

is the same and the higher mass of the strange quarks would not be important due to the high available energy [34]. In a baryon rich environment which also contains high density of u and d quarks and antiquarks, further production of u and d quarks from $\bar{u}$ and $\bar{d}$ pairs should be suppressed by the pauli principle favoring a higher relative abundance of strange quarks.

3.4 Elliptic Flow

Collisions of nuclei with finite impact parameters (non-central collisions) initially produce overlap regions with a spatial anisotropy. The overlap of the two nuclei can lead to observables which are highly sensitive to their emission angle relative to the reaction plane which is defined by the beam direction and the impact parameter direction. One such observable is the so-called "elliptic flow" which is the anisotropic emission of particles "in" or "out" of the reaction plane. The origin of elliptic flow is the initial spatial anisotropy of the overlap region which leads to momentum anisotropy due to particle rescatterings in the evolving system. Being dependent on re-scattering, elliptic flow is sensitive to the degree of thermalization of the system at early times [35, 36]. Details of the elliptic flow dependence on beam energy and centrality are thought to be sensitive to the phase transition between confined and de-confined matter [37, 38, 39, 40]. Results from elliptic flow measurements [21] at RHIC in Au-Au collisions at 200 GeV per nucleon point to strong partonic interactions in an early stage of the collision and early thermalization.

3.5 Jet quenching

Depending on their energy, the quarks and gluons emerging from a collision will materialize into a spray of particles (mostly mesons and baryons). At high momentum, these particles will appear in clusters called "jets," where a jet is defined as a group of particles moving in roughly the same direction, centered about the original parton.

Perturpative QCD calculations predict that high energy partons traversing a nuclear medium lose energy through induced gluon radiation [41]. The magnitude of the energy loss depends on the density of the medium [42] and can be used to probe the properties of the dense matter created in heavy ion collisions. By measuring the attenuation of these partons, a phenomenon called "Jet Quenching", as they propagate through the medium, one would be able to study properties such as the geometry and the gluon density of the medium.

Recent measurements at RHIC in Au-Au collisions have shown a suppression of hadron yields at high transverse momentum relative to peripheral collisions and scaled nucleon-nucleon collisions, consistent with the picture of partonic energy loss in a dense system [22, 43]. The disappearance of the away side jet in a measurement of back to back correlations of jets [21] suggests that the observed high p_t hadrons come from partons produced near the surface of the collision region while the recoil parton is absorbed or rescattered in the medium. Combined together with the elliptic flow results, these observations suggest that a high density and strongly interacting matter has been produced in at RHIC. A detailed study of jet quenching, together with other measurements like electro-magnetic signals and J/Ψ suppression, will thus help to map out detailed properties of matter created in heavy ion collisions.

3.6 HBT Radii

There is a direct connection between the properties of nuclear matter at very high temperatures and densities and the space time evolution of the system created in heavy ion collisions. The important features of this evolution can be accessed using two particle interferometry which gives an estimate of the life-time and final-state size of the reaction zone. If a QGP is formed, it lives only a very short time. However, for a first order phase transition, when the energy density of the QGP is only slightly higher than the threshold value, the system will remain in the mixed phase for a long time during the transition from the plasma phase to the hadronic phase. This arises because for a system not far from the phase transition threshold, the magnitude of its velocity field is small when the system evolves from the plasma phase to the mixed phase at the transition temperature [44]. Furthermore, the pressure of the system in the mixed phase is a constant over the large range of the combined mixed density. Due to the constancy of the pressure in the mixed phase and the small initial velocity field, there is no large scale hydrodynamical motion in the mixed phase. The mixed-phase system will remain in that configuration for a long time, until a phase transition is completed [45, 46, 47, 48] The particles are emitted over a longer period at a smaller rate, hence they have less chance to re-scatter. Resolving the pair momentum along the beam(called the long direction) and transverse to the beam(called the outward direction), the dimension of the source at the moment of last interactions in the outward direction would be larger than the side-ward dimension which is perpendicular to both the long and outward directions.

Recent measurement of charged pion correlations at RHIC [49, 50] did not show the predicted large HBT signal. Attempts to explain this result in a consistant picture

have so far been unsuccessful. A simple thermal-like initial state model coupled to a hadronic rescattering calculation [51] has been found to explain reasonably well the HBT results from RHIC. The calculation suggests a very early hadronization time of about 1 fm/c after the initial collision of the nuclei.

3.7 Chiral Symmetry Restoration

Chiral symmetry is a symmetry of QCD in the limit of vanishing quark masses [52]. It is known that the current-quark masses are finite. But compared with hadronic scales the masses of the two lightest quarks, up and down, are very small, so that chiral symmetry may be considered an approximate symmetry of the strong interactions. The hamiltonian possesses the symmetry but its ground state does not. An important consequence of the spontaneous breakdown of a symmetry is the existence of a massless mode, the so called Goldstone boson. If chiral symmetry was a perfect symmetry of QCD, the pion should be massless. Since chiral symmetry is only approximate, we expect the pion to have a finite but small(compared to all the hadrons) mass which is indeed the case.

At high temperatures and/or densities one expects to restore chiral symmetry. By that one means, that, unlike the ground state, the state of high temperature/density possesses the same symmetry as the hamiltonian (the symmetry of the hamiltonian will not be changed). As a consequence of this so called "'chiral restoration"' it is expected that the absence of any Goldstone modes and thus the pions, if still present, should become as massive as all the other hadrons.

CHAPTER 4

THERMODYNAMICS OF A QUARK GLUON PLASMA

The primary motivation for studying nucleus-nucleus collisions at relativistic energies is to understand the equation of state of nuclear, hadronic and partonic matter at high temperatures and densities. The equation of state describes the dependence of energy density ϵ, pressure P, and entropy S on temperature T and chemical potential μ. One looks for dramatic changes in the effective number of degrees of freedom, as expressed by the ratios e/T^4, p/T^4 or s/T^3 over a small temperature range. These quantities would exhibit a discontinuity if there was a first order phase transition.

4.1 Dynamics of Heavy Ion Collisions

Heavy ion collisions at very high energy proceed through a number of different stages, shown schematically in Figure (4.1). The colliding nuclei are assumed to be moving towards each other along the z-axis and are contracted along their direction of motion due to their relativistic speeds. In the first stage, the two colliding nuclei penetrate each other. The quarks and gluons composing the nuclei collide and transfer a large amount of energy to the vacuum which is later observed as new particles. This stage of the collision is thought to be very short lasting only about 10^{-24} seconds.

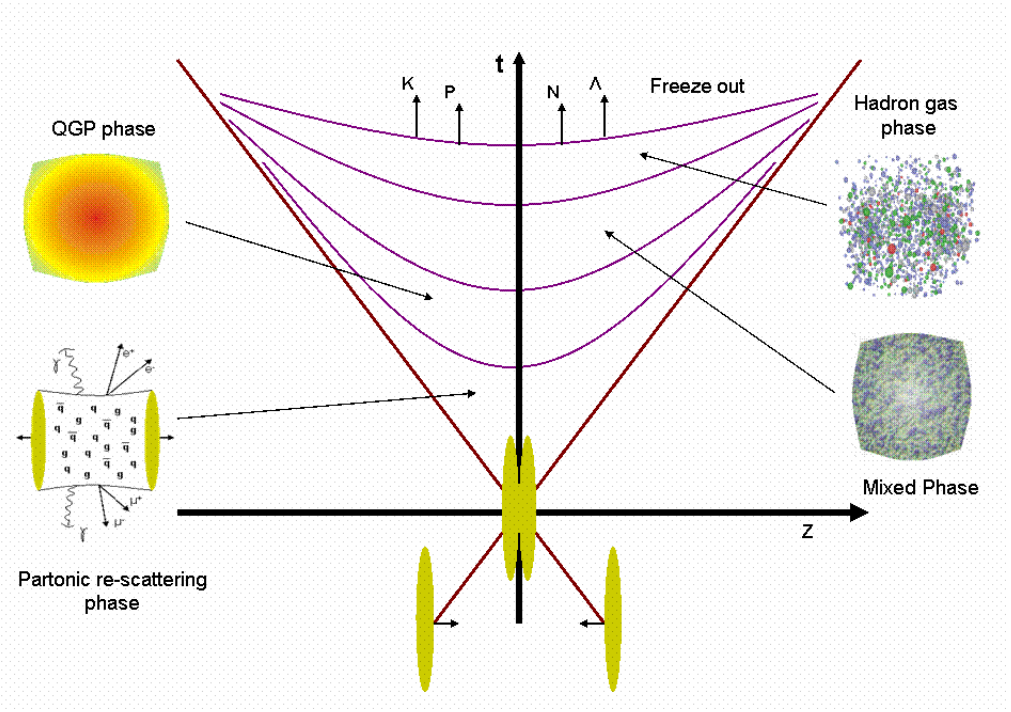

Figure 4.1: Evolution of a heavy ion collision.

The second stage of the collision involves the initial quarks and gluons undergoing "'hard"' collisions among themselves. These collisions produce additional gluons and light and heavy quarks. The quarks and gluons initially present, along with the newly formed quarks and gluons undergo a cascade of further collisions and eventually thermalize sharing their energy equally among themselves. This process should produce a quark-gluon plasma in local thermal equilibrium. The QGP thus produced is expected to live long enough to generate detectable signals. This is then the stage of the collision which experiments will have to sample for evidence of the existence and properties of the QGP.

The third stage is characterized by expansion and cooling of the hot and dense phase, and below the deconfinment temperature and density, the quarks and gluons condense to a gas of hadrons. In this stage of the collision, matter is still highly excited, and the density of the hadrons is large. Scattering between the hadrons maintains the pressure causing further expansion and cooling. The multiple scattering of the particles tend to partition the available energy equally among them and keep the system in equilibrium.

Eventually, in the last stage of the collision, the system is dilute that the hadrons cease colliding and travel outward to the detectors without further interactions.

4.2 Kinematic variables

A useful variable commonly used to describe particle spectra in heavy ion collisions is the so-called rapidity variable. For a particle with energy E and longitudinal momentum P_z, the rapidity is defined as

$$y = \frac{1}{2}\ ln(\frac{E + p_z}{E - p_z}) \tag{4.1}$$

In the non-relativistic limit , the rapidity equals the velocity of the particle in units of the speed of light . The rapidity of a particle in one reference frame boosted in the beam direction is related to its rapidity in another frame only by an additive constant. In terms of the rapidity y, the energy and momentum of the particle are given by

$$E = M_t cosh(y) \tag{4.2}$$

$$P_z = M_t sinh(y) \tag{4.3}$$

where $M_t = \sqrt{P_t^2 + m_0^2}$ is the transverse mass of the particle. To characterize the rapidity of a particle, it is necessary to measure two quantities, the energy and momentum of the particle. In some experiments, however, it is only possible to measure the angle of the detected particle relative to the beam axis. In that case, it is convenient to use this information by using the so-called pseudo-rapidity variable η to characterize the detected particle where

$$\eta = -ln(tan(\frac{\theta}{2})) \tag{4.4}$$

where q is the angle between the particle momentum and the beam axis. In terms of the momentum the pseudo-rapidity variable is written as

$$\eta = 0.5\ ln(\frac{|p| + p_z}{|p| - p_z}) \tag{4.5}$$

If the particles have a distribution $\frac{dN}{dydP_t}$ in terms of the rapidity variable y, then the distribution in the pseudo-rapidity variable η will be

$$\frac{dN}{d\eta dp_t} = \sqrt{1 - \frac{m_0^2}{M_t^2 cosh^2(y)}}\frac{dN}{dydp_t} \tag{4.6}$$

One can see from the last equation that in the region of y much greater than zero, $\frac{dN}{d\eta}$ and $\frac{dN}{dy}$ are approximately the same but in the region of y close to zero, there is a small depression of the $\frac{dN}{d\eta}$ distribution relative to $\frac{dN}{dy}$. Experimentally, the average transverse momentum $< p_t >$, rapidity distribution $\frac{dN}{dy}$ and the transverse energy distribution $\frac{dE_t}{dy}$ are related to the thermodynamic observables temperature T, entropy density s, and energy density ϵ respectively.

When the time scale of the space-time evolution of a given system is relatively slow compared to the microscopic time scale (such as the mean collision time), a lot of different physical configurations appear within a significant global time scale of the

system [53]. Thus, physical properties of the system are basically determined by the statistical average over all the microstates which appear within the macroscopic time-scale. The macroscopic state of the system, which is determined by a small number of parameters, such as temperature, pressure and total energy etc., usually does not specify the microstate α. Microscopically, a lot of interactions among particles will take place within a macroscopic time-lapse τ_h. Almost an infinite set of microstates appear and disappear in this time scale. This (infinite) set of microstates relevant for one macrostate is called ensemble. An ensemble not subject to the constraints of energy and particle number conservation is called the grand canonical ensemble and consideration of such ensembles in statistical equilibrium leads to the partition function

$$Z(V,T,\mu) = exp\{-\sum_i ln[1 \pm e^{-\beta(E_i-\mu)}]\} \tag{4.7}$$

from which one can calculate the relevant thermodynamical quantities. The quark gluon plasma (QGP) in thermodynamic and chemical equilibrium is characterized by temperature T and a baryonic potential μ_B. The densities of light and strange quarks can be determined from the equilibrium Fermi distribution functions which are obtained by taking the appropriate derivatives of lnZ

$$n = -\frac{1}{V}\frac{\partial lnZ}{\partial \beta}\Big|_{\mu\beta} = \frac{g_i}{(2\pi)^3}\int d^3p \frac{1}{e^{(\sqrt{p^2+m_i^2}-\mu_i)/T} \pm 1} \tag{4.8}$$

$$\epsilon = -\frac{1}{V}\frac{\partial\ lnZ}{\partial \mu} = \frac{g_i}{(2\pi)^3}\int d^3p \frac{\sqrt{p^2+m_i^2}}{e^{(\sqrt{p^2+m_i^2}-\mu_i)/T} \pm 1} \tag{4.9}$$

$$\langle P \rangle \;\; = \;\; \pm\frac{1}{\beta V}\ lnZ = \frac{g_i}{(2\pi)^3}\frac{1}{\beta}\ \int d^3p\ ln[1 \pm e^{\sqrt{p^2+m_i^2}-\mu_i}]$$

where the index i runs over $i = u, d, s, g$, and the plus sign is to be used for quarks, the minus sign for gluons. The chemical potentials $\mu_u = \mu_d \equiv \mu_q = \frac{1}{3}\mu_B$. Due to the total

strangeness neutrality of the initial state $\mu_s = 0$ and $\mu_g = 0$. p is the momentum,m_i is the mass,T is the temperature and g_i is the spin-color degeneracy factor.

4.3 QGP at high temperatures and zero baryon density

Consider a quark-gluon system in thermal equilibrium at high temperature T within a volume V. Treating the QGP as a continuum and assuming massless quarks and zero baryon density ($n_q = n_{\bar{q}}$), one calculates from Eq. (4.9) the energy densities of the quarks to be

$$\epsilon_q = \frac{g_q}{2\pi^2}\int_0^\infty \frac{p^3 dp}{1+e^{\frac{p}{T}}}, \qquad \epsilon_{\bar{q}} = \frac{g_{\bar{q}}}{2\pi^2}\int_0^\infty \frac{p^3 dp}{1+e^{\frac{p}{T}}} \tag{4.10}$$

where the degeneracy factors $g_q, g_{\bar{q}}$ depend on the number of flavors under consideration. The quark degeneracy is given by

$$g_q = g_{\bar{q}} = N_c N_s N_f \tag{4.11}$$

where $N_c(=3)$ is the number of colors, $N_s(=2)$ is the number of spins, $N_f(=2\text{or }3)$ is the number of flavors. The contribution to the energy density from the quarks is then

$$\begin{aligned} \epsilon_{q+\bar{q}} &= \epsilon_q + \epsilon_{\bar{q}} = \frac{(g_q + g_{\bar{q}})}{2\pi^2}\int_0^\infty \frac{p^3 dp}{1+e^{\frac{p}{T}}} \\ &= \frac{(g_q + g_{\bar{q}})}{2\pi^2}(\Gamma(4)\ \frac{7}{8}\ \frac{\pi^4}{30}T^4) = \frac{7}{4}\ g_q\ \frac{\pi^2}{30}T^4 \end{aligned} \tag{4.12}$$

The energy density of the gluons is

$$\epsilon_g = \frac{g_g}{2\pi^2}\int_0^\infty \frac{p^3 dp}{e^{\frac{p}{T}}-1} = \frac{(g_g}{2\pi^2}(\Gamma(4)\ \frac{7}{8}\ \frac{\pi^4}{30}T^4) = g_g\ \frac{\pi^2}{30}T^4 \tag{4.13}$$

The pressure of a massless system of particles is related to the energy density by $P = \frac{1}{3}\ \epsilon$ and hence

$$P_{q+\bar{q}} = \frac{1}{3}\ \epsilon_{q+\bar{q}} = \frac{7}{4}\ g_q\ \frac{\pi^2}{90}T^4$$

$$P_g = \frac{1}{3}\,\epsilon_g = \frac{7}{4}\,g_g\,\frac{\pi^2}{90}T^4 \tag{4.14}$$

Since there are eight gluons each with two degrees of polarization, $g_g = 8 \times 2 = 16$. For a system with two flavors only $g_q = 12$. Therefore the total pressure and energy density for a system of qaurks, antiquarks and gluons is

$$P_{QGP} = [\frac{7}{8}((g_q + g_{\bar{q}}) + g_g)]\,\frac{\pi^2}{90}T^4, \qquad \epsilon_{QGP} = [\frac{7}{8}(g_q + g_{\bar{q}}) + g_g)]\,\frac{\pi^2}{30}T^4 \tag{4.15}$$

For a relativistic pion gas in thermal equilibrium, treated approximately as a massless boson gas, the pressure and energy density are given by

$$P_{pion} = \frac{1}{3}\,g_{pion}\,\frac{\pi^2}{30}T^4, \qquad \epsilon_{pion} = g_{pion}\,\frac{\pi^2}{30}T^4 \tag{4.16}$$

The ratio of pressure and energy density in a QGP to the corresponding quantities in a pion gas gives

$$\frac{P_{QGP}}{P_{pion}} = \frac{\epsilon_{QGP}}{\epsilon_{pion}} = \frac{7}{8}\,\frac{(g_q + g_{\bar{q}}) + g_g}{g_{pion}} \tag{4.17}$$

Eq. (4.17) indicates that there would be a large change in the number of degrees of freedom during a phase transition from a QGP to hadronic system.

The above treatment of the thermodynamic variables for the QGP is too simplistic since a QGP which may be produced in the laboratory is a spatially finite system with a boundary, i.e., deconfinment extends only over the region within the boundary of the hot quark matter. As a result the equations for the pressure and energy density have to be modified. A system of quarks and gluons confined within a boundary can be treated as a bag with the particles inside. The MIT bag model, for example, describes hadrons as extended objects of quarks and gluons immersed in a vacuum that exerts an inward pressure.

By introducing a bag pressure B directed inward, the energy density and pressure of the system inside the bag will be given by

$$\epsilon_{QGP,bag} = \left[\frac{7}{8}((g_q + g_{\bar{q}}) + g_g)\right] \frac{\pi^2}{90} T^4 + B$$
$$P_{QGP,bag} = [\frac{7}{8}((g_q + g_{\bar{q}}) + g_g)] \frac{\pi^2}{90} T^4 - B \tag{4.18}$$

A lower limit of stability of the plasma state is obtained by setting $P_{QGP,bag} = 0$ from which one can determine the value of the critical temperature if the bag constant B is known, i.e.,

$$T_c = \left[\frac{90}{\frac{7}{8}((g_q + g_{\bar{q}}) + g_g)\ \pi^2}\right]^{\frac{1}{4}} B^{\frac{1}{4}} \tag{4.19}$$

If the quark matter inside the bag is heated from a temperature well below the critical temperature T_c to a sufficiently high temperature above T_c , the bag will not be able to hold the quark matter, i.e, deconfinment will occur since the pressure inside acting outward will be greater than the bag pressure. Figure (4.2) shows a plot of $\frac{\epsilon}{B}$ and $\frac{P}{B}$ versus $\frac{T^4}{B}$. It can be seen that a phase transition indeed could occur from a hadronic gas to a QGP as the temperature of the system is increased.

4.4 QGP at high baryon density and zero temperature

Another extreme case to the one discussed in the previous section is a system with very high baryon density at zero temperature. Deconfinment of the quarks and gluons is expected in this situation too since the nucleons overlap to such an extent that there is no clear boundary between individual neucleons and the quarks would be moving around over an extended volume. If more and more nucleons are packed inside a bag, the quark density increases and since quarks are fermions, they should populate higher and higher momentum states as a result of the Pauli exclusion principle which prevents quarks with same quantum numbers from occupying the same state.

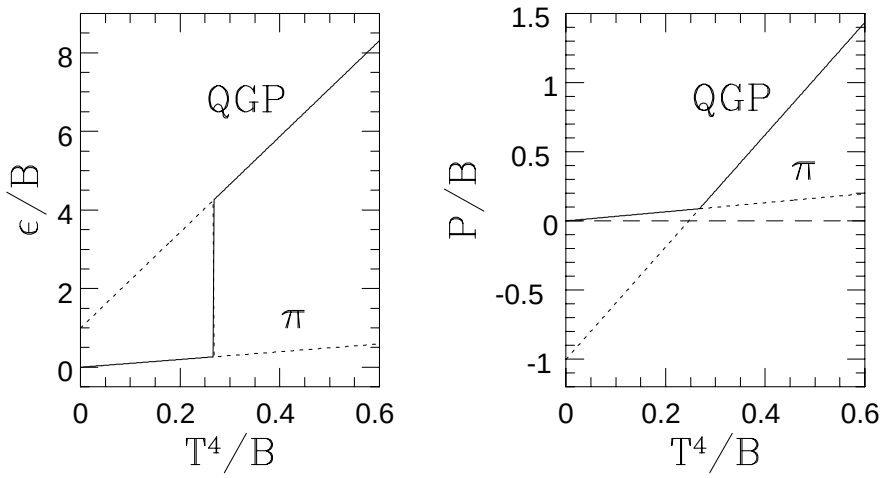

Figure 4.2: Schematic diagram of a phase transition.

The number of states in a bag volume V with momentum p in an interval dp is given by

$$N_q = \frac{V}{(2\pi)^3}\ 4\pi p^2\ dp \tag{4.20}$$

The number density of quarks in the bag is then

$$n_q = \frac{g_q}{(2\pi)^3}\ \int_0^{\mu_q} 4\pi p^2\ dp = \frac{g_q}{6\pi^2}\mu_q^3 \tag{4.21}$$

where μ_q is the chemical potential, i.e, the needed to introduce another quark in the bag volume. The corresponding energy density is

$$\epsilon_q = \frac{g_q}{(2\pi)^3}\ \int_0^{\mu_q} 4\pi p^3\ dp = \frac{g_q}{8\pi^2}\mu_q^4 \tag{4.22}$$

The pressure of the quark gas, using the relation $P = \frac{1}{3}\epsilon$ is

$$P_q = \frac{g_q}{24\pi^2}\mu_q^4 \tag{4.23}$$

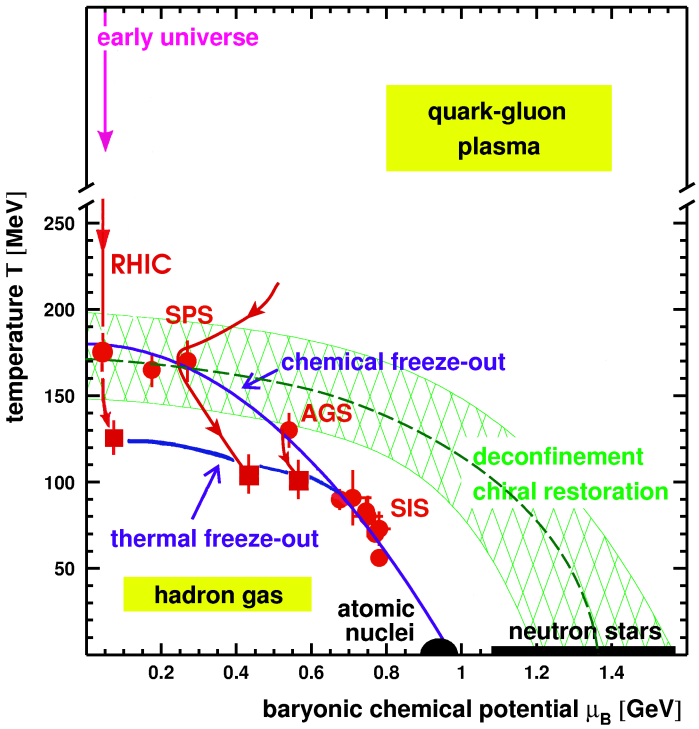

Figure 4.3: The QCD phase diagram.

A change of state of the matter will take place when the bag pressure equals the pressure of the quarks inside the bag which lead to a critical quark number density

$$n_{qc} = 4(\frac{g_q}{24\pi^2})^{\frac{1}{4}} B^{\frac{3}{4}} \tag{4.24}$$

corresponding to a critical baryon number density

$$n_{bc} = \frac{4}{3}(\frac{g_q}{24\pi^2})^{\frac{1}{4}} B^{\frac{3}{4}} \tag{4.25}$$

Eq. (4.24) yields a baryon density of $0.72/\text{fm}^3$ at $T = 0$ with $B = 206$ MeV and $g_q = 12$. This value of the critical baryon density is almost five times the normal nuclear matter density which is about $0.14/\text{fm}^3$. So far only the two extreme cases have been considered. In reality, however, deconfinment of quark matter can also

occur for non-zero temperatures and baryon densities. To get a better understanding of the phase transition, one has to map out a phase diagram in temperature and baryon density showing the transition region together with the results corresponding to the limiting cases discussed in this section. Figure (4.3) shows the $T - \mu_B$ phase diagram where μ_B is the baryon chemical potential [54]. One can see that as the beam energy increases the Baryo chemical potential decreases while the temperature increases. The data points, obtained from an analysis of particle ratios, correspond to the regions probed by different beam energies from SIS to RHIC. The region probed by the highest energies at RHIC is the one where μ_B is close to zero which is also the region in which the early universe is believed to have existed.

Even though the bag model has its own limitations, it is clear that it can account for the possible occurrence of deconfinment from hadronic matter to a QGP. For example, there have been many predictions of exotic states, multiquark and multi-gluon color singlet states which do not occur in the simplest quark models. Experimental observation of such exotic system has proved to be rather elusive. Another frame work that offers a better understanding of a phase transition to quark-gluon matter is the so called Lattice Guage Theory [55] which is the topic of the next section.

4.5 Results from Lattice QCD

The action based on the QCD lagrangian of quarks and gluons gives rise to very complicated physics because the fields in the lagrangian do not correspond to observable particles but are permanently confined to form hadrons. Thus it is possible to use perturbation theory only for deep inelastic (very high energy) phenomena where

asymptotic freedom is at work. The only formulation which is able to give quantitative predictions for hadron physics at low energy (masses, widths, decay amplitudes etc.) is Lattice QCD.

In the framework of lattice QCD a study of the equilibrium thermodynamics of QGP starts with the Euclidean path integral formulation of the partition function [23]. This is given as an integral over the fundamental quark $(\bar{\psi}, \psi)$ and gluon (A_ν) fields. In addition to its dependence on the bare couplings of QCD, i.e, the guage coupling g^2 and the quark masses m_f for $f = 1, 2, ..., n_f$ different quark flavours, the partition function also depends explicitly on the thermodynamic parameters, volume(V) and temperature (T)

$$Z(V,T) = \int DA_\nu D\bar{\psi} D\psi e^{-S_E(v,T)} \tag{4.26}$$

In Eq. (4.25), A_ν and $\bar{\psi}, \psi$ obey periodic and anti-periodic boundary conditions in Euclidean time, respectively. The Euclidean action $S_E = S_G + S_F$ contains a purely gluonic contribution S_G expressed in terms of the field strength tensor $F_{\mu\nu} = \partial_\mu A_\nu - \partial_\nu A_\mu - ig[A_\mu, A_\nu]$ and a fermionic part S_F which couples the guage and fermion fields

$$S_G(V,T) = \int_0^{1/T} dx_4 \int_V d^3x \frac{1}{2} F_{\mu\nu} F_{\mu\nu} \tag{4.27}$$

$$S_F(V,T) = \int_0^{1/T} dx_4 \int_V d^3x \sum_{f=1}^{n_f} \bar{\psi}(\gamma_\mu[\partial_\mu - igA_\mu] + m_f)\psi_f \tag{4.28}$$

The path integrals appearing in Eqs. (4.26) and (4.27) are regularized by introducing a four dimensional space-time lattice of size $N_\sigma^3 \times N_\tau$ with a lattice spacing a. Volume and temperature are then related to the number of points in space and time directions, respectively,

$$V = (N_\sigma a)^3, \quad \frac{1}{T} = N_\tau a \tag{4.29}$$

In the pure gluon sector, a guage invariant, descritized version of the field strength tensor is described in terms of what are known as link variables $U_{x,\mu}$. The link variables $U_{x,\mu}$ are associated with the link between neighboring sites of the lattice and describe the parallel transport of the field A_μ from site x to $x + \hat{\mu}a$

$$U_{x,\mu} = P\ exp(ig \int_x^{x+\hat{\mu}a} dx^\mu A_\mu(x)) \tag{4.30}$$

where $\hat{\mu}$ is a unit vector in the direction of μ-direction of the 4-dimensional lattice and P denotes the path ordering. A product of link variables around an elementary plaquette (Wilson loop of length 4) may be used to define an approximation to the continuum guage action .

The lattice action should have local guage invariance and be able to restore the symmetry properties of the original theory in the continuum limit $a \to 0$. The only parameters that enter in the action are the coupling constant g and the lattice spacing a. All masses and lengths may be expressed in terms of these parameters. In the limit in which the lattice spacing becomes smaller and smaller we expect that it is possible to vary g and a in such a way that the physical properties of the system are unaltered. In the continuum limit different lattice action should produce the same continuum physics (Universality principle). This means that the ratio of masses must be independent of the action used. Different forms of lattice actions which have different scale parameters should correspond to the same physical quantities.

A special problem, called species doubling [56, 57], arises when one tries to write on the lattice the fermionic part of the action. A simple translation of the continuum Dirac action is found to lead to a lattice action which actually describes $2^d (= 16)$ species of fermions in the continuum limit instead of the intended one species of the original continuum action. Different approaches have been used in an attempt to

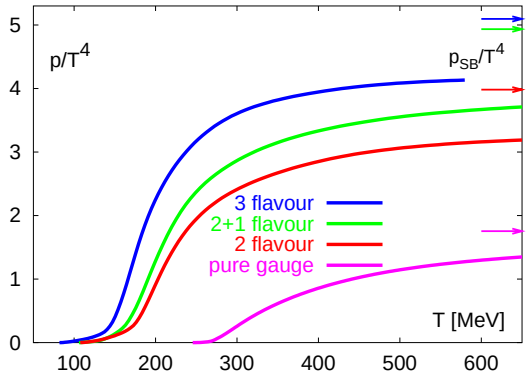

Figure 4.4: Pressure versus temperature from Lattice QCD calculations.

solve the species doubling problem. The two popular choices are the so-called Wilson fermions [55, 56] and staggered fermions [56, 58]. The approach with Wilson fermions involves the addition of a second derivative term, or momentum dependent mass term to the action which lifts the mass of the unwanted doublers in the continuum limit but at the price of explicitly breaking chiral symmetry at any non-zero value of the lattice spacing. The staggered fermions formulation distributes the fermionic degrees of freedom over the original lattice in such a way that the effective lattice spacing is twice the fundamental lattice spacing. While the species doubling problem is not completely solved, the number of flavors is reduced with respect to the naive formulation. The advantage of the staggered fermion action is that it preserves a part of chiral symmetry.

Due to asymptotic freedom, the QCD pressure is expected to approach the ideal gas value at infinite temperature. In this limit the number of degrees of freedom (quarks + gluons) is much larger than the three light pions which dominate the thermodynamics at low temperature. The pressure in QCD with different number of

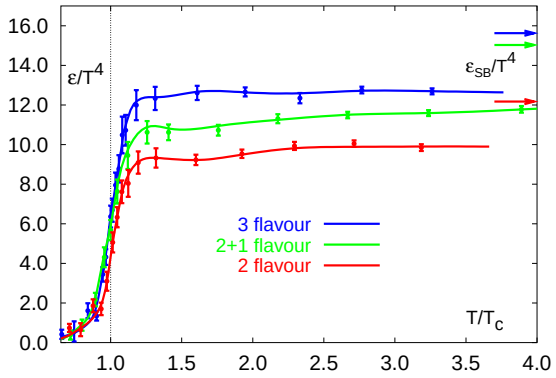

Figure 4.5: Energy versus temperature from Lattice QCD calculations.

degrees of freedom as a function of temperature is shown in Figure (4.4) [57]. The arrows indicate the expected Stephan-Boltzmann ideal gas limit. It can be seen that the pressure strongly reacts to changes in the number of degrees of freedom but varies smoothly with temperature.

The curve labeled (2+1)-flavor corresponds to a calculation with two light and a four times heavier strange quark mass. One thing to note is that the transition region shifts to smaller temperatures as the number of degrees of freedom is increased. At high temperatures, the magnitude of p/T^4 reflects the change in the number of light degrees of freedom present in the ideal gas limit. Rescaling the pressure by the corresponding ideal gas values, the overall pattern of the temperature dependence of p/T^4 becomes quite similar in all cases. The behavior of the energy density as a function of temperature is shown in Figure (4.5) [57] obtained with improved staggered fermions [59]. One can see the abrupt change of the energy density over a very small temperature interval but still the ideal gas limit is not reached.

CHAPTER 5

IDENTICAL PARTICLE INTERFEROMETRY

If a QGP was formed in heavy ion collisions, it would undergo a transition back to a hadronic phase due to subsequent expansion and cooling. One effect of the expected phase transition is delayed expansion of the reaction zone. Delayed expansion causes the system to live longer and as a result, one expects the size in the direction of the pair's momentum to be larger than that in the direction normal to both the pairs' momentum and the beam axis. Intensity interferometry can be used to obtain information on the space time structure of the particle emitting source. The technique of intensity interferometry was initially developed by Hanbury-Brown and Twiss [60] in the 1950s as a means of determining the dimension of distant astronomical objects. The method is now commonly referred to as the Hanbury-Brown-Twiss (HBT) interferometry.

5.1 General Considerations

In conventional amplitude interferometry, particles produce interference patterns which depend on the relative phases of the particles amplitudes as measured. Figure (5.1) shows a schematic diagram of a source of particles and detectors. One of the limitations to stellar diameter measurements using this method is the phase shift induced

in the incident waves amplitudes near the detection points due to atmospheric effects. The further apart the detectors are, the greater the potential for phase changes and hence the poorer the resolution of the amplitude interferometer. Intensity interferometry was developed to reduce the importance of these phase changes.

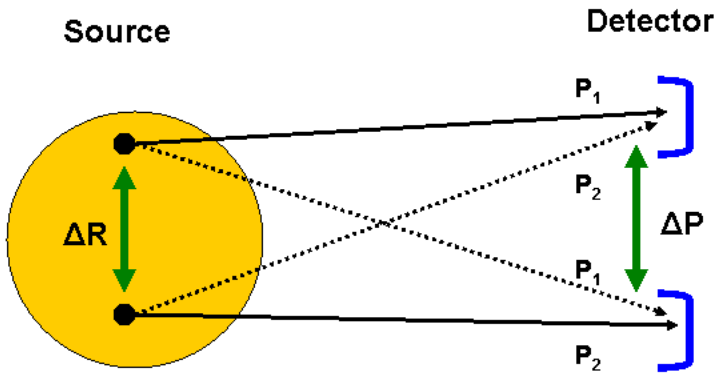

Figure 5.1: Schematic diagram of particle source and detector in HBT interferometry.

In astrophysics applications of the HBT effect, the spatial characteristics of the particle emitting source are assumed to have no strong time dependence over the time scale of the measurements. The situation is very different in applications of the HBT effect to reactions of subatomic particles. Here the system is evolving with time and the system is used to investigate the systems spatial and temporal characteristics.

The first investigation of Bose-Einstein symmetrization effects in subatomic reactions came from a study of pion emission in proton-antiproton annihilation [61]. What was observed was an enhancement of pion pairs, known as the GGLP effect, at small relative momenta in their angular distribution. The effect was explained in

terms of the finite spatial extension of the decaying pion system and the finite quantum mechanical localization of the decay pions. The connection of the GGLP effect with HBT was later made by Kopylov *et al.* [62].

5.2 Correlation Functions

Because of the symmetrization (or antisymmetrization) of their wave function, identical particles can have a nonzero correlation function even if the particles are otherwise noninteracting. There exist different approachs to derive correlation functions for a given system of particles. For identical bosons, a simplified approach to construct a correlation function starts with a symmetrized plane wave [63]

$$\begin{aligned}\Psi_{12} &= \frac{1}{\sqrt{2}}\Big[A(x_1,p_1)e^{i(r_1-x_1)\cdot p_1}A(x_2,p_2)e^{i(r_2-x_2)\cdot p_2} \\ &\qquad + A(x_2,p_1)e^{i(r_1-x_2)\cdot p_1}A(x_1,p_2)e^{i(r_2-x_1)\cdot p_2}\Big] \qquad (5.1)\end{aligned}$$

Where $A(x,p)$ is the production amplitude for the production of a particle with momentum p at x. The two particle momentum distribution is given by

$$\begin{aligned}P(p_1,p_2) &= \int d^4x_1 d^4x_2 \rho(x_1)\rho(x_2)|\Psi_{12}^*\Psi_{12}|^2 \\ &= \int d^4x_1 \rho(x_1)A^2(x_1,p_1)\int d^4x_2\rho(x_2)A^2(x_2,p_2) \\ &\qquad + \left|\int d^4x_1\rho(x)A^2(x,p_1)A^2(x,p_2)e^{i(p_2-p_1)\cdot x}\right|^2 \\ &= P(p_1)P(p_2) + \left|\int d^4x_1\rho(x)A^2(x,p_1)A^2(x,p_2)e^{i(p_2-p_1)\cdot x}\right|^2 \qquad (5.2)\end{aligned}$$

where $P(p) = \int d^4x\rho(x)A^2(x,p)$ is the single particle momentum distribution and $\rho(x)$ is the spatial distribution of emission points in the source. The two particle correlation function is defined as the ratio of the probability $P(p_1,p_2)$ of finding two particles with momenta p_1 and p_2 to the product of the individual probabilities $P(p)$

$$
\begin{aligned}
C_2(p_1,p_2) &= \frac{P(p_1,p_2)}{P(p_1)P(p_2)} \\
&= 1+\frac{\left|\int d^4x_1\rho(x)A^2(x,p_1)A^2(x,p_2)e^{i(p_2-p_1)\cdot x}\right|^2}{\int d^4x_1\rho(x_1)A^2(x_1,p_1)\int d^4x_2\rho(x_2)A^2(x_2,p_2)}
\end{aligned}
\tag{5.3}
$$

The correlation function is expressed in terms of the Fourier transform of the effective source distribution $\tilde{\rho}_{eff}(x,p_1,p_2)=\frac{\rho(x)A(x,p_1)A(x,p_2)}{\rho(x_1)A^2(x_1,p_1)\int d^4x_2\rho(x_2)A^2(x_2,p_2)}$

$$
C(q)=1+\left|\tilde{\rho}_{eff}(p_1,p_2)\right|^2 \tag{5.4}
$$

Another formalism is the so-called classical current parameterization [64, 65]. Particle production in a nuclear collision is assumed to be described by the field equations for the particle field $\Phi(x)$

$$
(\partial_\mu\partial^\mu+m^2)\Phi(x)=\hat{J}(x) \tag{5.5}
$$

The classical current parameterization approximates the nuclear current $\hat{J}(x)$ by a classical commuting space time function $J(x)$. The underlying picture is that at freeze-out, when the particles stop interacting, the emitting source is assumed not to be affected by the emission of a single particle. The final particle state is then a coherent state $|J\rangle$ which is an eigenstate of the annihilation operator

$$
\hat{a_p}\,|J\rangle = i\tilde{J}(p)\,|J\rangle \tag{5.6}
$$

The Fourier transformed classical currents $\tilde{J}$ are on-shell. Usually the classical current is taken to be a superposition of independent elementary source functions J_0:

$$
\tilde{J}(p)=\sum_{j=1}^{N} e^{i\phi_j}e^{ip\cdot x_j}\tilde{J}_0(p-p_j) \tag{5.7}
$$

If the phases ϕ_i are random, then this ansatz characterizes uncorrelated "'chaotic"' particle emission, i.e, a superposition of elementary sources J_0 centered around phase-space points x_i, p_i with random phases ϕ_i describes chaotic sources. The particle spectra is specified by taking the ensemble average

$$\left\langle \hat{a}_p^+ \hat{a}_p \right\rangle = \sum_{N=0}^{\infty} P_N \prod_{i=1}^{N} d^4x_i d^4p_i \rho(x_i, p_i) \int_0^{2\pi} \frac{d\phi_i}{2\pi} \left\langle J | \hat{a}_p^+ \hat{a}_p | J \right\rangle \tag{5.8}$$

where P_N is the probability distribution for the number N of sources, $\sum_{N=0}^{\infty} P_N = 1$ and $\rho(x_i, p_i)$ is the normalized phase-space distribution of elementary sources. The two particle distribution is given by

$$P(p_1, p_2) = \frac{\langle N(N-1) \rangle_P}{\langle N \rangle_P^2} (P_1(p_1) P_2(p_2) + |\bar{S}_J(p_1, p_2)|^2) \tag{5.9}$$

where $\bar{S}_J(p_1, p_2) = \sqrt{E_1 E_2} \left\langle \hat{a}_p^+ \hat{a}_p \right\rangle$ and the integer N denotes the number of sources and $\langle N(N-1) \rangle_P = \sum_{N=0}^{\infty} P_N N(N-1), \langle N \rangle_P = \sum_{N=0}^{\infty} P_N N$. The Fourier transform of $\bar{S}_J(p_1, p_2)$ gives the emission function $S(x, K)$ which is an effective single particle Wigner phase space density of the particles in the source. Here $2K = p_1 + p_2$ is the total four momentum of the pair . The two particle correlator is written as

$$C(q, K) = 1 + \frac{|\int d^4x S(x, K) e^{iq \cdot x}|^2}{\int d^4x S(x, K - \frac{1}{2}q) \int d^4y S(y, K + \frac{1}{2}q)} \tag{5.10}$$

where $q = p_1 - p_2$ is the relative momentum. Using the so-called smoothness approximation $K - \frac{q}{2} \approx K$ [66], the two particle correlation function is expressed as

$$C(q, K) = 1 + \frac{|\int d^4x S(x, K) e^{iq \cdot x}|^2}{|\int d^4x S(x, K)|^2} \tag{5.11}$$

where $\vec{q} = \vec{p_1} - \vec{p_2}, q_0 = E_1 - E_2, \vec{K} = \frac{1}{2}(\vec{p_1} + \vec{p_2})$, and $K_0 = \sqrt{m^2 + |\vec{K}|^2}$. The function $S(x, K)$ describes the phase space density of the particle emitting source.

For identical particles, since the four momenta of the two measured particles are on shell, the four momenta q and K satisfy the orthogonality relation

$$\begin{aligned} q_\mu K^\mu &= \frac{1}{2}(p_{1\mu}p_1^\mu - p_{2\mu}p_2^\mu) \\ &= m^2 - m^2 = 0 \end{aligned} \tag{5.12}$$

Eventhough $p_i^0 = E_i = \sqrt{m^2 + p_i^2}$, the four vectors q and K are off-shell. For a system with a Gaussian distribution of source points, the correlation function is parameterized by a Gaussian function in relative momentum space as

$$C(q,K) = 1 + e^{-q_\mu q_\nu \langle \bar{x}^\mu \bar{x}^\nu \rangle} \tag{5.13}$$

Eq. (5.12) expresses the width of the correlation function in terms of the rms widths of the single-particle wigner density $S(x,K)$. The orthogonality constraint implies that not all components of q are independent. One can eliminate the time component through the relation $q^0 = q \cdot \frac{|\vec{K}|}{K^0}$. For a Cartesian parameterization [67], one introduces a coordinate system such that the z-axis is along the beam direction, see Figure (5.2). Then, the component of the vector $\vec{K}$ along the beam direction is labeled K_l (for longitudinal), the component transverse to the beam direction is denoted K_o (for outward) and the component perpendicular to both the outward and longitudinal directions is denoted by K_s (for sideward). For azimuthally symmetric systems, it is convenient to orient the x axis along the transverse component of the pair momentum such that $K = (K_o, 0, K_l)$, i.e, the pair momentum $\vec{K}$ lies in the $x - z$ plane. Using the mass-shell constraint to eliminate q^0, one obtains for the correlation function the parameterization,

$$C(q,K) = 1 + \lambda(K)\ exp[- \sum_{i,j=o,s,l} R_{ij}^2(K) q_i q_j] \tag{5.14}$$

where the HBT radius parameters R_{ij} are defined in terms of the variances of the source function

$$R_{ij}^2 = \left\langle (\tilde{x}_i - \beta_i \tilde{t})(\tilde{x}_i - \beta_i \tilde{t}) \right\rangle, i, j = o, s, l \tag{5.15}$$

The parameter $\lambda(K)$ equals unity for a fully chaotic particle source.

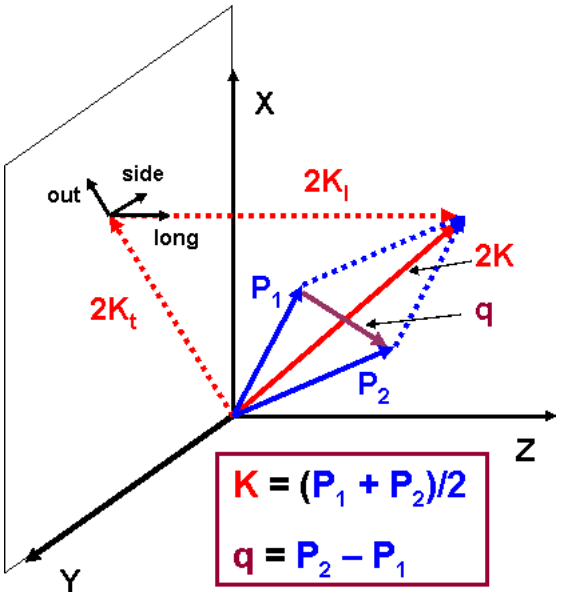

Figure 5.2: Coordinate system for the Cartesian parameterization showing the out, side and long directions in which the 4-momentum of the pair is decomposed.

Azimuthal symmetry implies that $C(q, K)$ is symmetric with respect to $q_s \to -q_s$. It follows then that $R_{ij}^2 = R_{ij}^2 = 0$ and the correlation function becomes

$$C(q, K) = 1 + \lambda(K)\ exp[-R_o^2(K)q_o^2 - R_s^2(K)q_s^2 - R_l^2(K)q_l^2 - 2R_{ol}^2(K)q_o q_l] \tag{5.16}$$

Following Eq. (5.14), the non vanishing HBT radius parameters are given by the following expressions

$$R_s^2(K) \;=\; \left\langle \tilde{y}^2 \right\rangle \tag{5.17}$$

$$R_o^2(K) = \left\langle (\tilde{x} - \beta_o \tilde{t})^2 \right\rangle \tag{5.18}$$

$$R_l^2(K) = \left\langle (\tilde{z} - \beta_l \tilde{t})^2 \right\rangle \tag{5.19}$$

$$R_{ol}^2(K) = \left\langle (\tilde{x} - \beta_o \tilde{t})(\tilde{z} - \beta_l \tilde{t}) \right\rangle \tag{5.20}$$

Due to the on-shell constraint, spatial and temporal source sizes are mixed in all observable radius parameters except for R_s^2. This makes the interpretation of a measurement rather involved since the spatial and temporal contributions cannot be resolved in a model independent manner. The situation is simplified for the longitudinal radius R_l^2 if the frame in which the analysis is performed is boosted to the so-called Longitudinally Co Moving System (LCMS) where $K_l = \beta_l = 0$. Then, $R_{ol}^2(K) = \left\langle (\tilde{x} - \beta_o \tilde{t})(\tilde{z}) \right\rangle$. So, the longitudinal dimension is measured directly in the rest frame of the pion pair. Access to the life time is provided by the difference

$$\begin{aligned} R_{diff}^2 &= R_o^2 - R_s^2 \\ &= \beta_t^2 \left\langle \tilde{y}^2 \right\rangle - 2\beta_t \left\langle \tilde{x}\tilde{t} \right\rangle + \left\langle \tilde{x}^2 - \tilde{y}^2 \right\rangle \end{aligned}$$

Experimental correlation functions are usually fit with a Gaussian in terms of four components of the four momentum difference. The parameters of such a fit are then compared to some analytic model in order to to get an idea of what is being measured. The radius parameters in general depend on the 4-momentum K. As a result, what is measured in HBT is the so-called "homogeneity length" [68] which is simply the size of the region within the source from which particles with similar momenta are emitted. The K dependence of the HBT radii (that size of the source as seen by pairs of momentum K) could arise due to collective expansion of the source, temperature gradients along the freeze-out surface and the decay of unstable resonances all which may produce space-momentum correlations.

If one eliminates q_o and q_s in terms of $q_t = \sqrt{q_o^2 + q_s^2}, q^0$, and q_l one arrives at the so called Yanoo_Koonin Parameterization (YKP) [69] which gives the correlation function as

$$\begin{aligned} C(q,K) &= 1 + \lambda\, exp\{-R^2_{YKP,t}(K)q^2t - R^2_{YKP,l}(K)(q^2l - (q^0)^2) \\ &\quad -[R^2_{YKP,o}(K) + R^2_{YKP,l}(K)](q_\mu U^\mu(K))\} \end{aligned} \tag{5.21}$$

where $U(K) = \gamma(K)[1,0,0,v(K)]$ and $\gamma(K) = \frac{1}{\sqrt{1-v^2(K)}}$. The YKP parameters $R^2_{YKP,o}(K), R^2_{YKP,s}(K)$ and $R^2_{YKP,l}(K)$ extracted from such a fit do not depend on the longitudinal velocity of the observer system in which the correlation is measured. They can again be expressed in terms of the space time variances $\langle \tilde{x}_\mu \tilde{x}_\nu \rangle$ and take their simplest form in the Yano-Koonin frame in which $v(K)$ vanishes.

$$\begin{aligned} R^2_{YKP,t}(K) &= R^2_s(K) = \left\langle \tilde{x}_s^2 \right\rangle \\ R^2_{YKP,l}(K) &= \left\langle (\tilde{x}_l - \frac{\beta_l}{\beta_t}\, \tilde{x}_o)^2 \right\rangle - (\frac{\beta_l}{\beta_t})^2 \left\langle \tilde{x}_s^2 \right\rangle \approx \left\langle \tilde{x}_l^2 \right\rangle \\ R^2_{YKP,o}(K) &= \left\langle (\tilde{t} - \frac{1}{\beta_t}\, \tilde{x}_o)^2 \right\rangle - \frac{1}{\beta_t^2}) \approx \left\langle \tilde{t}^2 \right\rangle \end{aligned} \tag{5.22}$$

The YKP radii are most easily interpreted in terms of coordinates measured in this frame. For sources with strong longitudinal expansion, the YKP velocity $v(K)$ accurately reflects the longitudinal velocity at the center $\bar{x}(K)$ of the homogeneity region of particles of momentum K. The YK frame can thus be interpreted as the rest frame of the effective source of particles with momentum K, and the YKP radii measure the transverse, longitudinal and temporal size of this effective source in its own frame.

5.3 Resonance decay contributions

Because of their smaller mass, pions are the most abundant particles produced in heavy ion collisions. A significant fraction of them, however, come from the decay of

unstable resonances after freezout. Resonances affect the source such that it seems to have a larger life time or larger outward source size [70]. Long lived resonances can escape to quite some distance from the freezeout region before decaying leading to HBT radius parameters which are larger than the width of the particle production region. Due to the resonance decay phase-space, secondary pions populate mainly the low momentum region and can thus introduce an additional pair momentum dependence of the two-particle correlator.

Wiedemann and Heinz [71] studied the contribution of resonance decays in detail. They considered the emission function to be the sum of a direct term and another term for each resonance decay channel

$$S(x,p) = S^{dir}(x,p) + \sum_{r \neq \pi} S_{r \to \pi}(x,p) \tag{5.23}$$

where the sum is over the decay channel. Their findings indicate that long lived resonances with width < 1 MeV cannot be resolved in correlation measurements but they reduce the correlation strength without influencing the shape of the correlation function in the region where it can be measured. On the other hand, short-lived resonances with width > 30 MeV decay close to their production point and thus do not change the spatial width of the emission function. Those resonances with widths such that they are not sufficiently long-lived to escape detection and not sufficiently short-lived to not change the spatial width of the emission function lead to non-Gaussian distortions in the correlator.

Kaon HBT on the other hand suffers less from resonance contributions and could provide a cleaner signal for correlation studies than pions. In particlular, neutral kaon correlations have an advantage over their charged counterparts due to the absence of final state Coulomb interactions.

CHAPTER 6

NEUTRAL KAON CORRELATIONS

According to their behavior under the operation of charge conjugation, neutral particles fall into two classes: (a) particles like the photon and the π^0 that transform into themselves and are thus their own antiparticles and (b) particles like the neutron that behave like charged ones in that they have antiparticles distinct from themselves For the second of class of particles, there exist conservation laws that prohibits virtual transitions between particle and antiparticle states. An example of this class of particles is the neutron which can be distinguished from the anti-neutron by the sign of its magnetic moment. The law that forbids the virtual processes $N \rightleftharpoons \bar{N}$ is the law of conservation of baryon number which states that the number of baryons minus the number of antibaryons must remain unchanged. Another example is the neutral kaon system, K^0 $(d\bar{s})$ and $\bar{K^0}$ $(\bar{d}s)$, whose production is attributed to the strong interaction which conserves the strangeness quantum number. Gell-Mann and Pais [72] noted that the process $K^0 \rightleftharpoons \bar{K^0}$ proceeds through a second order weak interaction. As a result the particles that we normally observe through weak decay channels in the laboratory are not K^0 and $\bar{K^0}$ but rather some linear combination of the two, i.e, particles with mixed strangeness.

In a representation with $|K^0\rangle = \begin{pmatrix} 0 \\ 1 \end{pmatrix}$ and $\left|\bar{K^0}\right\rangle = \begin{pmatrix} 1 \\ 0 \end{pmatrix}$ as basis vectors with definite strangeness, one may express a general neutral kaon wave function by

$$|\Psi_k\rangle = c_1 \left|K^0\right\rangle + c_2 \left|\bar{K^0}\right\rangle \tag{6.1}$$

The $K_s^0 K_s^0$ system is a linear combination of K^0K^0, $\bar{K^0}\ \bar{K^0}$ and $K^0\bar{K^0}$. If a $K_s^0 K_s^0$ pair comes from K^0K^0 ($\bar{K^0}\ \bar{K^0}$), it is subject to BE enhancement as it originates from an identical boson pair. On the other hand, a $K^0\bar{K^0}(\bar{K^0}K^0)$ system gives a $K_s^0 K_s^0$ pair which is not necessarly subject to BE symmetrization. In general, the wave function of the $|K^0\bar{K^0}>$ state is made up of $C = +1$ and $C = -1$ eigenstates of the charge conjugation operator [73]:

$$\left|K^0\bar{K^0}\right\rangle_{C=\pm 1} = \frac{1}{\sqrt{2}}(\left|K^0(p)\bar{K^0}(-p)\right\rangle \pm \left|\bar{K^0}(p)K^0(-p)\right\rangle) \tag{6.2}$$

where p is the three momentum vector of one of the pairs in their center of mass frame. One can see that, the probability amplitude for the $C = -1$ state disappears in the limit of vanishing momentum while it goes to unity for the $C = +1$ state. A measurement of only $K_s^0 K_s^0$ thus leads to a BE like enhancement in the low Q region.

In order to study the correlation of neutral kaons, one has to work with the particles that are actually measured in experiments. As the STAR experiment measures neutral kaons through their weak decay topology, it is convenient to work with the short lived K_s^0 and the long lived K_l^0. Allowing for CP violation one writes,

$$\left|K^0\right\rangle = \frac{\sqrt{1+|\delta|^2}}{2}\left(\left|K_s^0\right\rangle + \left|\overline{K_l^0}\right\rangle\right), \quad \left|\bar{K^0}\right\rangle = \frac{\sqrt{1+|\delta|^2}}{2\delta}\left(\left|K_s^0\right\rangle - \left|\overline{K_l^0}\right\rangle\right) \tag{6.3}$$

If CP is conserved, then $\delta = 1$. Neglecting CP violation, the time dependence of neutral kaon in terms of arbitrary mixture of CP eigenstates becomes

$$|\Psi_k\rangle \ = \ \frac{1}{\sqrt{2}}\left(a_1(0)e^{-i(E_1 t - i\frac{t}{2\tau_1})}\,|K_s\rangle + a_2(0)e^{-i(E_2 t - i\frac{t}{2\tau_2})}\,|K_l\rangle\right) \tag{6.4}$$

where $a_1(0)$, $a_2(0)$ are the amplitudes at $t = 0$, E_1 and E_2 are the energies of the CP eigenstates, τ_1 and τ_2 are their mean lifetimes. The propagation of a neutral kaon from the source at $\vec{x}_1$ to the detector $\vec{x}_A$ via momentum eigenstate $\vec{k}_A$ is

$$|\Psi_{k_A,t}\rangle = \frac{1}{\sqrt{2}}\Big((a_s(0)e^{-i(E_s t - i\frac{t}{2\tau_s})}\,|K_s\rangle + a_l(0)e^{-i(E_l t - i\frac{t}{2\tau_l})}\,|K_l\rangle\Big)e^{i\vec{k}_A\cdot(\vec{x}_A-\vec{x}_1)}e^{i\phi} \quad (6.5)$$

where ϕ is a random production phase at the source. Two neutral kaons propagating from source to detector are indistinguishable, hence the two-kaon amplitude for propagation from source coordinates x_1^μ,x_2^μ to detection at x_A^μ ,x_B^μ

$$\begin{aligned} |\Psi_{12}\rangle &= \frac{1}{\sqrt{2}}\Big(\left|\Psi^{(1)}_{k_A}(x_1^\mu, x_A^\mu)\right\rangle\left|\Psi^{(2)}_{k_B}(x_2^\mu, x_B^\mu)\right\rangle \\ &\quad + \left|\Psi^{(2)}_{k_A}(x_2^\mu, x_A^\mu)\right\rangle\left|\Psi^{(1)}_{k_B}(x_1^\mu, x_B^\mu\right\rangle\Big) \end{aligned} \quad (6.6)$$

This includes any, arbitrary two-neutral-kaon initial state and all four possible final states $K_{s_A}K_{s_B}, K_{l_A}K_{l_B}, K_{s_A}K_{l_B}, K_{l_A}K_{s_B}$. Projecting the one particle state for K_s , with $k_{A\mu} = (\vec{k}_A, k^0)$ where $k^0 = E_s$, $x_A^\mu = (\vec{x}_A, t_A)$, $x_1^\mu = (\vec{x}_1, 0)$, we get

$$\langle K_s|\Psi(k_A, t_A)\rangle = \frac{1}{\sqrt{2}}\; a_s(0)e^{i\phi_1}\; e^{\frac{t_A}{2\tau_s^A}}e^{ik_{A\mu}\cdot(x_A^\mu - x_1^\mu)} \quad (6.7)$$

The $t = 0$ amplitude , $a_s(0)$ will be generalized to represent the probability amplitudes in the finite source. Assumming a random phase for each point in the source and noting that $a_s(0) = a_0(0) + \bar{a_0}(0)$ for K^0 and $\bar{K^0}$ in the initial state of the source, we represent the factor $a_s(0)e^{i\phi_1}$ in $\langle K_s|\Psi(k_A, t_A)\rangle$ as

$$\begin{aligned} a_s(0)e^{i\phi_1} &= D_{K^0}(x_1^\mu, k_A^\mu)\; e^{i\phi_{1K^0}} + D_{\bar{K^0}}(x_1^\mu, k_A^\mu)\; e^{i\phi_{1\bar{K^0}}} \\ &= \sum_{\xi = K^0, \bar{K^0}} D_\xi(x_1^\mu, k_A^\mu)\; e^{i\phi_{1\xi}} \end{aligned} \quad (6.8)$$

The production phases will be averaged over in the end to represent a completely incoherent source of neutral kaons. The projection of the two particle state will be

$$\begin{aligned}\left\langle K_s^1 K_s^2 | \Psi_{12} \right\rangle &= \frac{1}{2\sqrt{2}}\, e^{-\frac{t_A}{2\tau_s^A}} e^{-\frac{t_B}{2\tau_s^B}} \Big(\sum_{\xi=K^0,\bar{K}^0} D_\xi^{(1)}(x_1^\mu, k_A^\mu)\; e^{i\phi_{1\xi}} e^{ik_{A\mu}\cdot(x_A^\mu - x_1^\mu)} \\ &\quad \cdot \sum_{\xi'=K^0,\bar{K}^0} D_{\xi'}^{(2)}(x_2^\mu, k_A^\mu)\; e^{i\phi_{2\xi'}} e^{ik_{B\mu}\cdot(x_B^\mu - x_2^\mu)} \\ &\quad + \sum_{\xi=K^0,\bar{K}^0} D_\xi^{(1)}(x_2^\mu, k_A^\mu)\; e^{i\phi_{2\xi}} e^{ik_{A\mu}\cdot(x_A^\mu - x_2^\mu)} \\ &\quad \cdot \sum_{\xi'=K^0,\bar{K}^0} D_{\xi'}^{(2)}(x_1^\mu, k_A^\mu)\; e^{i\phi_{1\xi'}} e^{ik_{B\mu}\cdot(x_B^\mu - x_1^\mu)} \Big) \end{aligned} \tag{6.9}$$

The coherent sum(integral) over the finite source distribution, $\rho(x^\mu)$, is

$$\begin{aligned} F(k_A^\mu, k_B^\mu) &= \int\int d^4x_1 d^4x_2\; \rho(x_1^\mu) f(x_2^\mu) \left\langle K_s^1 K_s^2 | \Psi_{12} \right\rangle \\ &= \int\int d^4x_1 d^4x_2\; \frac{1}{2\sqrt{2}}\, e^{-\frac{t_A}{2\tau_s^A}} e^{-\frac{t_B}{2\tau_s^B}} \sum_\xi \sum_{\xi'} \\ &\quad \Big(f_\xi^{(1)}(x_1^\mu, k_A^\mu)\; e^{i\phi_{1\xi}} e^{ik_{A\mu}\cdot(x_A^\mu - x_1^\mu)} \\ &\quad \cdot f_{\xi'}^{(2)}(x_2^\mu, k_A^\mu)\; e^{i\phi_{2\xi'}} e^{ik_{B\mu}\cdot(x_B^\mu - x_2^\mu)} \\ &\quad + f_\xi^{(1)}(x_2^\mu, k_A^\mu)\; e^{i\phi_{2\xi}} e^{ik_{A\mu}\cdot(x_A^\mu - x_2^\mu)} \\ &\quad \cdot f_{\xi'}^{(2)}(x_1^\mu, k_A^\mu)\; e^{i\phi_{1\xi'}} e^{ik_{B\mu}\cdot(x_B^\mu - x_1^\mu)} \Big) \end{aligned} \tag{6.10}$$

where $f(x^\mu, k^\mu) = \rho(x^\mu) D(x^\mu, k^\mu)$. In order to follow more clearly the averaging over the random phases of the source functions, we introduce discrete summation over the source mesh points to get $\int d^4x_1 U(x_1^\mu, ...) = \sum_i \Delta x_i^4 U(x_i^\mu, ...)$ and similarly for x_2.

$$\begin{aligned} F(k_A^\mu, k_B^\mu) &\approx \frac{1}{2\sqrt{2}}\, e^{-\frac{t_A}{2\tau_s^A}} e^{-\frac{t_B}{2\tau_s^B}} \sum_{ij} \sum_{\xi\xi'} \\ &\quad \Big(f_\xi^{(1)}(x_i^\mu, k_A^\mu)\; e^{i\phi_{i\xi}} e^{ik_{A\mu}\cdot(x_A^\mu - x_i^\mu)} \\ &\quad \cdot f_{\xi'}^{(2)}(x_j^\mu, k_A^\mu)\; e^{i\phi_{j\xi'}} e^{ik_{B\mu}\cdot(x_B^\mu - x_j^\mu)} \\ &\quad + f_\xi^{(1)}(x_j^\mu, k_A^\mu)\; e^{i\phi_{j\xi}} e^{ik_{A\mu}\cdot(x_A^\mu - x_j^\mu)} \\ &\quad \cdot f_{\xi'}^{(2)}(x_i^\mu, k_A^\mu)\; e^{i\phi_{i\xi'}} e^{ik_{B\mu}\cdot(x_B^\mu - x_i^\mu)} \Big) \end{aligned} \tag{6.11}$$

With $S_\xi(x^\mu, k^\mu)$, the space-time distribution of particle type $\xi(= K^0 or \bar{K^0})$ with a weak parametric dependence on momentum and the function $g_\xi(k^\mu) = \sqrt{\frac{dN_\xi(k^\mu)}{d^4k}}$, the one body production amplitude for particle type ξ to final momentum state k^μ, the source functions are approximated as [74]

$$f_\xi(x^\mu, k_A^\mu) \cong S_\xi(x^\mu, k^\mu) g_\xi(k^\mu) \tag{6.12}$$

The source radii will depend on k_T, y, ϕ if transverse expansion, longitudinal expansion, and elliptic flow respectively are important. It is crucial to assume that $S_\xi(x^\mu, k_A^\mu) = S_\xi(x^\mu, k_B^\mu)$ since k_A^μ and k_B^μ are only relevant if close together in momentum space and since S_ξ only weakly depends on k^μ (i.e S_ξ varies with momentum over very large scales compared to the correlation scale in momentum space).

The probability amplitude for the particles to propagate from source to detectors is then given by

$$\begin{aligned}
P_{K_sK_s}(k_{A\mu}, k_{B\mu}) &= \frac{1}{2!}|F_{K_sK_s}(k_{A\mu}, k_{B\mu})|^2 \\
&= \frac{1}{16}\, e^{-\frac{t_A}{\tau_s^A}} e^{-\frac{t_B}{\tau_s^B}} \sum_{ijkl} \sum_{\xi\xi'\eta\eta'} \\
&\quad \Big[S_\xi(x_i^\mu) g_\xi(k_{A\mu}) S_{\xi'}(x_j^\mu) g_{\xi'}(k_{B\mu}) e^{i(\phi_{i\xi}+\phi_{j\xi'})} e^{-i(k_{A\mu}\cdot x_i^\mu + k_{B\mu}\cdot x_j^\mu)} \\
&\quad + S_{\xi'}(x_j^\mu) g_{\xi'}(k_{A\mu}) S_\xi(x_i^\mu) g_\xi(k_{B\mu}) e^{i(\phi_{j\xi}+\phi_{i\xi'})} e^{-i(k_{A\mu}\cdot x_j^\mu + k_{B\mu}\cdot x_i^\mu)} \Big] \\
&\quad \cdot \Big[S_\eta^*(x_i^\mu) g_\eta(k_{A\mu}) S_{\eta'}^*(x_j^\mu) g_{\eta'}(k_{B\mu}) e^{-i(\phi_{k\xi}+\phi_{l\xi'})} e^{i(k_{A\mu}\cdot x_i^\mu + k_{B\mu}\cdot x_j^\mu)} \\
&\quad + S_{\eta'}^*(x_j^\mu) g_{\eta'}(k_{A\mu}) S_\eta^*(x_i^\mu) g_\eta(k_{B\mu}) e^{-i(\phi_{l\xi}+\phi_{k\xi})} e^{i(k_{A\mu}\cdot x_j^\mu + k_{B\mu}\cdot x_i^\mu)} \Big]
\end{aligned} \tag{6.13}$$

The factor $\frac{1}{2!}$ in the probability amplitude is necessary since the propagation of particles 1 and 2 from points x_α^μ and x_β^μ are counted twice since we get $x_1^\mu = x_\alpha^\mu$,$x_2^\mu = x_\beta^\mu$ and $x_2^\mu = x_\alpha^\mu$,$x_1^\mu = x_\beta^\mu$ while doing the integrals. Only terms of the general form $S_\lambda(x_m^\mu) S_\lambda^*(x_m^\mu) S_{\lambda'}(x_{m'}^\mu) S_{\lambda'}^*(x_{m'}^\mu)$ will survive the average over random phases assumed

in the source functions $S(x^\mu)$. Note that $S_\lambda(x^\mu_m)S^*_\lambda(x^\mu_m)$ where $\lambda \neq \lambda'$ does not contribute since the K^0 and $\bar{K^0}$ are independent(assumption), even at the same point x^μ_m. If $i = k, j = l$ then $\xi = \eta, \xi' = \eta'$ contribute and if $i = l, j = k$ then $\xi = \eta', \xi' = \eta$ contribute and all other combinations vanish leaving only eight terms. Writing the $\xi = \xi'$ and $\xi \neq \xi'$ terms out explicitly one obtains

$$
\begin{aligned}
P_{K_sK_s}(k_{A\mu}, k_{B\mu}) = \frac{1}{16}\, & e^{-\frac{t_A}{\tau_s^A}} e^{-\frac{t_B}{\tau_s^B}} \sum_{ij}\sum_{\xi\xi'} \\
& \Big[S_\xi(x^\mu_i) g_\xi(k_{A\mu}) S_{\xi'}(x^\mu_j) g_{\xi'}(k_{B\mu}) S^*_\xi(x^\mu_i) g_\xi(k_{A\mu}) S^*_{\xi'}(x^\mu_j) g_{\xi'}(k_{B\mu}) \\
& + S_\xi(x^\mu_i) g_\xi(k_{A\mu}) S_{\xi'}(x^\mu_j) g_{\xi'}(k_{B\mu}) S^*_{\xi'}(x^\mu_j) g_{\xi'}(k_{A\mu}) S^*_\xi(x^\mu_i) g_\xi(k_{B\mu}) e^{-iq_\mu r^\mu} \\
& + S_\xi(x^\mu_i) g_\xi(k_{A\mu}) S_{\xi'}(x^\mu_j) g_{\xi'}(k_{B\mu}) S^*_{\xi'}(x^\mu_j) g_{\xi'}(k_{A\mu}) S^*_\xi(x^\mu_i) g_\xi(k_{B\mu}) e^{-iq_\mu r^\mu} \\
& + S_\xi(x^\mu_i) g_\xi(k_{A\mu}) S_{\xi'}(x^\mu_j) g_{\xi'}(k_{B\mu}) S^*_\xi(x^\mu_i) g_\xi(k_{A\mu}) S^*_{\xi'}(x^\mu_j) g_{\xi'}(k_{B\mu}) \\
& + S_{\xi'}(x^\mu_j) g_{\xi'}(k_{A\mu}) S_\xi(x^\mu_i) g_\xi(k_{B\mu}) S^*_\xi(x^\mu_i) g_\xi(k_{A\mu}) S^*_{\xi'}(x^\mu_j) g_{\xi'}(k_{B\mu}) e^{iq_\mu r^\mu} \\
& + S_{\xi'}(x^\mu_j) g_{\xi'}(k_{A\mu}) S_\xi(x^\mu_i) g_\xi(k_{B\mu}) S^*_{\xi'}(x^\mu_j) g_{\xi'}(k_{A\mu}) S^*_\xi(x^\mu_i) g_\xi(k_{B\mu}) \\
& + S_{\xi'}(x^\mu_j) g_{\xi'}(k_{A\mu}) S_\xi(x^\mu_i) g_\xi(k_{B\mu}) S^*_{\xi'}(x^\mu_j) g_{\xi'}(k_{A\mu}) S^*_\xi(x^\mu_i) g_\xi(k_{B\mu}) \\
& + S_{\xi'}(x^\mu_j) g_{\xi'}(k_{A\mu}) S_\xi(x^\mu_i) g_\xi(k_{B\mu}) S^*_\xi(x^\mu_i) g_\xi(k_{A\mu}) S^*_{\xi'}(x^\mu_j) g_{\xi'}(k_{B\mu}) e^{iq_\mu r^\mu} \Big] \\
= \quad & \frac{1}{16}\, e^{-\frac{t_A}{\tau_s^A}} e^{-\frac{t_B}{\tau_s^B}} \sum_{ij}\sum_{\xi\xi'} |S_\xi(x^\mu_i)|^2\, |S_{\xi'}(x^\mu_j)|^2 \\
& \times \Big[2\, (g_\xi(k_{A\mu}))^2 (g_{\xi'}(k_{B\mu}))^2 + 2\, (g_{\xi'}(k_{A\mu}))^2 (g_\xi(k_{B\mu}))^2 \\
& + 2\, g_\xi(k_{A\mu}) g_{\xi'}(k_{A\mu}) g_\xi(k_{B\mu}) g_{\xi'}(k_{B\mu}) \Big(e^{iq_\mu r^\mu} + e^{-iq_\mu r^\mu} \Big) \Big]
\end{aligned}
\tag{6.14}
$$

where $q_\mu = k_{A\mu} - k_{A\mu}$ is the four momentum difference and $r^\mu = x^\mu_i - x^\mu_j$ is the relative separation between the source points (i) and (j). Writing the $\xi = \xi'$ and $\xi \neq \xi'$ terms explicitly gives

$$
\begin{aligned}
P_{K_sK_s}(k_{A\mu},k_{B\mu}) &= \frac{1}{8}\; e^{-\frac{t_A}{\tau_s^A}} e^{-\frac{t_B}{\tau_s^B}} \sum_{ij} \\
&\Big[|S_{K^0}(x_i^\mu)|^2\; |S_{K^0}(x_j^\mu)|^2 (g_{K^0}(k_{A\mu}))^2 (g_{K^0}(k_{B\mu}))^2 \\
&+|S_{\bar{K^0}}(x_i^\mu)|^2\; |S_{\bar{K^0}}(x_j^\mu)|^2 (g_{|bar K^0}(k_{A\mu}))^2 (g_{\bar{K^0}}(k_{B\mu}))^2] \\
&\times(2+e^{iq_\mu r^\mu}+e^{-iq_\mu r^\mu}) \\
&+2[|S_{K^0}(x_i^\mu)|^2\; |S_{\bar{K^0}}(x_j^\mu)|^2 + |S_{\bar{K^0}}(x_i^\mu)|^2\; |S_{K^0}(x_j^\mu)|^2] \\
&\times[(g_{K^0}(k_{A\mu}))^2 (g_{\bar{K^0}}(k_{B\mu}))^2 + (g_{\bar{K^0}}(k_{A\mu}))^2 (g_{K^0}(k_{B\mu}))^2 \\
&+g_{K^0}(k_{A\mu}) g_{\bar{K^0}}(k_{A\mu}) g_{K^0}(k_{B\mu}) g_{\bar{K^0}}(k_{B\mu}) (e^{iq_\mu r^\mu}+e^{-iq_\mu r^\mu})\Big] \qquad (6.15)
\end{aligned}
$$

Replacing the sum with an integral over the space time points x_1^μ and x_2^μ, we obtain

$$
\begin{aligned}
P_{K_sK_s}(k_{A\mu},k_{B\mu}) &= \frac{1}{4}\; e^{-\frac{t_A}{\tau_s^A}} e^{-\frac{t_B}{\tau_s^B}} \int\int d^4x_1 d^4x_2 \\
&\Bigg(|S_{K^0}(x_1^\mu)|^2 |S_{K^0}(x_2^\mu)|^2\; \frac{dN(K^0)}{d^4k_A}\frac{dN(K^0)}{d^4k_B}\Big[1+\tfrac{1}{2}(e^{iq_\mu r^\mu}+e^{-iq_\mu r^\mu})\Big] \\
&+|S_{\bar{K^0}}(x_1^\mu)|^2 |S_{\bar{K^0}}(x_2^\mu)|^2\; \frac{dN(\bar{K^0})}{d^4k_A}\frac{dN(\bar{K^0})}{d^4k_B}\Big[1+\tfrac{1}{2}(e^{iq_\mu r^\mu}+e^{-iq_\mu r^\mu})\Big] \\
&+|S_{K^0}(x_1^\mu)|^2 |S_{\bar{K^0}}(x_2^\mu)|^2 \Big[\frac{dN(K^0)}{d^4k_A}\frac{dN(\bar{K^0})}{d^4k_B}+\frac{dN(\bar{K^0})}{d^4k_A}\frac{dN(K^0)}{d^4k_B}\Big] \\
&\cdot\Bigg(\Bigg[1+\frac{\sqrt{\frac{dN(K^0)}{d^4k_A}\frac{dN(\bar{K^0})}{d^4k_A}\frac{dN(K^0)}{d^4k_B}\frac{dN(\bar{K^0})}{d^4k_B}}}{\frac{dN(K^0)}{d^4k_A}\frac{dN(\bar{K^0})}{d^4k_B}+\frac{dN(\bar{K^0})}{d^4k_A}\frac{dN(K^0)}{d^4k_B}}\Bigg]\Bigg)(e^{iq_\mu r^\mu}+e^{-iq_\mu r^\mu})\Bigg)
\end{aligned} \qquad (6.16)
$$

The single particle production probability, assuming an average over source random phases which requires $S_\xi(\vec{x}_i)S_{\xi'}(\vec{x}_j) = |S_\xi(\vec{x}_i)|^2\delta_{ij}\delta_{\xi\xi'}$, will be

$$
\begin{aligned}
P_{K_s}(k_{A\mu}) &= |F_{K_s}(k_{A\mu})|^2 = \frac{1}{2}\sum_i\sum_\xi |S_\xi(x_i^\mu)|^2 |g_\xi(k_{A\mu})|^2\; e^{-\frac{t_A}{\tau_s^A}} \\
&= \frac{1}{2}\; e^{-\frac{t_A}{\tau_s^A}} \int d^4x_1 \Big[|S_{K^0}(x_1^\mu)|^2 \frac{dN(K^0)}{d^4k_A} + |S_{\bar{K^0}}(x_1^\mu)|^2 \frac{dN(\bar{K^0})}{d^4k_A}\Big] \qquad (6.17)
\end{aligned}
$$

The single neutral kaon production using the same source function and neutral kaon amplitude is

$$F_{K_s}(k_{A\mu}) = \frac{1}{\sqrt{2}} \sum_i \sum_\xi S_\xi(x_i^\mu) g_\xi(k_{A\mu})\ e^{-\frac{t_A}{2\tau_s^A}}\ e^{ik_{A\mu}(x_A^\mu - x_i^\mu)} \tag{6.18}$$

Hence the correlation function for K_sK_s is

$$C_2(q_\mu) = \frac{P_{K_sK_s}(k_{A\mu}, k_{B\mu})}{P_{K_s}(k_{A\mu}) P_{K_s}(k_{B\mu})} \tag{6.19}$$

Defining

$$\begin{aligned}
B_{\xi\xi'}(q_\mu) &= \int\int d^4x_1 d^4x_2 |S_\xi(x_1^\mu)|^2 |S_{\xi'}(x_1^\mu)|^2 \left(\frac{e^{iq_\mu r^\mu} + e^{-iq_\mu r^\mu}}{2}\right) \\
G_{K^0K^0} &= \frac{dN(K^0)}{d^4k_A}\frac{dN(K^0)}{d^4k_B} \\
H_{\bar{K}^0\bar{K}^0} &= \frac{dN(\bar{K}^0)}{d^4k_A}\frac{dN(\bar{K}^0)}{d^4k_B} \\
I_{K^0\bar{K}^0} &= \left[\frac{dN(K^0)}{d^4k_A}\frac{dN(\bar{K}^0)}{d^4k_A}\frac{dN(K^0)}{d^4k_B}\frac{dN(\bar{K}^0)}{d^4k_B}\right]^{\frac{1}{2}} \\
J_{K^0\bar{K}^0} &= \frac{dN(K^0)}{d^4k_A}\frac{dN(\bar{K}^0)}{d^4k_B} + \frac{dN(\bar{K}^0)}{d^4k_A}\frac{dN(K^0)}{d^4k_B}
\end{aligned} \tag{6.20}$$

The correlation function is written as

$$C_2(q_\mu) = 1 + \frac{B_{K^0K^0}(q_\mu) G_{K^0K^0} + B_{\bar{K}^0\bar{K}^0}(q_\mu) H_{\bar{K}^0\bar{K}^0} + 2B_{K^0\bar{K}^0}(q_\mu) I_{K^0\bar{K}^0}}{B_{K^0K^0}(0) G_{K^0K^0} + B_{\bar{K}^0\bar{K}^0}(0) H_{\bar{K}^0\bar{K}^0} + B_{K^0\bar{K}^0}(0) J_{K^0\bar{K}^0}} \tag{6.21}$$

If the K^0 and $\bar{K}^0$ source functions $S(x_\mu)$ and $\frac{dN}{d^4k}$ are identical, then

$$C_2(q_\mu) = 1 + \frac{B_{K^0K^0}(q_\mu)}{B_{K^0\bar{K}^0}(0)} \tag{6.22}$$

It remains to determine $B_{K^0K^0}(q_\mu)$ given the source function $S_{K^0}(x^\mu)$. For a Gaussian distribution $|S_{K^0}(x^\mu)|^2 = \frac{1}{(2\pi)^{\frac{3}{2}}\ R_{K^0}^3}\ e^{-\frac{x^2}{2R_{K^0}^2}} \cdot \frac{1}{\sqrt{2\pi}}\ e^{-\frac{t^2}{2\tau_{K^0}^2}}$ one obtains

$$C_2(q_\mu) = B_{K^0K^0}(q_\mu) = e^{-q^2R^2 - (q^0)^2\tau_{K^0}^2} \tag{6.23}$$

As can be seen from the last equation, the finite lifetime of the source mixes into the spatial distribution. In situations where statistics is not enough to do a full three

dimensional HBT analysis, one can fit the experimental correlation functions to a one dimensional Gaussian expression (assuming a Gaussian particle source)

$$C_2(q_{inv}) = 1 + \lambda \cdot e^{-q_{inv}^2 R_{inv}^2} \tag{6.24}$$

CHAPTER 7

THE RELATIVISTIC HEAVY ION COLLIDER (RHIC)

The Relativistic Heavy Ion Collider (RHIC) is located at Brookhaven National Laboratory in Upton, New York. The collider consists of hundreds of magnets which are joined into two circular rings enclosed in a tunnel 12 feet under the ground. Inside the magnets bunches of ions race around RHIC's 2.4-mile ring in opposite directions. The first successful operation of RHIC took place in the summer of year 2000, after ten years of development. RHIC accelerates ions up to a top energy of 100 GeV/nucleon. The maximum center of mass energy for beam-beam collisions is $\sqrt{S_{NN}} = 200 GeV/nucleon.$

The RHIC collider depends for its operation on other facilities each serving specialized purposes. A schematic diagram of the RHIC collider and its supporting facilities are shown in Figure (7.1). Acceleration of heavy and light ions starts at the Tandem Van de Graff (VDG) which consists of two 15 million volt electrostatic accelerators, each about 24 meters long, aligned end-to-end. The Tandem VDG provides beams of more than 40 different types of ions, by stripping off electrons from the corresponding atoms. Ions ranging from hydrogen to uranium are available and the Tandem gives billions of these ions a boost of energy. A Tandem-to-Booster transfer line accepts these energetic ions and sends them on their way towards the so-called Booster, a

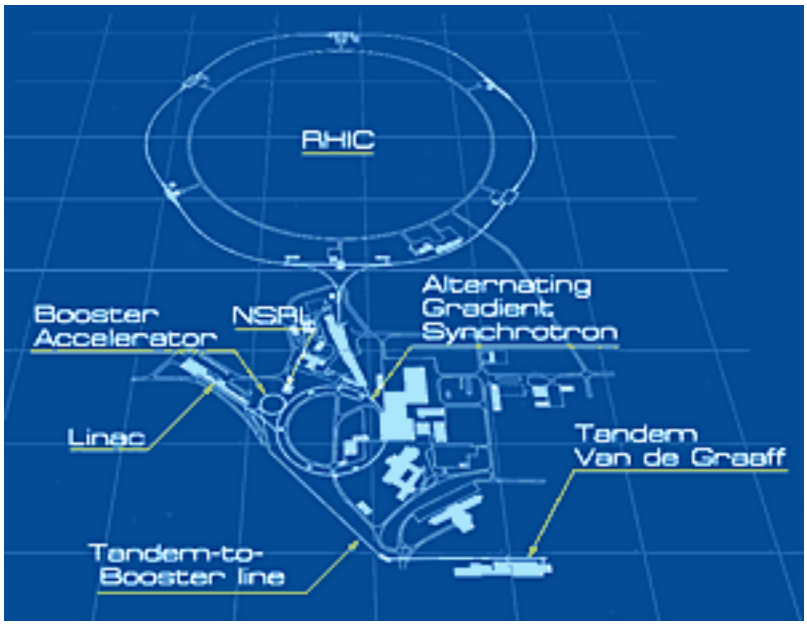

Figure 7.1: The Relativistic Heavy Ion Collider(RHIC).

powerful and compact circular accelerator, through a vacuum via a magnetic field. The ions will be moving at about 5% of the speed of light as they enter the Tandem. For experiments that use colliding beams of protons, energetic protons are transferred to the Booster after passing through the 200 million electron volt (MeV) Linear accelerator (Linac).

In being forced by magnets to travel around a circular storage ring, charged particles tangentially emit electromagnetic radiation and, consequently, lose energy. This energy is emitted in the form of light and is known as synchrotron radiation. The Booster synchrotron provides the ions more energy, by making them ride on the downhill slope of radio frequency electromagnetic waves. The ions are propelled forward at higher and higher speeds, getting closer and closer to the speed of light. The Booster

then feeds the beam into the Alternating Gradient Synchrotron (AGS) for further acceleration and delivery to RHIC. The Booster makes it possible for the AGS to accelerate and deliver heavy ions up to gold with its atomic mass of 197.

The Alternating Gradient Synchrotron (AGS) makes use of the concept of alternating gradient focusing, in which the field gradients of the accelerator's 240 magnets are successively alternated inward and outward, permitting particles to be propelled and focused in both the horizontal and vertical plane at the same time. Ions coming from the Booster into the AGS are traveling at about 37% the speed of light. The ions are accelerated at the AGS, until they are traveling at 99.7% the speed of light and then taken down another beam line called the AGS-To-RHIC (ATR) transfer line.

A switching magnet sends the ion bunches down one of two beam lines at the end of the ATR transfer line. The ion bunches are directed either left to the clockwise RHIC ring or right to travel counter-clockwise in the second RHIC ring. From here on, the counter-rotating beams are accelerated to the desired energy as they circulate in RHIC rings.

The particle beams are allowed to collide at the intersection points where the two rings of the accelerating magnets cross. The collisions produce the fleeting signals that are captured by one of RHIC's experimental detectors. Presently there are two small and two large experimental detectors at RHIC.

7.1 Overview of the RHIC experiments

One of the two smaller detectors is known as BRAHMS [75] which stands for "Broad Range Hadron Magnetic Spectrometer". The BRAHMS experiment studies

particles called charged hadrons as they pass through detectors called spectrometers. BRAHMS measures only a small number of particles emerging from a specific set of angles during each collision. The momentum, energy and other characteristics of the particles are measured very precisely.

The other small detector is the PHOBOS [76] detector which is able to measure quantities such as the temperature, size, and density of the fireball produced in the collision. The PHOBOS experiment looks for unusual events, such as fluctuations in the number of particles or angular distribution. It also studies the ratios of the various particles produced. With this information it should be possible to both detect and study a phase transition that might occur between quark-gluon plasma and ordinary matter. The PHOBOS group hopes to discover the quark-gluon plasma and learn more about the early universe.

One of the two large detector systems is the PHENIX (Pioneering High Energy Nuclear Interaction eXperiment) [77] detector. The PHENIX experiment records many different particles emerging from RHIC collisions, including photons, electrons, muons, and hadrons. Photons (particles of light) and leptons (electrons and muons) are not affected by the strong force, which binds quarks and gluons together into hadrons. Because they can emerge unchanged from the interior of a RHIC collision, photons and leptons carry unmodified information about processes within the collision.

The other big detector at RHIC is the Solenoidal Tracker At RHIC (STAR) [78]. The STAR detector was constructed to study the characteristics of strongly interacting matter at high energy density and to search for signatures of the QGP. Since this

thesis is based on data taken with the STAR detector, we will describe the STAR experiment in a little bit more detail in the next section.

7.2 The Solenoidal Tracker At RHIC (STAR)

Consisting of different sub-detectors each of which can be operated individually or all together, the STAR detector is a very versatile system capable of high precision tracking, momentum analysis, and particle identification. The layout of the STAR experiment [79] is shown in Figure (7.2).

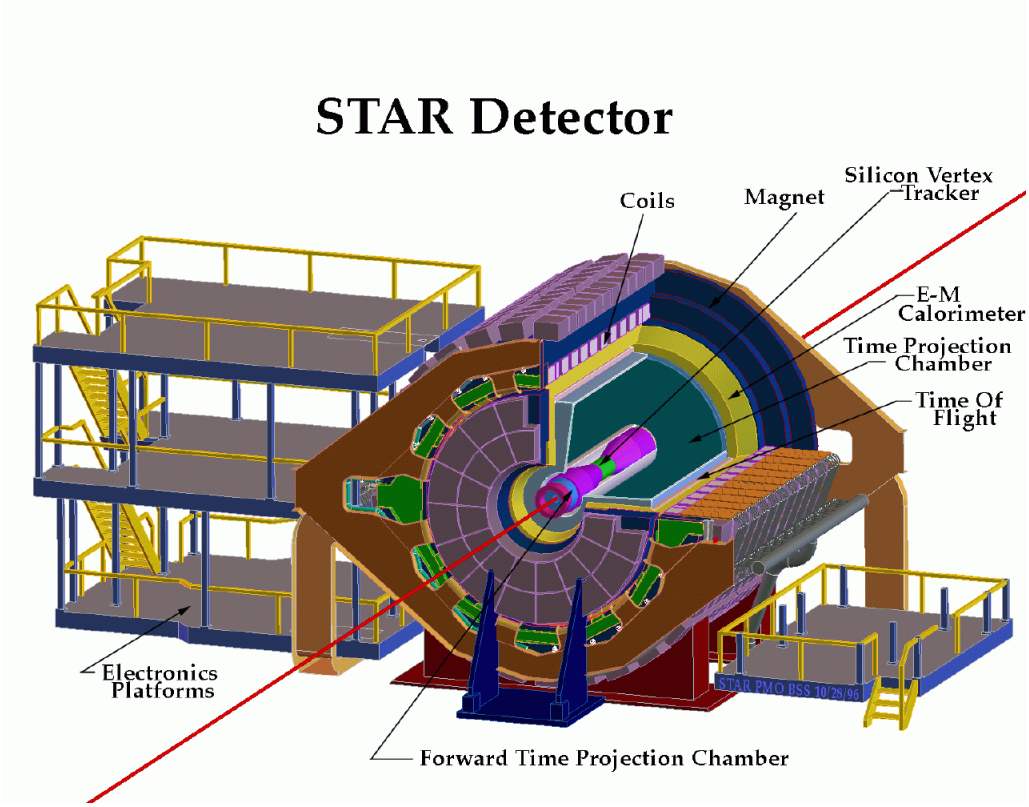

Figure 7.2: A schematic diagram of the STAR detector at RHIC.

A solenoidal magnet surrounding the interaction region provides the STAR detector with a uniform magnetic field upto $|Bz| = 0.5\ Tesla$ parallel to the beam axis. The primary charged particle tracking device is a gas filled cylindrical Time Projection Chamber(TPC). A central Trigger Barrel (CTB) around the TPC and and two Zero Degree Calorimeters (ZDC) provide triggering information for data taking. A Silicon Vertex Tracker (SVT) consisting of 216 silicon drift detectors provides charged particle tracking close to the interaction region.

7.2.1 The STAR Time Projection Chamber (TPC)

The STAR Time Projection Chamber (TPC), shown schematically in Figure (7.3), is 4.2 m long and has 0.5m inner radius and 2m outer radius. It has full azimuthal coverage around the beam line and provides complete tracking of charged particles within ± 1.8 units of pseudo-rapidity. The TPC is filled with P10 gas (10% methane, 90% argon) in a well defined uniform electric field provided by the outer field cage (OFC), the inner field cage (IFC), and the high voltage central membrane (CM).

The noble gas component has a very low affinity for free electrons while the organic gases quench the propagation of UV photons throughout the TPC volume. Quenching of the UV photons is important as they could produce electrons via the photoelectric effect distorting the signal from the electrons generated through ionization of the gas atoms by a primary track. The electrons from a primary track may drift as much as two meters before reaching the anode plane. So the gas must not attenuate these electrons and it must be kept pure to prevent other modes of electron loss due to attachment on oxygen and water molecules. Typically, the oxygen concentrations should be kept below a few hundred parts per million. This means the gas must be

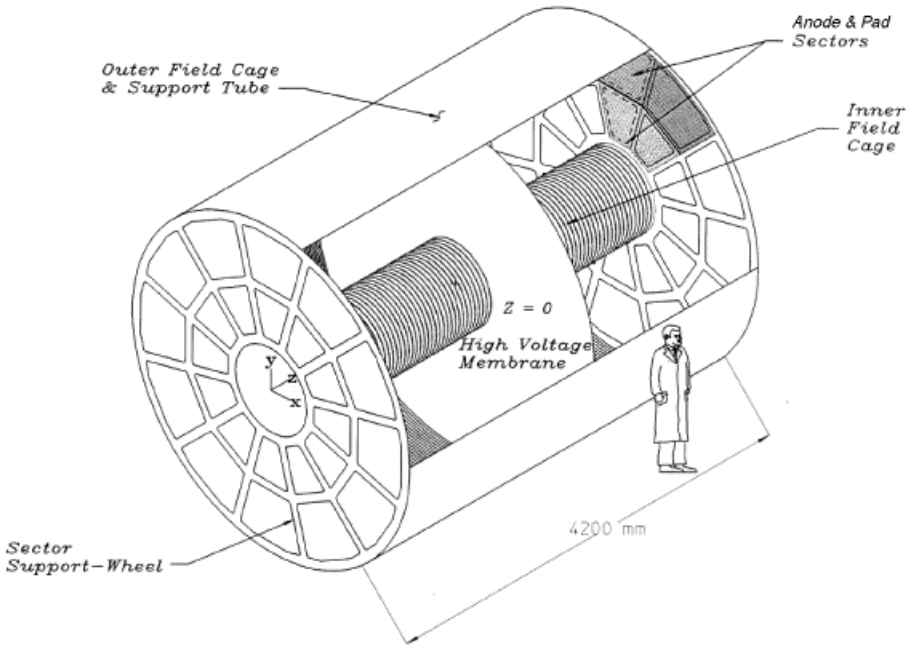

Figure 7.3: A schematic diagram of the STAR TPC.

easy to recirculate and clean in order to achieve these stringent standards. Noble gases are good candidates because they are easily cleaned with simple technologies and many pure organic gases are easily handled too. Examples are helium, argon, methane, ethane, and isobutane.

The OFC and the IFC together with the anode and pad planes define the active gas volume and were designed to contain the TPC gas and prevent it from being contaminated with outside air. The OFC and IFC include a series of gradient rings that divide the space between the central membrane and the anode planes. The central membrane is located in the middle of the TPC and is held at high voltage. The anode and pad planes are organized into sectors on each end of the TPC and

the pads are held at ground potential. The total distance from the CM to either anode plane is slightly greater than 2 meters. There is approximately one ring per centimeter and the rings are biased by a chain of resistors that connect to the CM, the anode plane ground, and each of the gradient rings in between. The rings are separated by 2 MΩ resistors and there are 182 rings and 183 resistors in each chain.

A charged particle passing through the TPC leaves a trail of electrons via ionization of the gas atoms. Since the central membrane divides the TPC in half, the electrons in one half of the chamber drift to the nearest readout pads on the endcaps. Figure (7.4) shows an end view of a typical event from a central Au-Au collision measured by the STAR detector.

7.2.2 The STAR Trigger Detectors

The STAR trigger detectors [80] provide information that is used to determine whether to begin the amplification-digitization-acquisition(ADA) cycle for the slower detectors such as the TPC and the SVT. The main trigger detectors in the 2001 run are the Central Trigger Barrel(CTB) surrounding the TPC, two Zero Degree Calorimeters (ZDC) which are placed at nearly identical positions along the beam lines on either side of the intersection regions, multi-wire proportional counters (MWC) which consists of the anode wires at the two ends of the TPC.

The CTB measures charged particle multiplicity in the pseudo-rapidity range $-1 < \eta < 1$ and 2π in azimuthal angle ϕ. The ZDC's measure neutron multiplicity in a small solid angle near zero degrees. Comparison of the time from the two ZDC's gives a measure of the interaction location. The MWC makes use of the ionization

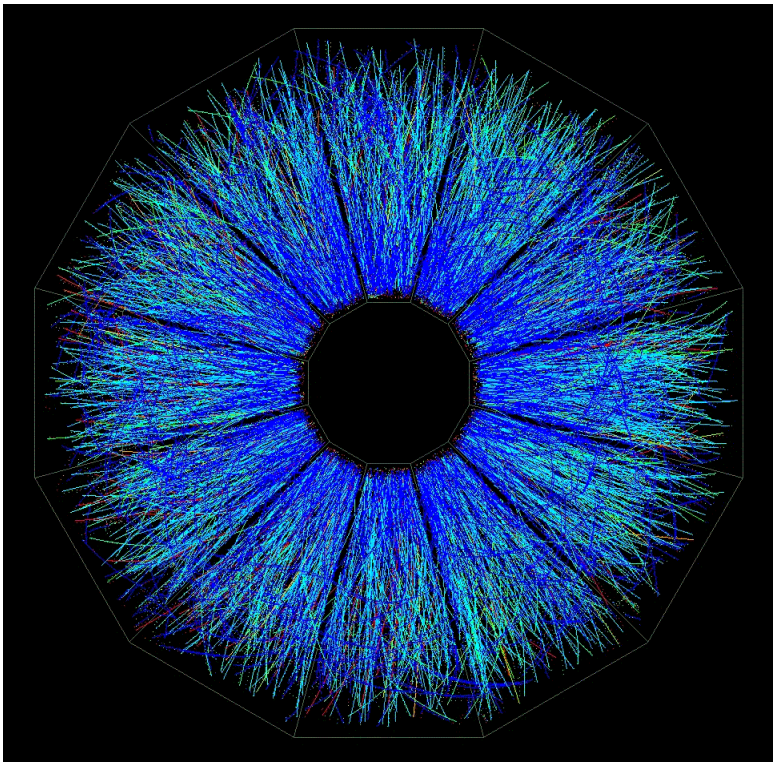

Figure 7.4: An end view of tracks in the STAR TPC.

from the charged tracks that pass through the anode wire region causing avalanches onto the wires. These signals can be used to measure the multiplicity of such tracks.

7.2.3 The STAR Silicon Vertex Tracker (SVT)

The SVT detector system [81] consists of 216 Silicon Drift Detectors(SDD) arranged on three cylindrical barrels at distances of approximately 7, 11, and 15 cm from the beam axis. The outer barrel is located at 14.91 cm, the middle barrel at 10.16 cm and the inner barrel at 5.97 cm from the beam line. The SVT provides a pseudo-rapidity coverage of $|\eta| \leq 1$ and full azimuthal symmetry ($\Delta\phi = 2\pi$). The close proximity of the SVT to the beam axis allows for precision localization of the

primary interaction vertex and makes it possible to identify secondary vertices from weak decays of particles like Λ, Σ, and Ω.

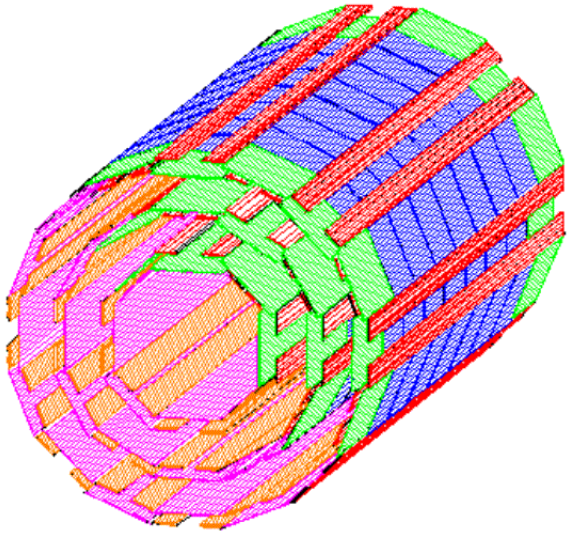

Figure 7.5: A schematic diagram of the STAR SVT detector.

The SVT will provide substantial improvement in the momentum resolution for high p_t particles and also enhance track reconstruction and particle identification for soft charged particles such as $\pi^{\pm}, K^{\pm}, p$, and $\bar{p}$. The excellent two track resolution of the detector also allows for a unique capability to carry out two particle interferometry (HBT) studies.

CHAPTER 8

THE SLOW SIMULATOR AND CLUSTER FINDER FOR THE SILICON VERTEX TRACKER (SVT)

8.1 Introduction

For several years semiconductors have been used as high resolution position sensing detectors in various experiments. The concept of a semiconductor drift chamber was first proposed by Gatti and Rehak [82, 83]. The novel feature of such a device is the transport of electrons parallel to large surfaces of the detector onto a small area anode connected to the input of an amplifier. Figure (8.1) shows a schematic diagram of what a silicon drift detector looks like.

A charged particle passing through the SDD leaves a cloud of electron-hole pairs. The elctric field configuration inside the detector is such that the electrons are focused into the center plane of the detector and drifted in this plane towards the anode. The potential energy of the electrons is shown in Figure (8.2). The potential does not depend on the z coordinate along the rectifying junction making the potential problem two-dimensional. The potential has to satisfy Poisson's equation

$$\frac{\partial^2(-\phi)}{\partial^2 x} + \frac{\partial^2(-\phi)}{\partial^2 y} = \frac{N_d q}{\epsilon_o \epsilon_r} \tag{8.1}$$

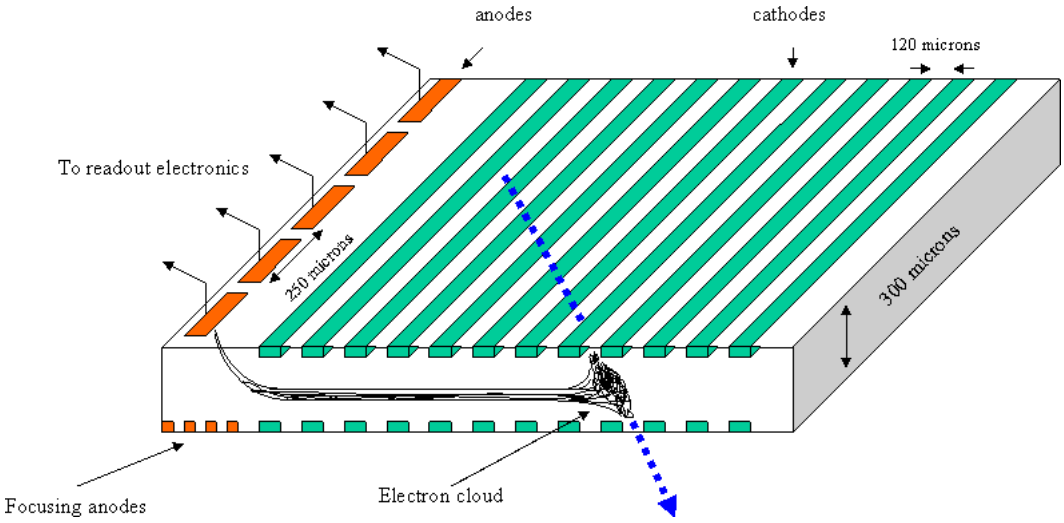

Figure 8.1: Principles of semiconductor drift detectors.

where N_d is the density of ionized donors in silicon bulk, ϵ_r is the relative dielectric constant, q is the elctronic charge and ϵ_o is the permeability respectively. The potential shown in Figure (8.2) is a close realization of an ideal case where the solution of Eq. (8.1) is a sum of a linear potential along y(drift coordinate) and a parabolic along x(focussing coordinate). x_o is the x coordinate of the minimum of the potential energy and E_d is the drift field. The elctric field has a different shape in the region of the detector close to the anode. Here the minimum of the electron potential energy is shifted from the central plane toward the anode side of the detector allowing for charge collection.

$$-\phi_i(x,y) = \frac{N_d q}{\epsilon_o \epsilon_r}(x - x_o)^2 + E_d y \tag{8.2}$$

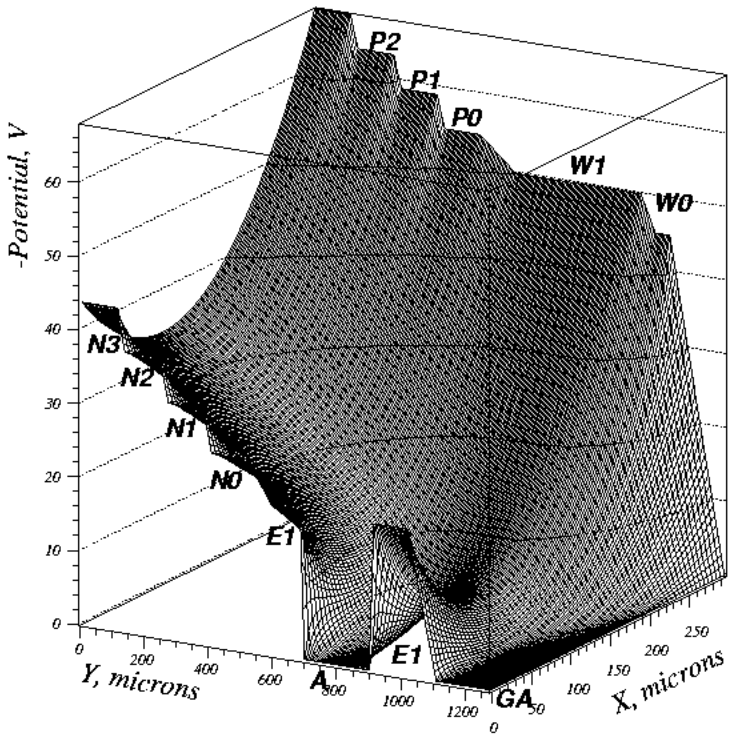

Figure 8.2: Potential energy of electrons in a linear drift detector.

8.2 The SVT detector

The Silicon Vertex Tracker (SVT) employs the technology of drift detectors for its operation. As mentioned in the previous chapter, the SVT detector consists of three concentric barrels of Silicon Drift Detectors (SDD) called wafers around the beam pipe. Figure (8.3) shows half of the actual SVT detector

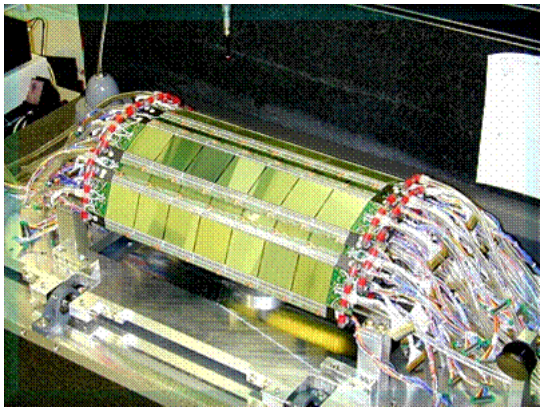

Figure 8.3: The actual SVT detector. Only half of the whole detector is shown.

Being the innermoset detector and closest to the beam line, the SVT allows for a good determination of the primary vertex and identifying short lived particles that decay before they reach the TPC. Due to its close proximity to the beam pipe, the SVT extends the tracking ability of STAR by measuring particles that cannot make it to the TPC due to their low momentum.

The passage of a charged particle through the SVT detector leaves behind a cloud of electron-hole pairs on each SDD the particle crosses. The electron clouds are forced to the mid planes of the SDDs by potentials applied to their outer faces and drift towards the collecting anodes under the influence of a linearly varying potential. Focusing of the cloud onto the anodes is accomplished by a suitably adjusted electric field configuration.

Each SVT wafer has a central cathode across it maintained at -1500 V and the edges of the wafer are kept at 0 V. This arrangement divides the wafer into two oppositely directed drift regions. The top and bottom cathods are supplied with

the same potential providing the bias voltage necessary to create the depleted region througout the thickness of the silicon. From the central cathode the voltage is stepped down linearly in both directions creating the drift field required to transport the electrons towards the edges of the wafer where the collecting anodes are located. The charge collection area consists of 240 $n+$ implanted anodes.

The expansion of the electron cloud due to diffusion and coulomb repulsion causes the charge to be spread out over many anodes [84]. The small geometric size of the anode and complete depletion of the silsicon bulk result in small input capacitance at the anodes. The SDDs are provided with Front-End Electronics (FEE) to amplify and shape the signals before storing them. The FEEs are designed to minimize the noise introduced into the measurement of the time of arrival and charge information at the anodes. The low input capacitance permits a fast preamplifier-shaper response due to a lower (capacitance dependent) series noise. Good separation of charge from two hits arriving on the same anode(two track resolution) requires a fast impulse response. The expected separations and widths of adjecent hits determine how fast the response should be and in the case of the SVT correspondes to a rise time of $50ns(10-100\%)$. The Pre Amplifier ShAper (PASA) for the SVT is thus implemented in bipolar technology due to its very good noise-power performance at such clocking speeds. A Swith Capacitor Array (SCA) carries out wave form sampling providing both timing and dE/dx information. The number of required samples is determined by $N \times 1/f > t_d$ where N is the number of samples, f is the sampling frequency and t_d is the total drift time. A total drift time of about $4.5\mu s$ and a frequency of sampling around 25 MHz suggest $N > 112$. The SCA thus samples the output from the PASA and sequentially stores the signal on one of the 128 (a number easily implemented as

a power of two) capacitors in the array. Since the sampling is continuous, the SCA capacitors are constantly overwritten with new data from the SDD. At the onset of a trigger signal, the SCA samples for a total drift time after which it connects its capacitors to an output driver, which transmits the capacitor values onto the analog signal line at the rate of 1.6 MHz.

8.3 The Svt Slow Simulator

The particular point through which the particle passes on the detector is what we call a HIT. The most important task in particle tracking is to be able to find the hits associated with particles crossing through the detector. This is usually accomplished using a hit reconstruction software. However, one would like to be sure if a given reconstructed hit realy belongs to an actual particle track. Thus, it is necessary to have a software to simulate a hit given the energy a particle deposits on the detector and the position of the crossing point. For this purpose, a Slow Simulator for the SVT detector has been coded in C++. Starting with hits whose positions momenta and corresponding energies are already known, the code generates electron clouds, determines their initial widths and propagates them over the drift time of the actual SDD and calculates their apparent widths at the anodes. Once the signals reach the anodes, they are digitized and the data is stored in the same format as for the real SVT data.

The signal shape when the cloud arrives at the anodes is determined by the PASA response function [85] which is given by

$$f(t) = \frac{b}{c^5}e^{-bt} + e^{-at}[\frac{-b}{c^5} + \frac{b}{c^4}t - \frac{b}{2c^3}t^2 + \frac{b}{6c^2}t^3 - \frac{a}{24c}t^4] \tag{8.3}$$

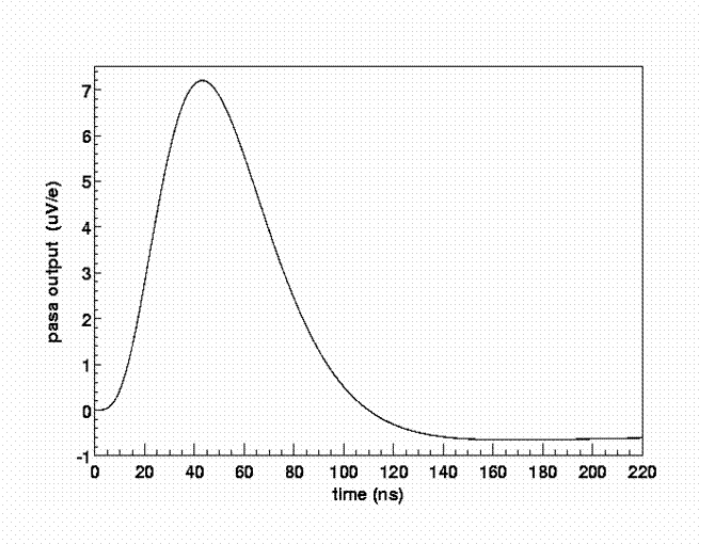

Figure 8.4: Simulation of the PASA response function.

where $a = \frac{1}{\tau_s}$, $b = \frac{1}{\tau_l}$ and $c = b - a$. The parameters $\tau_s = 11.5\ ns$ and $\tau_l = 500\ ns$ correspond to the short and long time components of the PASA response function used for the SVT at STAR. The output signal is given by

$$A(t) = \int_{-\infty}^{t} \frac{dq'}{dt'} f\left(t - t_c'\right) \tag{8.4}$$

which is nothing but a convolution of the input signal with the PASA response function [86]. It is clear from Eq.(8.4) that the PASA response function is simply the output for a delta function input.

Since 2-dimensional position information is what is needed, it is necessary to know for how long a given electron cluod has been drifting before collection at the anodes. The SVT Slow Simulator starts by putting a hit at a specified position on the SDD.

It then forms an electron cloud at that point by converting the energy deposited by the particle into a two dimensional charge signal.

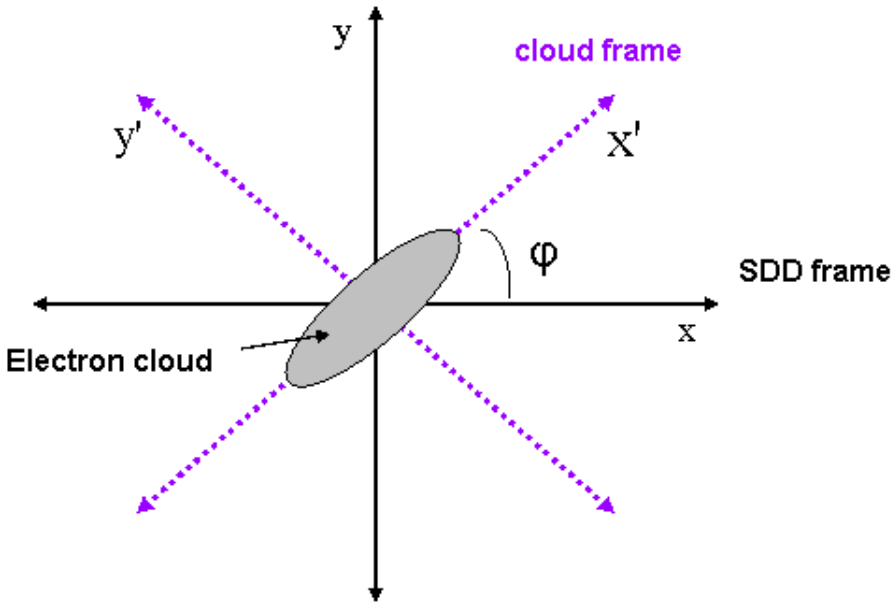

Figure 8.5: Projection of the electron cloud onto the SDD plane for a charged particle that crosses the SDD at angle to the normal. For perpendicular crossing, the cloud will assume a disc shape.

In the frame with respect to the cloud itself, called the principal axes frame, the electron cloud is assumed to be a two dimensional gaussian with the principal axes parallel (x') and perpendicular (y') to the initial projection of the track onto the SDD plane.

$$\frac{dq}{dxdy} = \frac{Q_o}{2\pi\sigma_x\sigma_y} exp\left(-\frac{(x-x_c)^2}{2\sigma_x^2} - \frac{(y-y_c)^2}{2\sigma_y^2}\right) \tag{8.5}$$

where the point (x_c, y_c) denotes the centroid of the cloud. The time dependence of the charge arriving at a given anode is then given by

$$\frac{dq\,(t)}{dt} = \frac{Q_o}{2\pi\sigma_x\,(t_c)\,\sigma_t\,(t_c)}\;exp\left(-\frac{(t-t_c)^2}{2\sigma_t^2\,(t_c)}\right) \tag{8.6}$$

Signals are generated numerically since the analytical form of the PASA convolution integral does not give the desired result for relatively large widths of input signal. The SDD frame is related to the principal axes frame through the transformation equations

$$\begin{aligned} x &= x'\;cos\theta - y'\;sin\theta \\ y &= x'\;sin\theta + y'\;cos\theta \end{aligned} \tag{8.7}$$

The rms widths of the electron cloud (σ_x, σ_y) in the SDD frame are given by

$$\begin{aligned} \sigma_x^2 &= \int dxdy\;x^2\;f\,(x', y') \\ \sigma_y^2 &= \int dxdy\;y^2\;f\,(x', y') \end{aligned} \tag{8.8}$$

where

$$f\,(x', y') = \frac{1}{2\pi\sigma_{x'}\sigma_{y'}}\;exp\left(-\frac{(x')^2}{2\sigma_{x'}^2} - \frac{(y')^2}{2\sigma_{y'}^2}\right) \tag{8.9}$$

The distribution function in Eq. (8.9) is normalised to 1. $\sigma_{x'}$ measures the longer width of the cloud parallel to the projection of the track onto the SDD and $\sigma_{y'}$ is the width in the perpendicular direction which is very small and taken to be 0.001 μs in the simulation. For perpendicular crossing the electron cloud starts from a point and is thus given small equal initial widths in both directions. Since the jacobian of the

transformation between the two frames is 1, we use $dxdy = dx'dy'$ for the integration measure together with Eqs.(8.8) to get

$$\begin{aligned}
\sigma_x^2 &= \frac{1}{2\pi\sigma_{x'}\sigma_{y'}}\int dx'dy' \left[(x')^2 cos^2(\phi) + (y')^2 sin^2(\phi) \right. \\
&\quad \left. - x'y' sin(2\phi) \right] exp\left(-\frac{(x')^2}{2\sigma_{x'}^2} - \frac{(y')^2}{2\sigma_{y'}^2} \right) \\
&= \sigma_{x'}^2 cos^2(\phi) + \sigma_{y'}^2 sin^2(\phi) \qquad (8.10)
\end{aligned}$$

$$\begin{aligned}
\sigma_y^2 &= \frac{1}{2\pi\sigma_{x'}\sigma_{y'}}\int dx'dy' \left[(x')^2 sin^2(\phi) + (y')^2 cos^2(\phi) \right. \\
&\quad \left. + x'y' sin(2\phi) \right] exp\left(-\frac{(x')^2}{2\sigma_{x'}^2} \frac{(y')^2}{2\sigma_{y'}^2} \right) \\
&= \sigma_{x'}^2 sin^2(\phi) + \sigma_{y'}^2 cos^2(\phi) \qquad (8.11)
\end{aligned}$$

$$\begin{aligned}
\sigma_{xy}^2 &= \frac{1}{2\pi\sigma_{x'}\sigma_{y'}}\int dx'dy' \left[(x')^2 cos(\phi) sin(\phi) \right. \\
&\quad + x'y' cos^2(\phi) - x'y' sin^2(\phi) \\
&\quad \left. - (y')^2 sin(\phi) cos(\phi) \right] exp\left(-\frac{(x')^2}{2\sigma_{x'}^2} - \frac{(y')^2}{2\sigma_{y'}^2} \right) \\
&= \frac{1}{2}\left(\sigma_{x'}^2 - \sigma_{y'}^2 \right) sin^2(\phi) \qquad (8.12)
\end{aligned}$$

Eqs.(8.10-8.12) suggest the following expressions for the time dependence of the rms widths in the SDD frame in terms of those in the principal axes frame

$$\begin{aligned}
\frac{d\sigma_x^2}{dt} &= \frac{1}{2}[\left(\frac{d\sigma_{x'}^2}{dt} + \frac{d\sigma_{y'}^2}{dt} \right) + \left(\frac{d\sigma_{x'}^2}{dt} - \frac{d\sigma_{y'}^2}{dt} \right) cos(2\phi)] \\
\frac{d\sigma_x^2}{dt} &= \frac{1}{2}[\left(\frac{d\sigma_{x'}^2}{dt} + \frac{d\sigma_{y'}^2}{dt} \right) - \left(\frac{d\sigma_{x'}^2}{dt} - \frac{d\sigma_{y'}^2}{dt} \right) cos(2\phi)] \\
\frac{d\sigma_{xy}^2}{dt} &= \frac{1}{2}\left(\frac{d\sigma_{x'}^2}{dt} - \frac{d\sigma_{y'}^2}{dt} \right) sin(2\phi) \qquad (8.13)
\end{aligned}$$

where

$$\frac{d\sigma_{x'}^2}{dt} = 2D_{x'} + f_1(\sigma_{x'}, \sigma_{y'}), \qquad \frac{d\sigma_{y'}^2}{dt} = 2D_{y'} + f_2(\sigma_{x'}, \sigma_{y'}) \qquad (8.14)$$

The quantities $D_{x'}$ and D'_y are diffusion constants in the principal axes frame. The functions $f_1(\sigma_{x'}, \sigma_{y'})$ and $f_2(\sigma_{x'}, \sigma_{y'})$ [88], which account for the coulomb expansion of the electron cloud are given by

$$\begin{aligned} f_1(\sigma_{x'}, \sigma_{y'}) &= \frac{\mu Q}{4\pi\epsilon_o\epsilon}\left(\frac{K_1\left(\frac{\sigma_{y'}}{\sigma_{x'}}\right) - \frac{K_3}{4}\ln[\left(\frac{\sigma_{y'}}{\sigma_{x'}}\right)^4 + [1+\left(\frac{d}{\sigma_{y'}}\right)^2]^{-2}]}{\sigma_{x'}[1+(\frac{K_1\sigma_{y'}}{K_2 d})^3]^{\frac{1}{3}}}\right) \\ f_2(\sigma_{x'}, \sigma_{y'}) &= \frac{\mu Q}{4\pi\epsilon_o\epsilon}\left(\frac{K_3 - (K_3-K_1)\left(\frac{\sigma_{y'}}{\sigma_{x'}}\right)^{\frac{1}{2}}}{\sigma_{x'}[1+(\frac{K_1\sigma_{y'}}{K_2 d})^3]^{\frac{1}{3}}}\right) \end{aligned} \tag{8.15}$$

where d is the anode size, and K_1, K_2 and K_3 are constants. In the absence of Coulomb effects, one gets the familiar expression $\sigma = \sqrt{2Dt}$ which is the width due to diffusion only. Defining $D_x = D_{x'}cos^2(\phi) + D_{y'}sin^2(\phi)$ and $D_y = D_{x'}sin^2(\phi) + D_{y'}cos^2(\phi)$, Eqs.(8.13) are written as

$$\begin{aligned} \frac{d\sigma_x^2}{dt} &= 2D_x + \frac{1}{2}[(f_1(\sigma_{x'}, \sigma_{y'}) + f_2(\sigma_{x'}, \sigma_{y'})) \\ &\quad + (f_1(\sigma_{x'}, \sigma_{y'}) - f_2(\sigma_{x'}, \sigma_{y'}))cos(2\phi)] \\ \frac{d\sigma_y^2}{dt} &= 2D_y + \frac{1}{2}[(f_1(\sigma_{x'}, \sigma_{y'}) + f_2(\sigma_{x'}, \sigma_{y'})) \\ &\quad - (f_1(\sigma_{x'}, \sigma_{y'}) - f_2(\sigma_{x'}, \sigma_{y'}))cos(2\phi)] \\ \frac{d\sigma_{xy}^2}{dt} &= 2\left(D_x sin^2(\phi) + D_y cos^2(\phi)\right)tan(2\phi) \\ &\quad + \frac{1}{2}(f_1(\sigma_{x'}, \sigma_{y'}) - f_2(\sigma_{x'}, \sigma_{y'}))sin(2\phi) \end{aligned} \tag{8.16}$$

8.4 The Svt Cluster Finder

At the heart of the SVT hit reconstruction software is the so called cluster finder. As the signal is sampled 128 times for each of the 240 anodes, the detector may be viewed as a rectangular grid of 128×240 cells referred to as "pixels". A cluster is

defined as a set of pixels in contact with each other and having signals. A cluster may be generated either by a particle crossing or by noise in the detector itself. For a given anode, a set of consecutive pixels with signal on them form what is called a sequence. The cluster finder uses sequences which are in contact with each other to make a cluster. An array of integers where each integer stands for one of the 240 anodes with sequences on it is used in the search for sequences which have adjecent neighbors.

The search is alwayes started from the left with the first sequence from the first element of the anode array and keeps a record of the anode number and the sequence number in a two dimensional array. This sequence is considered as the first member of a cluster. The following actions are then performed:

1) The cluster finder tags this sequence and looks at sequences on the immediate right and left listanodes. Whenever a new adjecent sequence is found, it is tagged and a record of its sequence number and the corresponding listanode number is kept.

2) While tagged members on left and right are ignored,the process in (1) is repeated for each one of the newly found members in search of other new ones. This continues until no further new members are found at which point the cluster finder says " the first cluster is found ,it is time to look for the next one... "

3) The finder goes back to the first element in the list and searchs for a sequence which is not tagged and when it findes one it repeates steps (1) and (2). If all sequences on the first anode are tagged it immediately passes to the second element to get a sequence and processes (1) and (2) are carried out again. If the actual anode numbers on the list are not consecutive while looking on the left for a given index,

the index is marked so that subsequent searchs for an untagged sequences start there to go on with the next cluster finding.

Once the cluster finding process is over, moment analysis of the clusters is carried out in order to determine their centroid positions with respect to the SDD frame. After the hit positions are reconstructd locally, a coordinate transformation to global position coordinates with respect to the STAR detector is finally done and the data is ready for further analysis.

8.5 Results from the SVT slow simulator

The energy deposited by a minimum ionizing particle (MIP) is approximately 96000 eV. The energy required to make an electron hole pair in silicon is about 3.6 eV. So we expect around $96000/3.6 \approx 25000$ electrons to be liberated by the passage of an MIP through the SDD. Signals are generated numerically since the analytical form of the PASA convolution integral does not give the desired result for relatively large widths of input signal. The important parameters for the simulation are summarized in Table (8.1).

parameter	value
Electron mobility	0.135 e/V-mm
Drift velocity	6.75 mm/μs
Diffusion constant	0.0035 mm^2/μs
Dielectric constant	12.0

Table 8.1: Constants for the Silicon Drift Detector

The code produces very well the PASA output for a gaussian input signal up to widths of 0.4 μs. For a consistency check, the signal generating part of a fortran code [88] which gives results upto signal widths of 0.23 μs, has also been converted into C++ and incorporated into the slow simulator software. But,the signals from the two codes start to differ for widths above around 0.15 μs as shown in Figures (8.6 c, 8.6 d). The difference comes from numerical problems associated with parameters in the fortran version which have been tuned to work with signals having widths over a limited range of values.

Particle tracking in a given detector depends on how well one reconstructs hit positions. Plots (a) and (b) in Figure (8.7) show distributions of residuals (differences between input and reconstructed positions) in drift and anode directions respectively. The distribution in the drift direction is not centered around zero due to the shift introduced by the rise time of the PASA responce function. Gaussian fits to the distributions give widths less than 25 μm in both directions. This is in agreement with positions resolutions measured by the STAR-SVT collaboration [89] using electrons generated by light pulse from a laser. The group also carried out a study of the cloud shape dependence on the drift time. Figure (8.7 c) shows the evolution of the electron cloud as a function of drift time. The line through the data points is the solution of the continuity equation [84] that takes into account drift, diffusion and Coulomb repulsion. The dashed lines show the evolution of the cloud width due to diffusion only. The dependence of the width on drift time for the case of Coulomb repulsion is shown by the dotted line. One can see that the contribution of the Coulomb interaction is significant at short drift times while the cluod size is small. Diffusion is the dominant effect for large drift times. Figure (8.7 d) shows the dependence of

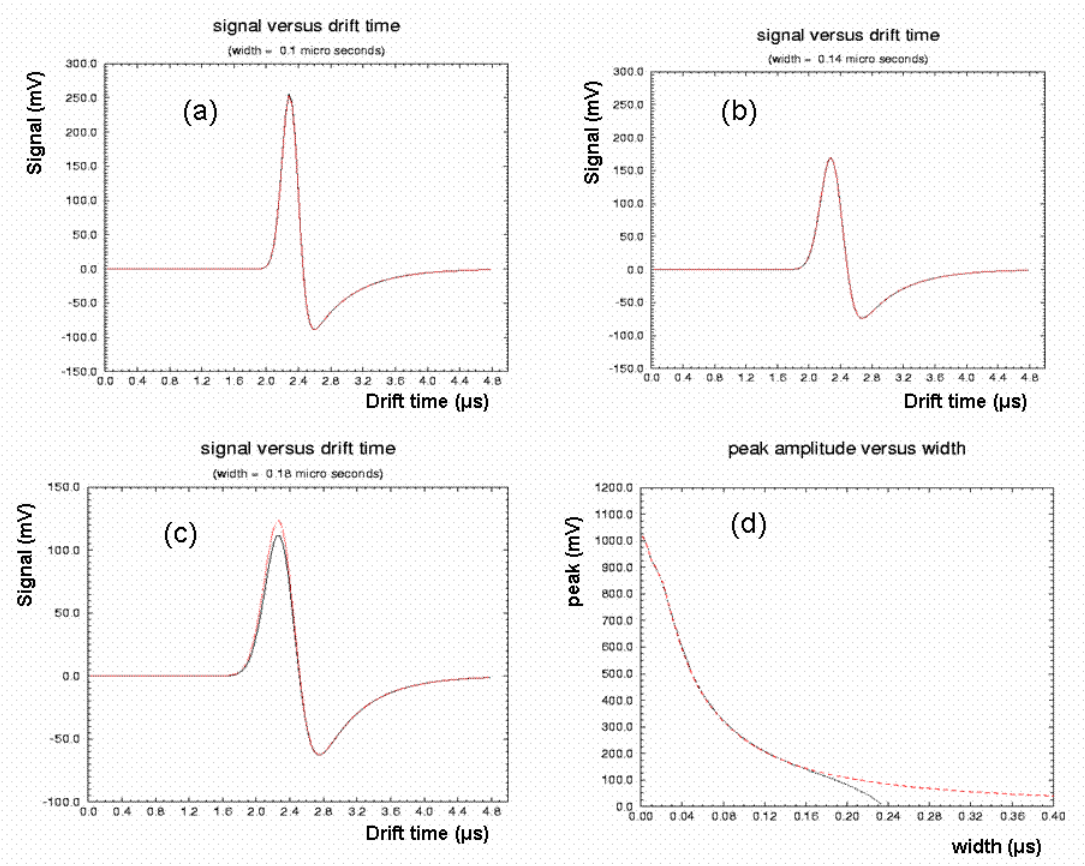

Figure 8.6: Examples of a gaussian signal convoluted with the PASA response function. The red curves show the results from the svt slow simulator. The black curves correspond to results obtained with a previous fortran code. One can see the agreement up to input widths of 0.15 μs.

the electron cloud width on drift distance from data (upper points) and simulaton (lower points) for the STAR SVT detector. One can see that the width increases with drift distance in general. The width seems to be unusually large even for small drift times which is not what one sees in the laser spot measurement. One possible reason for such large initial widths may be the difficulty to accurately determine widths for hits that fall on the edge of the detector close to the anodes and so span only one or

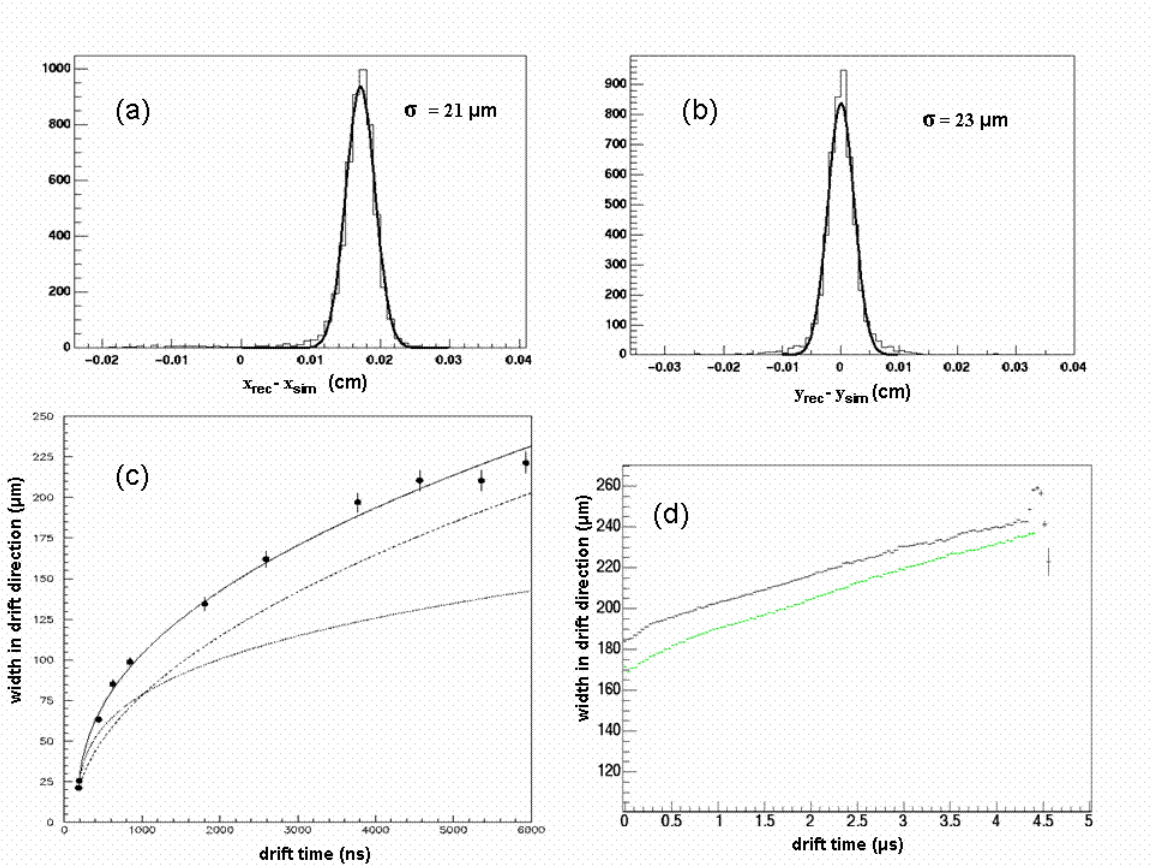

Figure 8.7: (a) position resolution in drift direction, (b) position resolution in anode direction, (c) dependence of the cloud size on drift time (points are data), (d) width in drift direction from the STAR SVT detector (upper points are data, and lower pionts are from simulation).

two bins in the drift directions. It is also possible that trapping-detrapping processes affect the dynamics of the electron cloud during the whole drift time.

Based on Eqs. (8.16), a simulation of the signal left in the SDD by a particle was carried out. Figure (8.8) shows the dependence of the cloud width on time as it propagates the full drift length of the SDD. One can again see that coulomb repusion is important during the initial stages of the drift and gets weaker as the

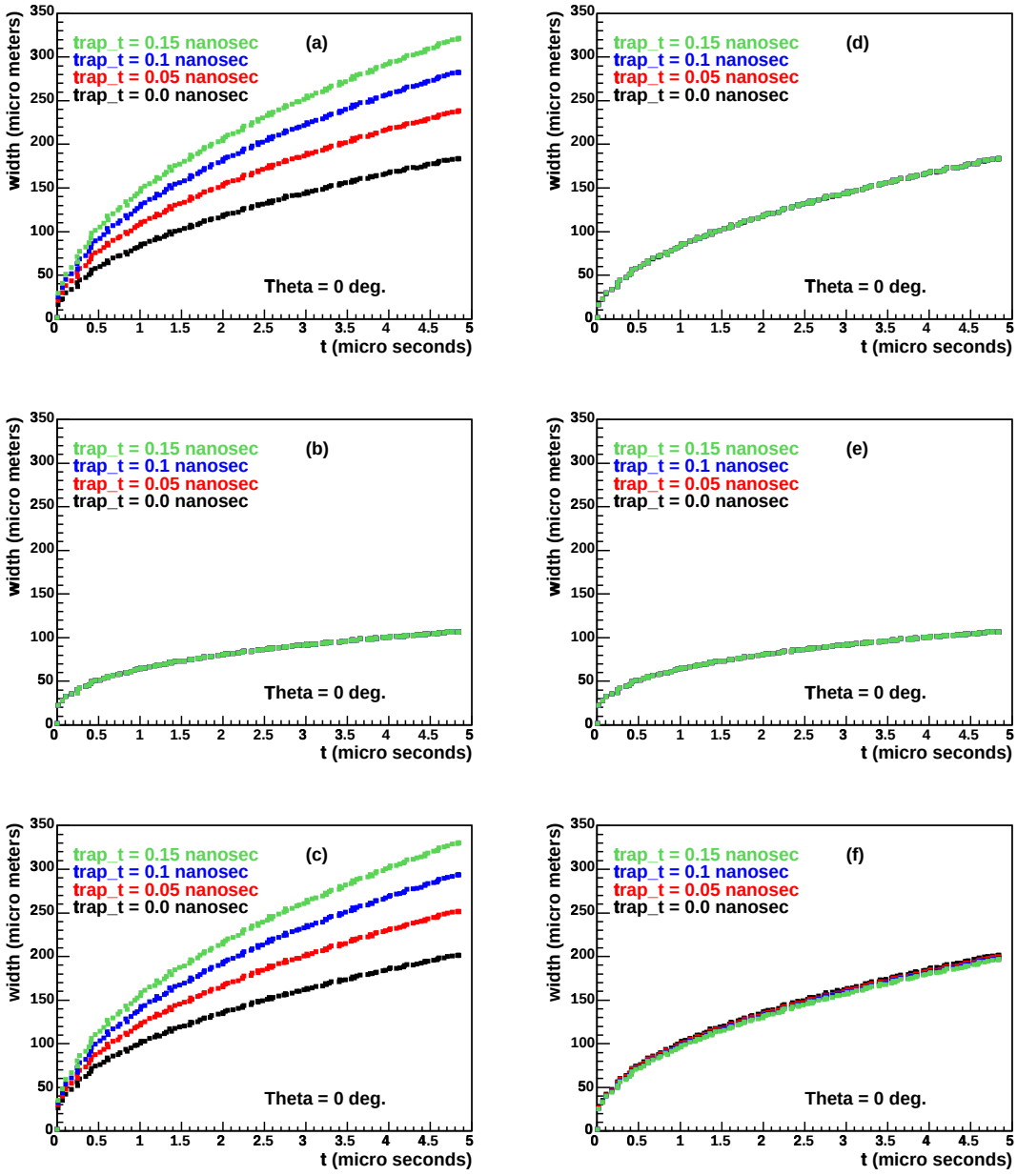

Figure 8.8: Dependence of signal width as a function of drift time on trapping time (MIPs) $\theta = 0^o$. (a) Expansion due to diffusion, (b) Expansion due to Coulomb repulsion and (c) Expansion due to both diffusion and Coulomb repulsion along the drift direction. (d),(e) and (f) show the same information as in (a),(b) and (c) respectively in the anode direction.

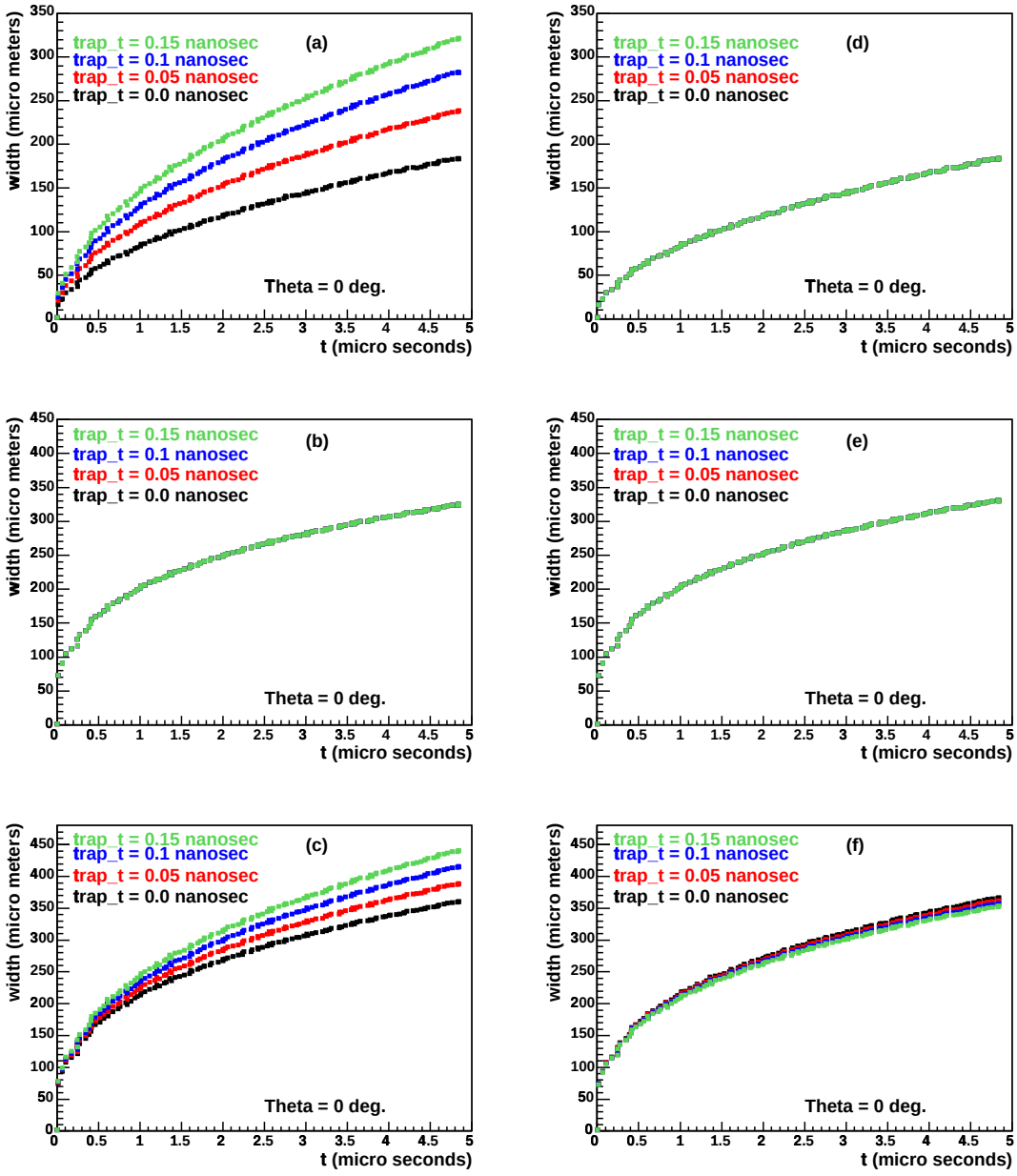

Figure 8.9: Dependence of signal width as a function of drift time on trapping time, large ionization (40× MIPs), $\theta = 0^o$. (a) Expansion due to diffusion, (b) Expansion due to Coulomb repulsion and (c) Expansion due to both diffusion and Coulomb repulsion along the drift direction. (d),(e) and (f) show the same information as in (a),(b) and (c) respectively in the anode direction.

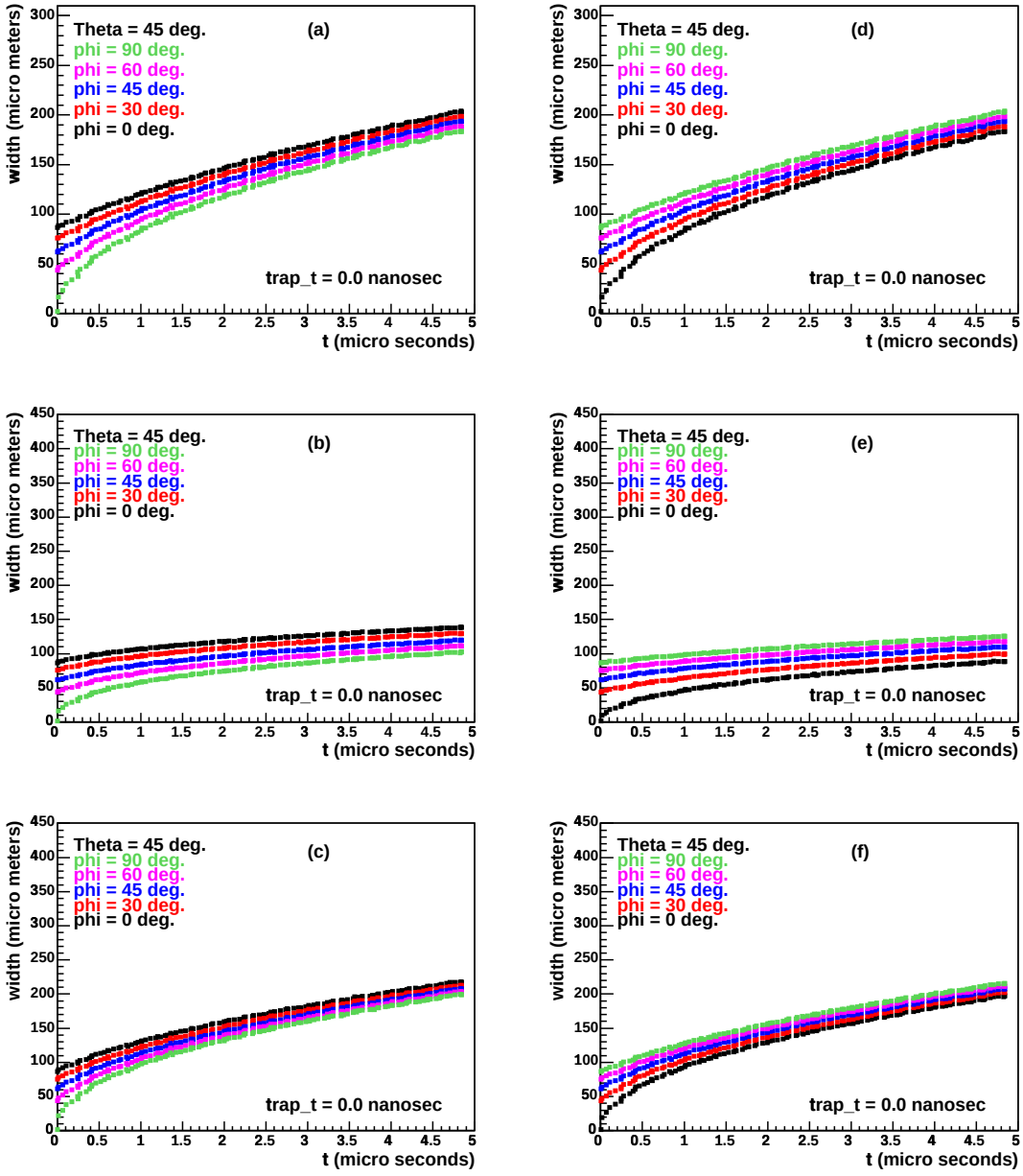

Figure 8.10: Dependence of signal width as a function of drift time on entrance angle(different ϕ's) (MIPs) $\theta = 45^o$, $t_{trap} = 0$. (a) Expansion due to diffusion, (b) Expansion due to Coulomb repulsion and (c) Expansion due to both diffusion and Coulomb repulsion along the drift direction. (d),(e) and (f) show the same information as in (a),(b) and (c) respectively in the anode direction.

cloud expands more and more. Diffusion however remains important until all the signal is collected. In Figures (8.8 a, 8.8 d) are shown the widths along drift and anode directions respectively considering only diffusion for a normal crossing of the SDD. Figures (8.8 b, 8.8 e) correspond to the case where only coulomb repulsion is considered. Figures (8.8 c, 8.8 f) include the effects of both diffusion and coulomb repulsion.

In the absence of trapping and detrapping effects, the charge carriers created by ionizing radiation move in the SDD with a constant drift velocity determined by the drift field, the temperature and the density of ionized impurities. The presence of trapping centers affects the drift velocity. Shown also are the effects of trapping and detrapping on the widths of the electron cloud produced by an MIP. One can see that trapping-detrapping process has a significant effect on the width in the drift direction while the width in the anode direction is affected very little. The overall effect is to make the electron cloud wider in the drift direction.

The plots in Figure (8.9) show the effect on the width of an electron cloud corresponding to large ionization ($40\times$ MIP $\approx 10^6$ electrons). In contrast to MIPs, the resulting huge coulomb repulsion significantly affects the widths in both drift and anode directions as shown in Figures (8.9 b, 8.9 e). As can be seen in Figures (8.9 a, 8.9 d), this seems to have no effect at all on the diffusion of the electrons.

Since particles cross the SDD in arbitrary directions, one has to consider the situation where the entrance angle is no longer 90^o relative to the plane of the SDD. Figure (8.10) shows what happens to the widths of an MIP for $\theta = 45^o$ and the trapping time $t_{trap} = 0$. Here θ is the angle between the normal to the SDD plane and the particle track and ϕ is the azimuthal angle of the track with respect to

the drift direction. The width in the drift direction in general decreases when the azimuthal angle ϕ gets larger.

On the other hand, the width in the anode direction gets larger when ϕ increases. This picture does not change for a trapping time of $0.1ns$ except that diffusion affects strongly the widths in the drift direction compared to the case where $t_{trap} = 0$ as shown in Figure (8.11).

In the case of high ionization charge, the effect of coulomb repulsion dominates over that of diffusion for $t_{trap} = 0$ as shown in Figure (8.12). For $t_{trap} = 0.1ns$ diffusion has a strong effect in the drift direction in addition to the effect of the coulmb repulsion. The widths exhibit the same behavior as those corressponding to MIPs except the coulomb effect is much bigger as shown in Figure (8.13).

The results of the simulation indicate the importance of electron trapping and detrapping effects and entrance angle of a track in addition to electron diffusion and mutual coulomb repulsion as the signal propagates from the point of generation to collection at the anodes. All these effects need to be taken into account in actual data analysis efforts.

With the TPC alone, star is limited to the study of hadron production with p_t above 150 MeV/c and had a modest efficiency and accuracy for the study of short lived particles decaying before they reach the inner layer of the TPC. Determination of the primary vertex to a very high accuracy is very important in track reconstruction. Being close to the beam line, the SVT plays an essential role in finding the interaction vertex. Figure (8.14 a) shows the very good correlation between the primary vertex as found by the SVT and that determined by the TPC.

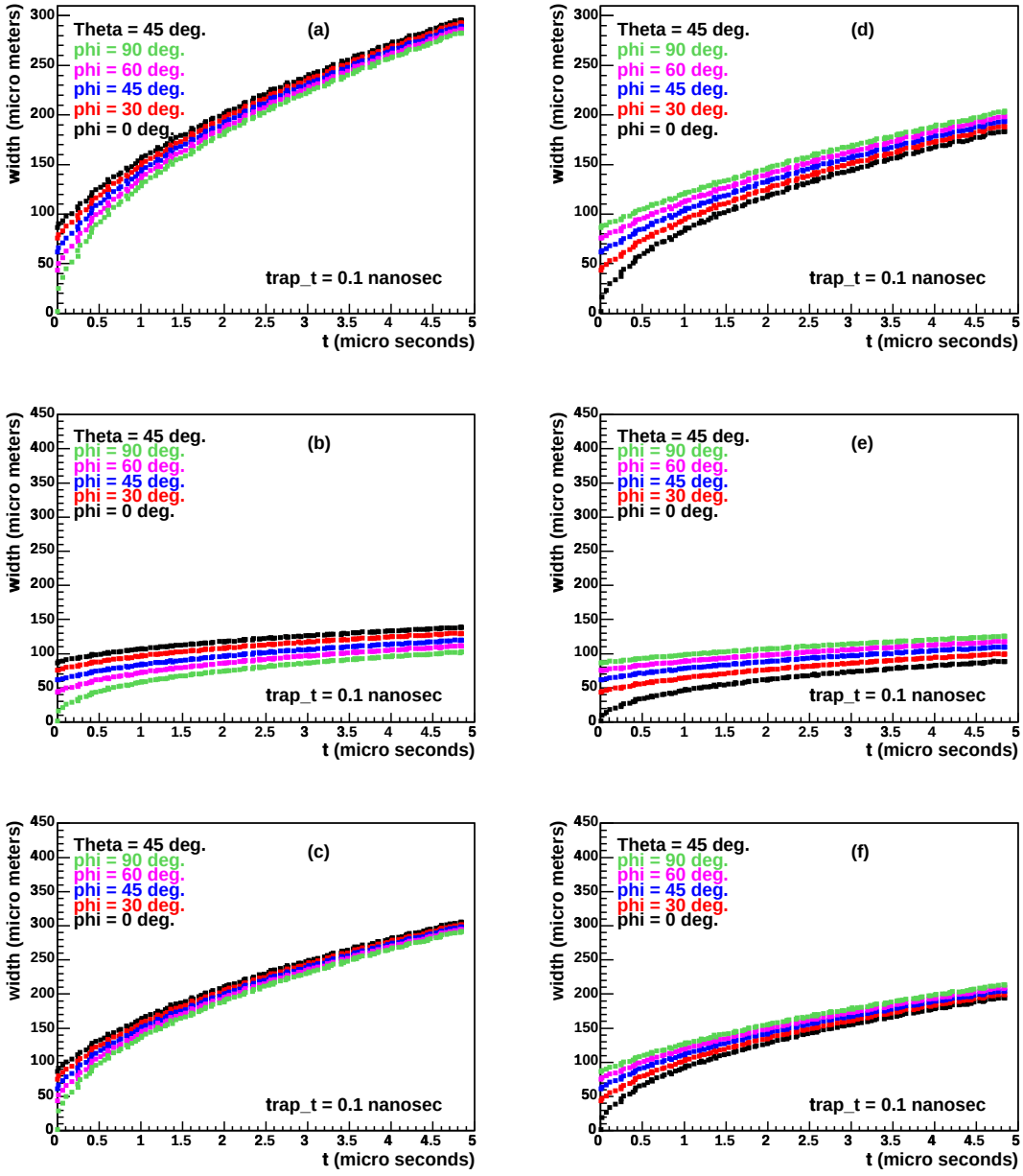

Figure 8.11: Dependence of signal width as a function of drift time on entrance angle(different ϕ's) (MIPs) $\theta = 45^o$, $t_{trap} = 0.1ns$. (a) Expansion due to diffusion, (b) Expansion due to Coulomb repulsion and (c) Expansion due to both diffusion and Coulomb repulsion along the drift direction. (d),(e) and (f) show the same information as in (a),(b) and (c) respectively in the anode direction.

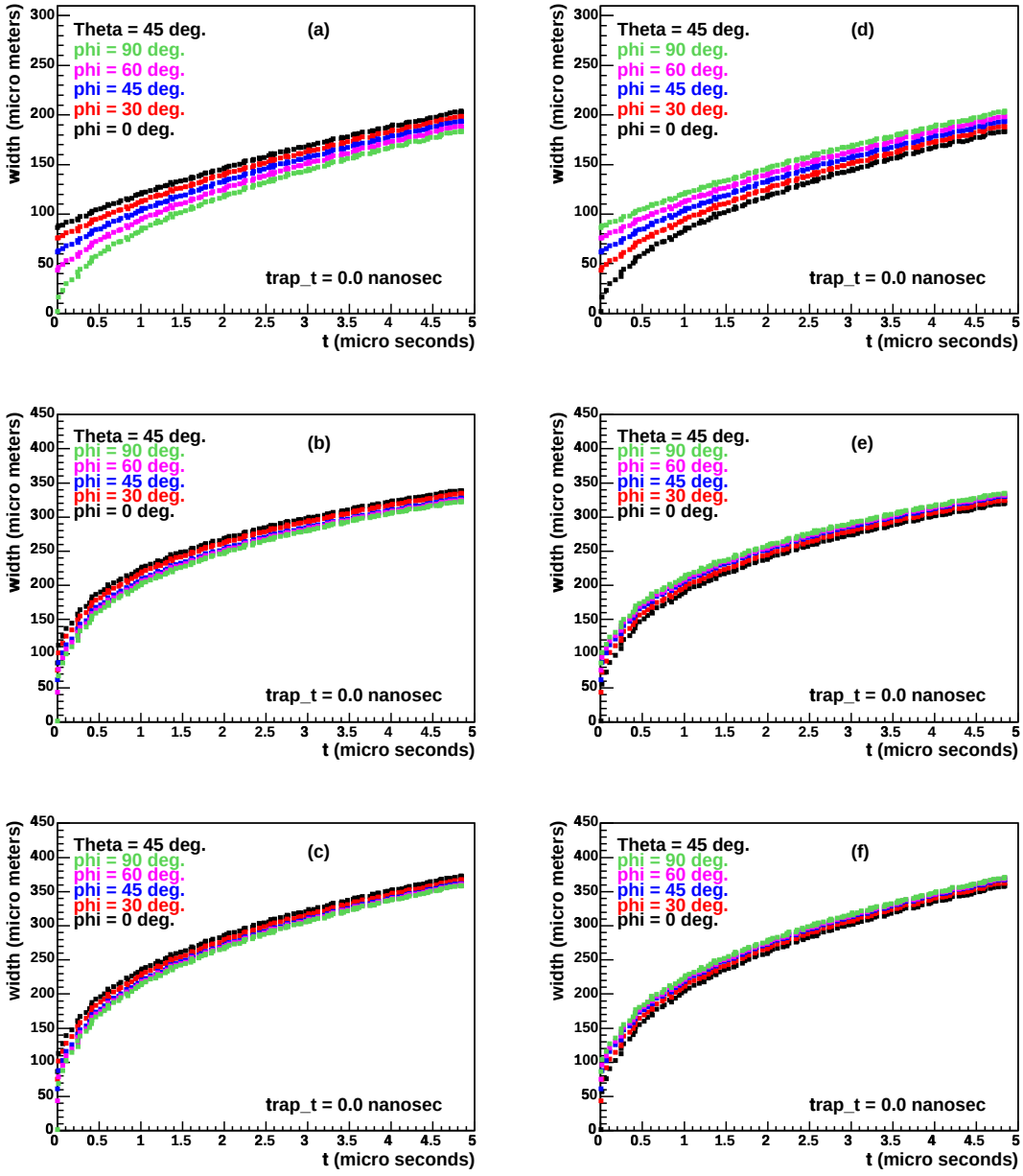

Figure 8.12: Dependence of signal width as a function of drift time on entrance angle(different ϕ's) large ionisation (40$\times$ MIPs), $\theta = 45^o$, $t_{trap} = 0$. (a) Expansion due to diffusion, (b) Expansion due to Coulomb repulsion and (c) Expansion due to both diffusion and Coulomb repulsion along the drift direction. (d),(e) and (f) show the same information as in (a),(b) and (c) respectively in the anode direction.

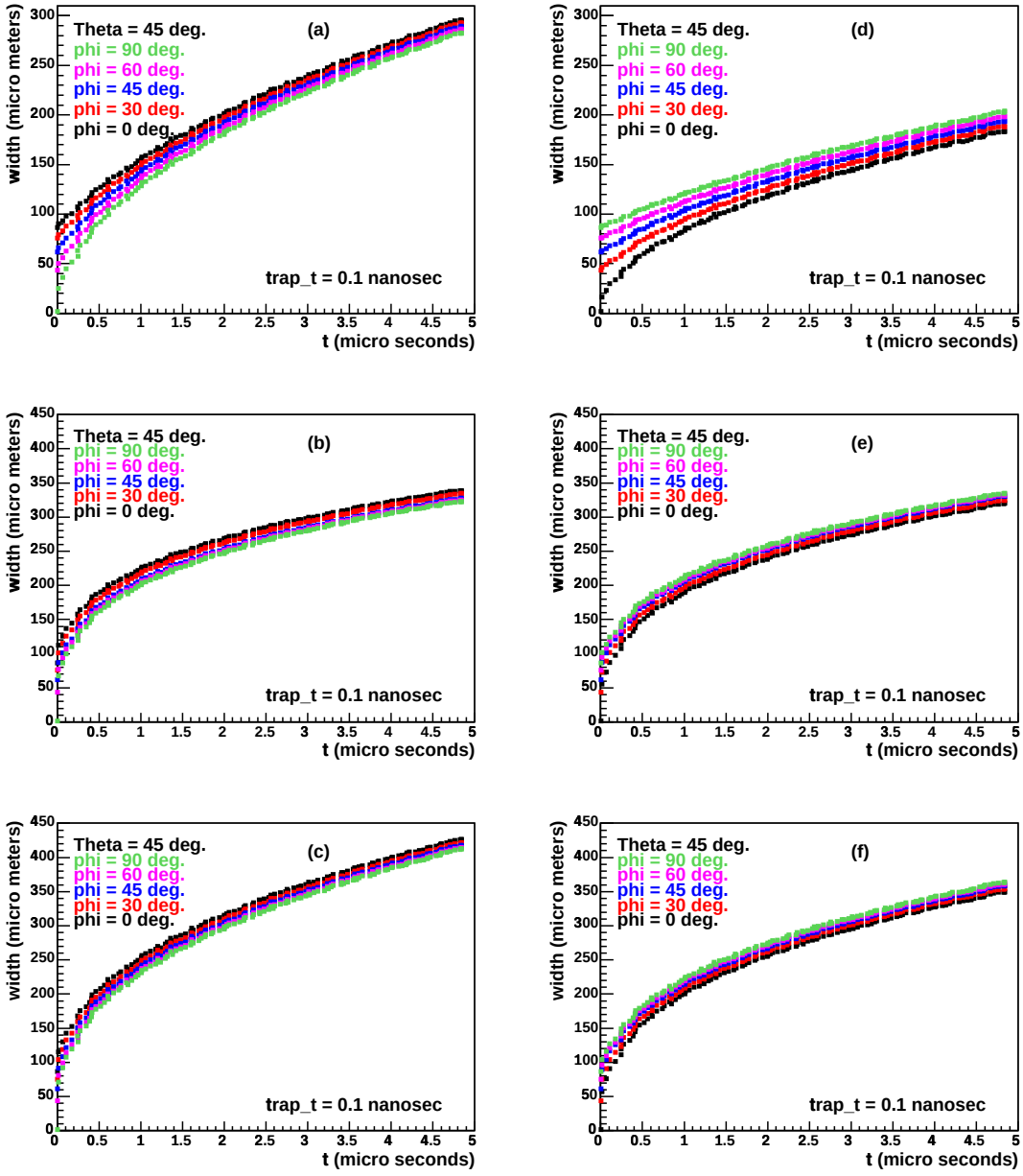

Figure 8.13: Dependence of signal width as a function of drift time on entrance angle(different ϕ's) large ionisation (40× MIPs), $\theta = 45^o$, $t_{trap} = 0.1ns$. (a) Expansion due to diffusion, (b) Expansion due to Coulomb repulsion and (c) Expansion due to both diffusion and Coulomb repulsion along the drift direction. (d),(e) and (f) show the same information as in (a),(b) and (c) respectively in the anode direction.

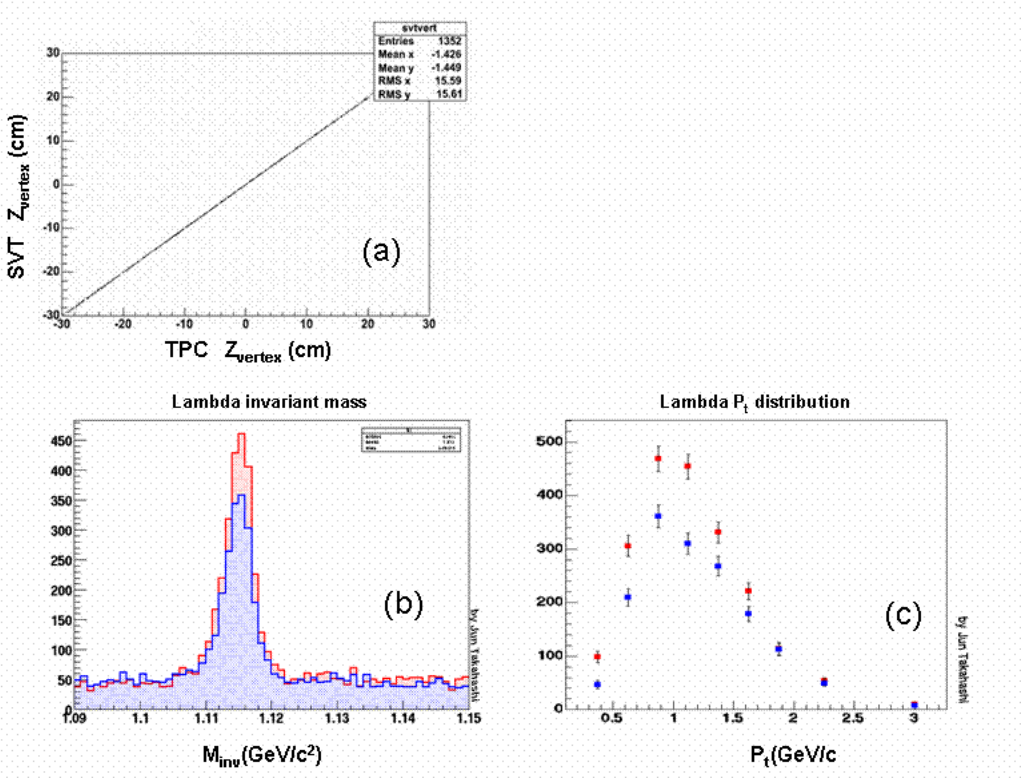

Figure 8.14: Correlation between SVT z-vertex and TPC z-vertex (a), invariant mass peak of λ particles (b), transverse momentum spectra of Λ particles (c).

Measurement of low p_t ($40 \leq p_t \leq 200$ Mev/c) spectra, detecting multi-strange baryons and improving the reconstruction efficiency for short lived particles such as $K^0_s, \phi, \Lambda, \bar{\Lambda}$ are also some of the design objectives for the SVT. The invariant mass distribution for λ particles is shown Figure (8.14 b). The histogram in red is obtained when the SVT is included together with the TPC for tracking of charged particles while the one in blue corresponds to the TPC only. The corresponding momentum spectra is shown in Figure (8.14 c). It is evident that there is an enhancement of low p_t particles and more Λs are found when SVT and TPC work together.

In general the SVT detector and its reconstruction software are performing well in the scientific endeavors of the STAR experiment at RHIC.

CHAPTER 9

EXPERIMENTAL RESULTS ON $K^0_S K^0_S$ CORRELATIONS

9.1 Introduction

Most of the particles produced in relativistic heavy ion collisions are pions and, as a result, pion interferometry has been a particularly useful tool in correlation studies. High statistics data from colliders like RHIC has also made it possible to study kaon correlations. A major problem in pion interferometry is resonance decays. Almost half of the pions produced in heavy ion collisions come from resonances. Kaon HBT on the other hand suffers less from resonance contributions and could provide a cleaner signal for correlation studies than pions [90, 91]. Higher multi-particle correlation effects that might play a role for pions, should be of minor importance for kaons since the kaon density is considerably smaller than the pion density at RHIC ($\sqrt{s}_{NN} = 130$ GeV) . The pion multiplicity has increased by approximately 70% from SPS ($\sqrt{s}_{NN} = 17.4$ GeV) [92] to RHIC whereas the interferometry radii are almost the same [93, 94]. The strangeness distillation mechanism [95] might further increase the time delay signature. Kaon evaporation could lead to strong temporal emission asymmetries between kaons and antikaons [96], thus probing the latent heat of the phase transition. For the neutral kaons, the absence of Coulomb interaction is an advantage over their charged counterparts. Charged pions and kaons can be identified

via the energy loss method only up to a momentum of about 700 MeV which prohibits correlation studies with these particles in the high momentum region. The neutral kaons, with a mean transverse pair momentum of around 1 GeV, push the method of intensity interferometry into the high momentum region.

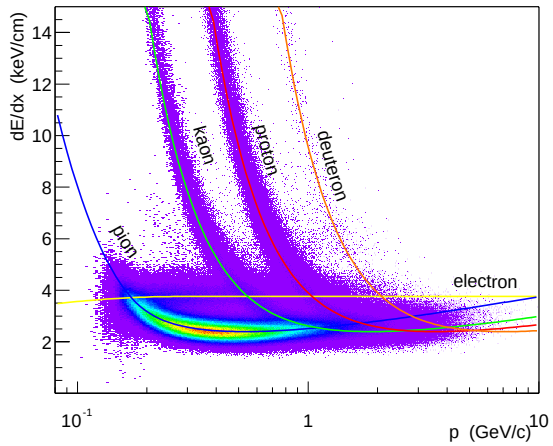

Figure 9.1: Energy loss $\frac{dE}{dx}$ of charged particles as a function of their momentum p.

Neutral particles decay into oppositely charged particles which can be identified through a measurement of the correlation between their ionization energy loss ($\frac{dE}{dx}$) in the gas of the TPC and their momentum. Figure (9.1) shows the energy loss bands for various particles as a function of momentum. The ionization energy loss, also called the specific ionization, is given by the expression

$$-\frac{dE}{dx} = 4\pi N_0 r_e^2 m^e c^2 \frac{Z}{A}\rho\frac{1}{\beta^2}z^2\left[ln(\frac{2m_e c^2}{I}\beta^2\gamma^2) - \beta 62 - \frac{\delta}{2}\right] \tag{9.1}$$

where N_0 is the Avogadro number, A and Z are the mass number and atomic number respectively, m_e is the mass of the electron, $r_e = \frac{e^2}{m_e}$ is the classical electron radius,

and ρ is the medium density. I is the ionization potential of the medium, z is the charge of the particle traversing the medium, and δ parameterizes a "density effect" of the the medium which describes the saturation energy loss at highly relativistic velocities. Also, $\beta = \frac{v}{c}$ and $\gamma = \frac{1}{\sqrt{1-\beta^2}}$. While the specific ionization does not depend on the mass of the particle traversing the medium, it can be shown that $\beta\gamma = \frac{p}{mc}$ where p and m are the momentum and mass of the particle. This means that specific ionization energy losses of different mass particles are separated from each other when examined at the same momentum.

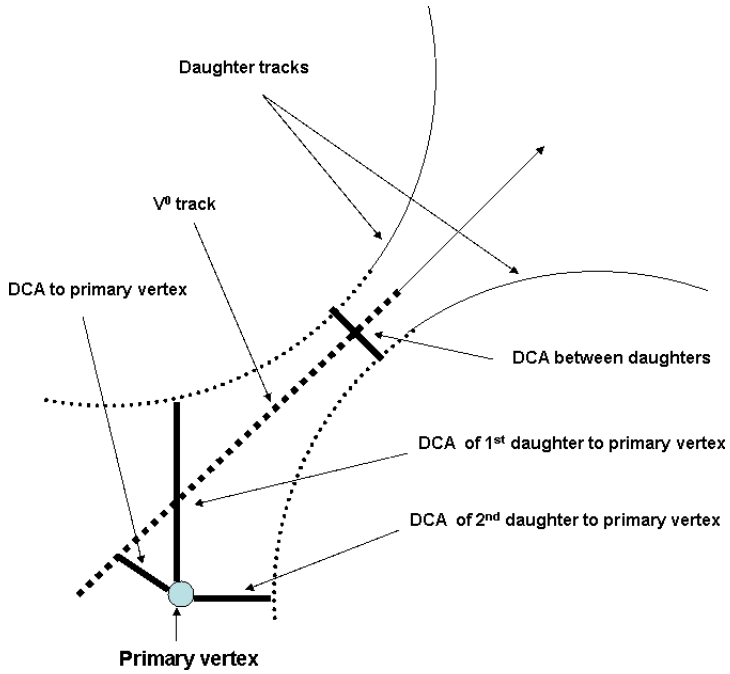

Figure 9.2: V^0 decay topology for a neutral particle.

Figure (9.2) shows a schematic diagram of the decay of a neutral particle into positive and negative daughters which bend away from each other due to the magnetic

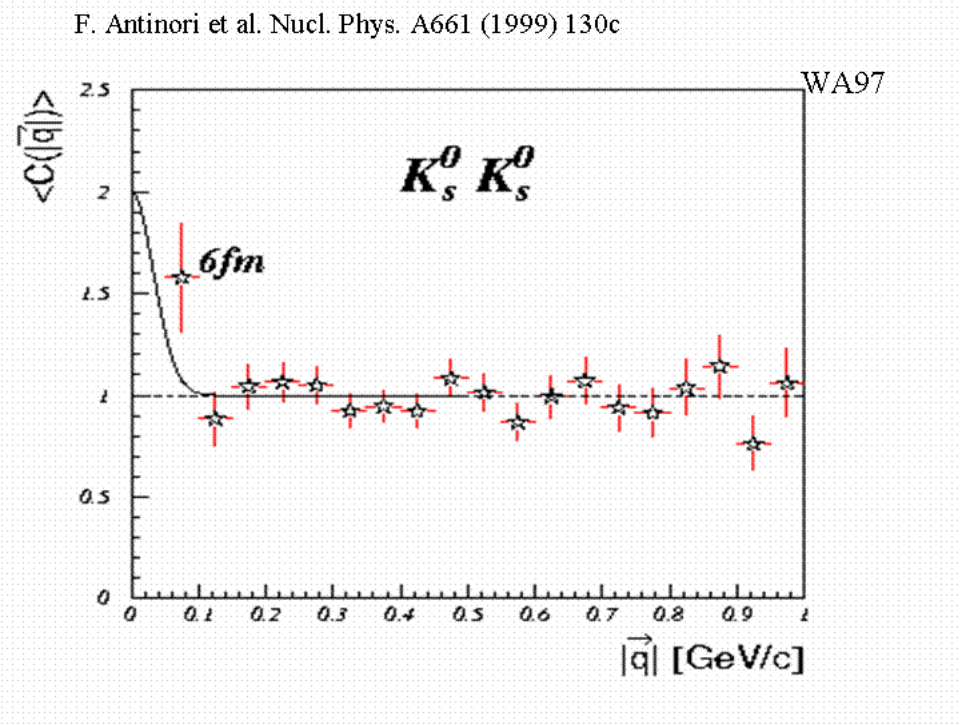

Figure 9.3: $K_s^0 K_s^0$ correlation from WA97 experiment.

field in the TPC. Once the secondary particles are reconstructed, the neutral particles are identified through their decay topology by looking for pairs of oppositely charged tracks that extrapolate to a common point which is as far away as possible from the main interaction vertex. Momentum conservation allows to calculate the momentum of the neutral particle from the reconstructed momenta of the daughter particles.

Previous heavy ion experiments were not able to measure neutral kaon correlations mainly due to lack of sufficient statistics. Figure (9.3) shows the only $K_s^0 K_s^0$ correlation from the WA97 experiment at CERN. The line is just a simulated correlation function to show what one might get for a 6 fm Gaussian source. It can be clearly

seen that a significant enhancement of low q pairs is absent. This would make STAR the first heavy ion experiment to have made a significant neutral kaon measurement.

9.2 Data Selection

For this analysis, central events were used with an event vertex within ± 25 cm of the TPC center. The K_s^0 has a decay length of 2.7 cm and decays via the weak interaction into $\pi+$ and $\pi-$. The kinematic and topological cuts are summarized in Table (9.1). The possibility of a single neutral kaon being correlated with itself was eliminated by requiring that a pair of K_s^0 have unique daughters.

parameter	Range
Invariant mass	$0.48 - 0.51$ GeV/c^2
Transverse momentum (p_t)	$0.1 - 3.5$ GeV/c
Armentros p_t	$0.1 - 0.25$
Armentros α	$-1.0 - 1.0$
Rapidity	$-1.5 - 1.5$
$\frac{dE}{dx}$	< 3 Sigmas
Number of hits	> 15
DCA of +ve daughter	> 1.3 cm
DCA of -ve daughter	> 1.3 cm

Table 9.1: Kinematic and topological cuts used in this analysis. DCA to the primary vertex and decay length of the K_s^0 are not included since they are used in the systematic studies of correlation functions

In experimental intensity interferometry, a correlation function is constructed from the number of counts n_1 and n_2 measured at two detectors if one of them was absent and the number n_{12} of counts in which particles are observed at both detectors simultaneously. The correlation function is proportional to the intensity (i.e., the complex

square of the amplitude) of the particles at the two detectors. The correlation function is defined as

$$C_2(q) = \frac{A(q)}{B(q)} \tag{9.2}$$

where A(q) represents the distribution of the four momentum difference $q = p_1 - p_2$ for a pair of particles coming from the same event. B(q) is the reference distribution constructed by mixing particles from different events. The mixed pairs are also required to satisfy the same pair-wise cuts applied to pairs from the same event.

Figure (9.4 a) shows the K_s^0 invariant mass distribution obtained with the set of cuts in Table (9.1), distance of closest approach(DCA) < 0.6 cm and decay length (DCL)> 4 cm. As it is very important to have a pure sample of the data available for correlation studies, one applies all possible kinematical and detector related cuts to achieve the maximum desired signal at the single particle level. One may apply very stringent cuts to make the data sample as pure as possible. While this procedure improves the signal over the background, it would not be very useful in situations with limited statistics. However, even after all possible cuts are applied, there still remain some particles that make it through the cleaning process making it necessary to correct for the contribution of the residual background. This calls for a knowledge of the best signal to background ratio with in the selected invariant mass window (ΔM_{inv}). While it is quite clear where to set their values for most of the cut parameters, sometimes it becomes neccesary in the case of insufficient statistics to use a wider set of windows for those cut parameters for which it is not clear where to set their values. This procedure improves statistics at the expense of adding more background to the signal. This is not a problem with since one can always make corrections if the signal to background is correctly determined. For the neutral kaons, the decay length(DCL) and distance

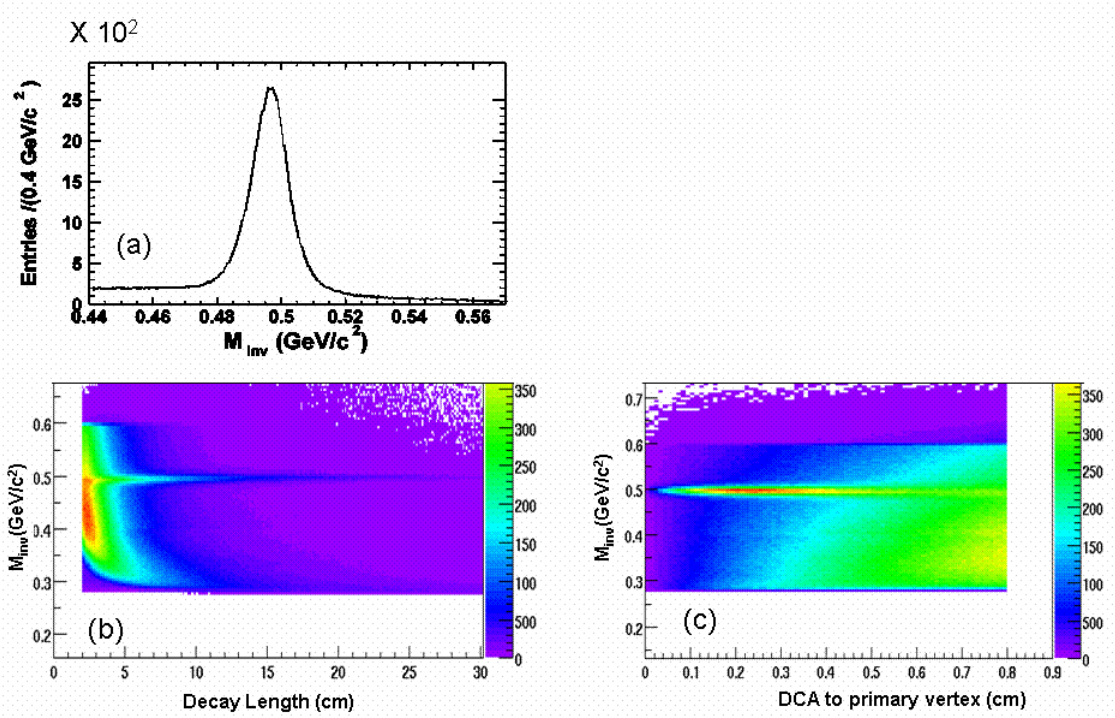

Figure 9.4: The K_s^0 invariant mass distribution (a), distribution of the K_s^0 invariant mass versus decay length(DCL) (b), distribution of the K_s^0 invariant mass versus DCA to primary vertex (DCA).

of closest approach(DCA) to the interaction vertex were two of the cut parameters for which it was difficult to set their values. Figure (9.4 b) shows a distribution of M_{inv} versus DCL. One can clearly see the band around the mass of the kaon. Evidently, a decay length of less than 0.4 cm should be good enough for our purpose. Similarly, a DCA value greater than 4 cm would work very well as can be seen from a distribution of M_{inv} versus DCA displayed in Figure (9.4 c). But these cuts would somehow limit the statistics that we can use. These two parameters are considered as the main sources of systematic errors.

9.3 Signal to Background Study

By looking at the invariant mass distribution of the K_s^0 in several transverse momentum bins, it was found that the signal to noise is momentum dependent. Once the signal to noise as a function of p_t is computed, the next thing to calculate is the pair-purity which is the product of the signal to noise values for each pair of particles that make it into the correlation function. The variation with p_t of the signal to noise means that the pair purity is a function of the invariant four momentum difference, Q_{inv}.

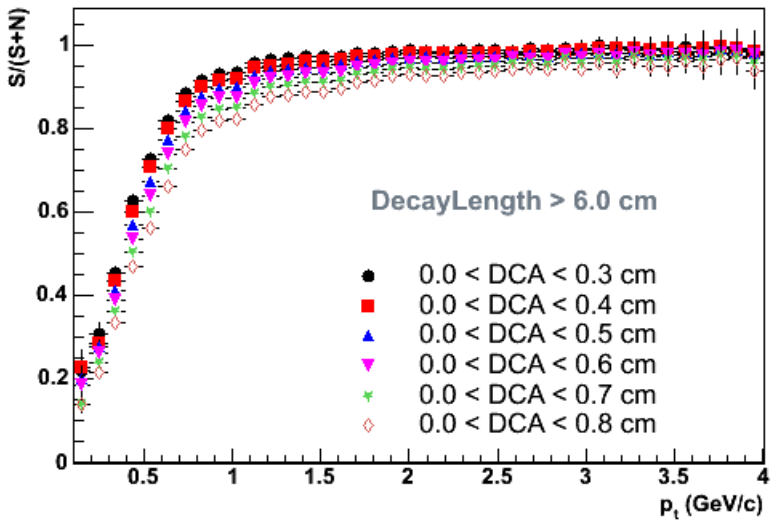

Figure 9.5: The signal to noise of K_s^0 as a function of transverse momentum.

Figure (9.5) displays the signal to noise as a function of p_t for the various DCA and DCL combinations. It can be seen that for a given DCA cut, the signal increases as the decay length gets bigger. The largest change in signal to noise occurs below about

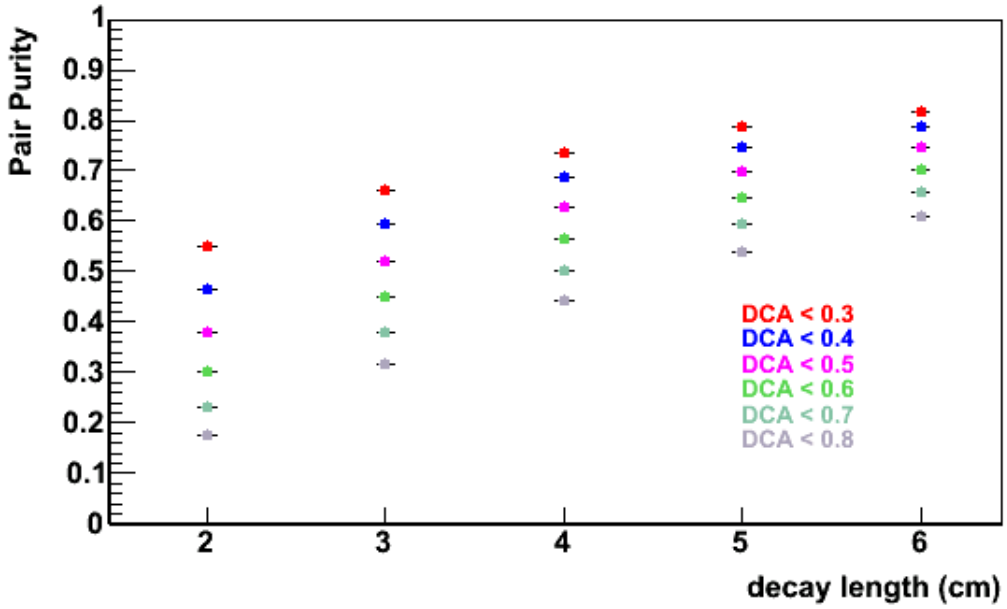

Figure 9.6: The pair purity of the $K^0_s K^0_s$ pairs as a function of the invariant four momentum difference based on the signal to noise in Figure(9.5).

1 GeV in transverse momentum. The plots are almost flat above $p_t = 1$ GeV. The corresponding pair-purity correlation function is constructed by taking the product of the individual $\frac{S}{S+N}$ values for the particles that make up a given pair. The pair-purity correlation functions were found to be independent of Q_{inv} for all combinations of DCL and DCA values with all other cut parameters fixed. Figure (9.6) shows the average pair-purity as a function of decay length for the various DCA values. It is evident that the pair-purity increases as the decay length gets larger for each DCA cut and the best pair purity corresponds to a DCL cut larger than 6 cm and DCA less than 0.3 cm.

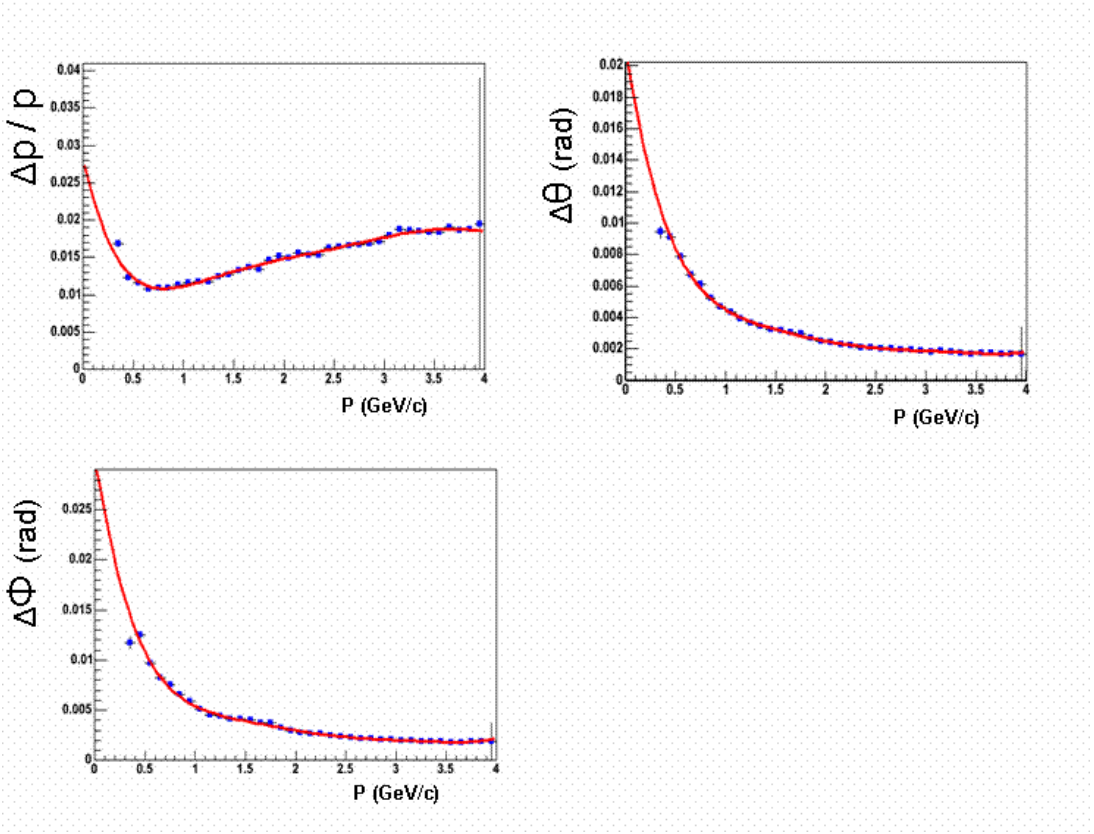

Figure 9.7: Momentum resolution as a function of the K_s^0 transverse momentum p_t.

9.4 Momentum Resolution Study

A charged particle traversing a medium is deflected by many small-angle scatters. The net effect of all these scatters causes the particle to stray from its original trajectory, thus reducing the tracking resolution of any experimental device. The effect is significant for low momentum tracks since they spend more time around a scattering center. The implication is that the measured momentum of a particle is usually different from the actual value. Since the momenta of neutral particles are reconstructed

from their charged daughters, they are also affected indirectly by momentum resolution. To investigate the effect of momentum resolution on the correlation functions simulated K^0_s tracks with known momenta $\vec{p}_{in}$ are embedded into the data from a real event. The reconstructed momenta of the embedded tracks $\vec{p}_{rec}$ are then compared with the input $\vec{p}_{in}$. The distribution of $\frac{\vec{p}_{rec}-\vec{p}_{in}}{p}$ are then fitted to a Gaussian to get the rms widths which are used to characterize the momentum resolution of the detector. Figure (9.7) shows a plot of $\frac{dp}{p}$ versus p. The bins in p are 100 MeV wide in order to have enough statistics. The resolution in p lies between 1% and 2%. The resolutions are less than 0.015 in ϕ, less than 0.01 in θ.

9.5 Results

The $K^0_s K^0_s$ correlation function is displayed in Figure(9.8). The line is a fit to the corrected correlation function using the expression

$$C(q) = N \cdot (1 + \lambda \cdot e^{-R^2_{inv} q^2_{inv}}) \tag{9.3}$$

where q_{inv} is the invariant four momentum and R_{inv} is the corresponding size parameter. It can be seen that the effect of the momentum resolution is very small compared to the purity of the data sample. The width of the correlation function does not change very much while its height which corresponds to λ is pushed up. Plotting the fit parameters as a function of the pair purity gives an idea of the systematic errors involved. The plots in Figures (9.9) and (9.10) show the fit parameters for K^0_s as a function of the average pair purity. Decay Length increases to the right from 2 cm (corresponding to the lowest pair purity) to 6 cm (corresponding to the largest pair purity) for each DCA cut. The values of Rinv and Lambda are extracted by fitting the corresponding correlation functions to a Gaussian. These values seem to saturate

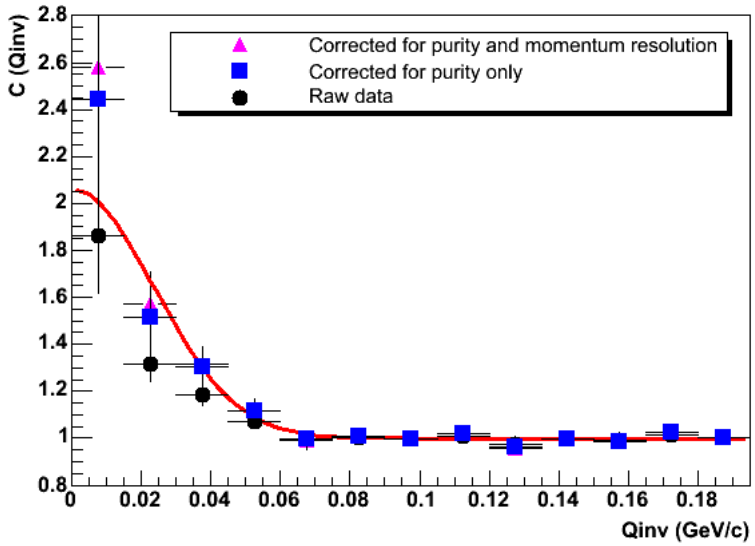

Figure 9.8: The $K^0_s K^0_s$ correlation function.

for decay lengths greater than 4 cm. The points in red are obtained when the fit is done including the first bin in the correlation function.

1^{st} bin	λ	R_{inv}
included	$1.05 \pm 0.32\ (stat.) \pm 0.19\ (sys.)$	$6.04 \pm 0.85\ (stat.) \pm 0.89\ (sys.)$
excluded	$0.92 \pm 0.30\ (stat.) \pm 0.18\ (sys.)$	$5.74 \pm 0.83\ (stat.) \pm 0.51\ (sys.)$

Table 9.2: The values of R_{inv} and λ obtained by including and excluding the 1^{st} point of the correlation function while fitting. The two results are similar within errors.

The blue points are what one gets by excluding the first bin from the fit. Table (9.2) shows the final values of R_{inv} and λ. It seems that the exclusion of the first bin does not affect the fit parameters that much. One expects $\lambda = 1$ for a system with little contamination from decaying resonances and misidentified particles. In

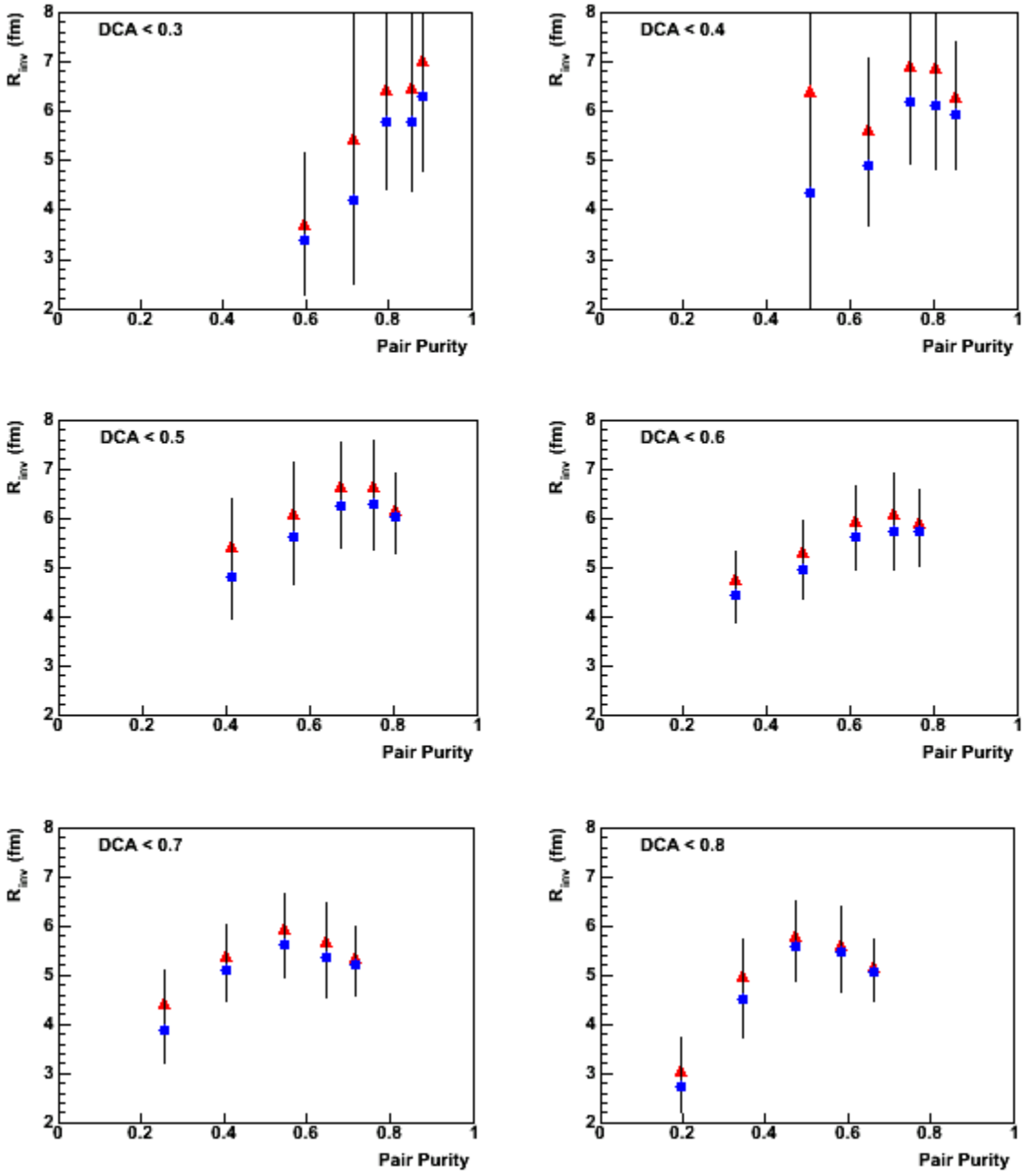

Figure 9.9: The radius parameter R_{inv} versus the pair purity of the $K_s^0 K_s^0$ pairs .

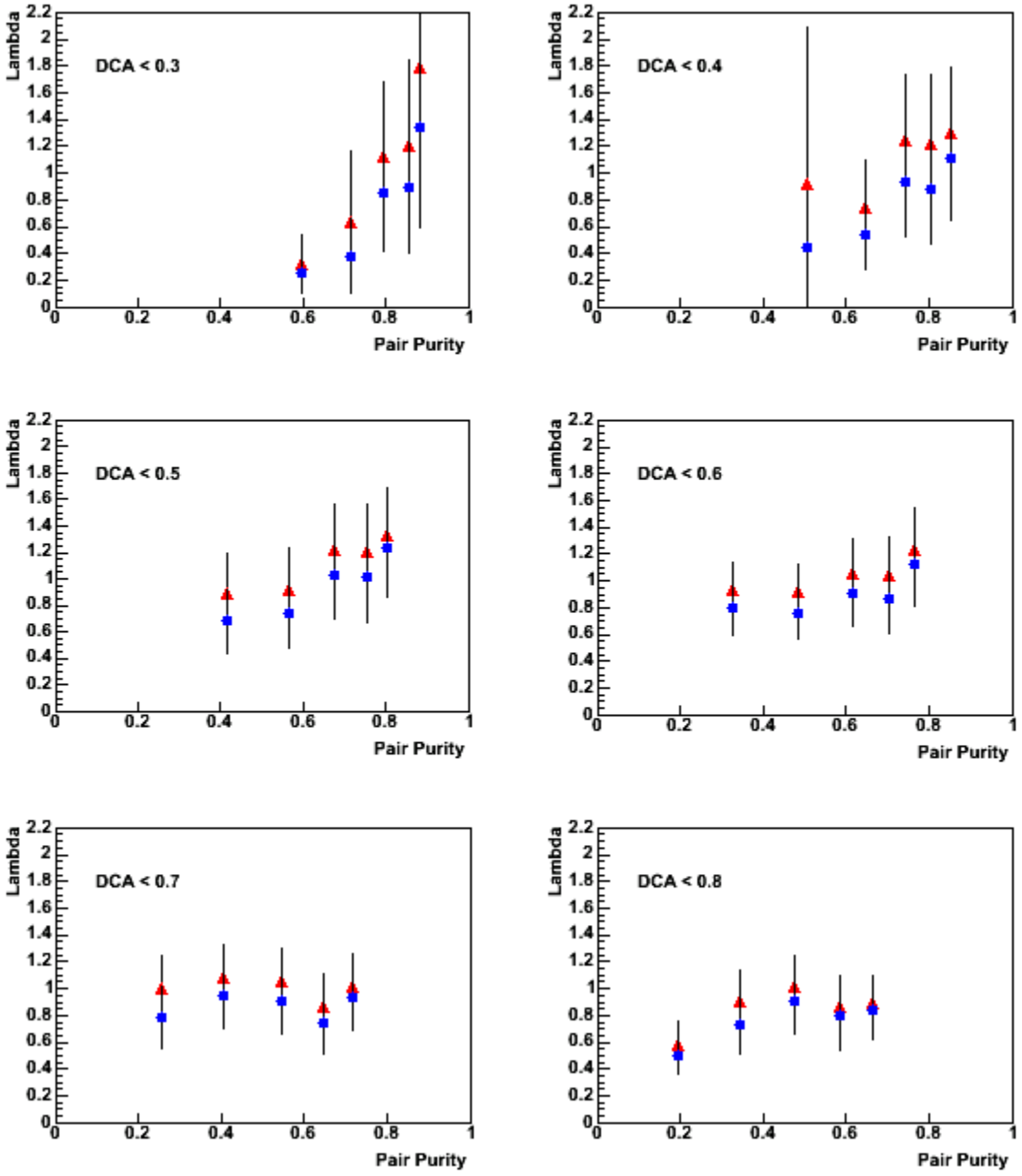

Figure 9.10: The chaoticity parameter λ versus the pair purity of the $K_s^0 K_s^0$ pairs.

comparison, the experiments OPAL [99] and ALEPH [100] have measured correlations of neutral kaons from hadronic decays of Z^0 in e^+e^- collisions at LEP. They report the values $\lambda = 1.14 \pm 0.23, R_{inv} = 0.76 \pm 0.1$ and $\lambda = 0.96 \pm 0.21, R_{inv} = 0.65 \pm 0.07$ respectively. As expected, the size measured in Au-Au collisions is considerably larger than those from the LEP experiments which involve collisions that indeed produce smaller sources.

9.6 Final State Interactions

The strong interaction has an important effect on the nature of the interference correlations in the detection of pairs of neutral kaons. Using a static spherical Gaussian source as a model [101] in the pair rest frame, a simulation of theoretical correlation function including final state interaction (FSI) weights was carried out. The momentum spectra from the data was used to calculate the relative momenta between pairs of particles. Several correlation functions were calculated by varying the radius (R_{in}) of the kaon emitting source. Figure (9.11a) shows what one should get

$Reference$	$g_{f^0 \to K\bar{K}}$	$g_{f_0 \to \pi\pi}$	$g_{a^0 \to K\bar{K}}$	$g_{a_0 \to \pi\eta}$
[102]	.792	.199	.333	.222
[103]	.094	.110	.333	.222

Table 9.3: Coupling constants determined by scattering phase shift analysis taken from references [102, 103]

for a pure quantum statistics case. The correlation functions with only the strong interaction are shown in Figures (9.11 b, 9.11 c). The lower two plots on the left correspond to values of the coupling strengths as determined by phase shift analysis

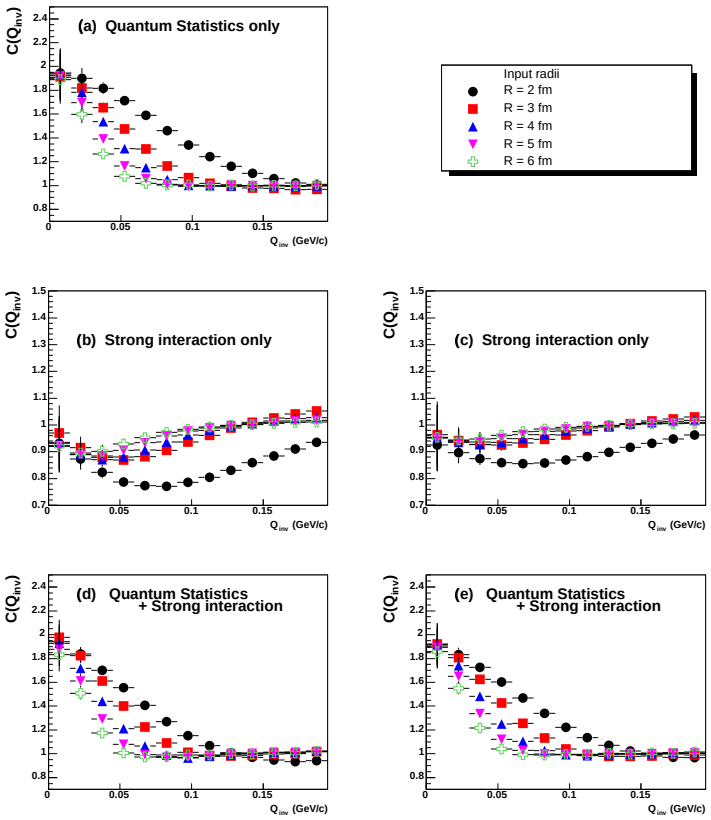

Figure 9.11: Theoretical correlation functions for a static Gaussian source.

of scattering data by Martin *et al.*[102] and those on the right correspond to values from analysis carried out by Morgan and collaborators [103]. The actual values are given in Table (9.3). Our calculations showed that the effect of the strong interaction for the $K^0\bar{K}^0$ pairs seems repulsive. The negative sign is indeed unexpected for the resonances that decay to a particle-antiparticle pair. The FSI effect may be dominated by the interference term between the plane and spherical waves of the wave function

$$\Psi(Q,r) = e^{-i\frac{\vec{Q}\cdot\vec{r}}{2}} + f(Q)\ \frac{e^{i\frac{Qr}{2}}}{r} \tag{9.4}$$

where f(Q) is the s-wave $K^0\bar{K}^0$ scattering amplitude. Neglecting the real part of the resonance amplitude for simplicity , the imaginary part of the amplitude can be written as $f(Q) \approx i\frac{2b_0}{1+b_0 k}$, where $b_0 \approx 1$ fm is the scattering length. By considering the first two terms (higher order terms in Q are ignored for $Q \to 0$) in the expansions of the exponentials and averaging over the angle between the vectors $\vec{Q}$ and $\vec{r}$ one gets

$$C(Q) = \left\langle \left(1 - \frac{b_0\ Q}{(2\ +\ b_0\ Q)}\right)^2 \right\rangle + \left\langle \left(\frac{2\ b_0}{r(2\ +\ b_0)}\right)^2 \right\rangle + ... \tag{9.5}$$

One can show that it is possible to get $C(Q) < 1$ for $\langle (b_0/r)^2 \rangle < b_0 Q$, and this is the case for heavy ion collisions where $\langle r \rangle \approx 10$ fm ($>> b_0 \approx 1$ fm). We would then have a dip in the CF at the intermediate values of Q since $C(Q) \to 1$ as $Q \to \infty$.

The expected Breit-Wigner behavior comes in only at small distances when the square of the spherical wave $\approx |b_0|^2/r^2$ dominates. Of course, there can be additional (compared to FSI) resonance contribution due to direct f^0, a^0 production which are not related to FSI. This contribution is believed to be of the usual Breit-Wigner form and is assumed to be small and so it is not added to the FSI calculation. Figure (9.12) shows the correlation between the extracted radius (R_{fit}) and the input radius (R_{in}) by fitting the correlation functions in Figure (9.11) to a Gaussian. The effect of the strong interaction is to make the source sizes bigger than would be obtained by considering Bose-Einstein correlations only. Table (9.4) summarizes the values of R_{inv} obtained after a simple subtraction of the strong interaction effect for the two sets of parameters in the references indicated. There exist various parameterizations of experimental data that give differing values of coupling strengths and widths for

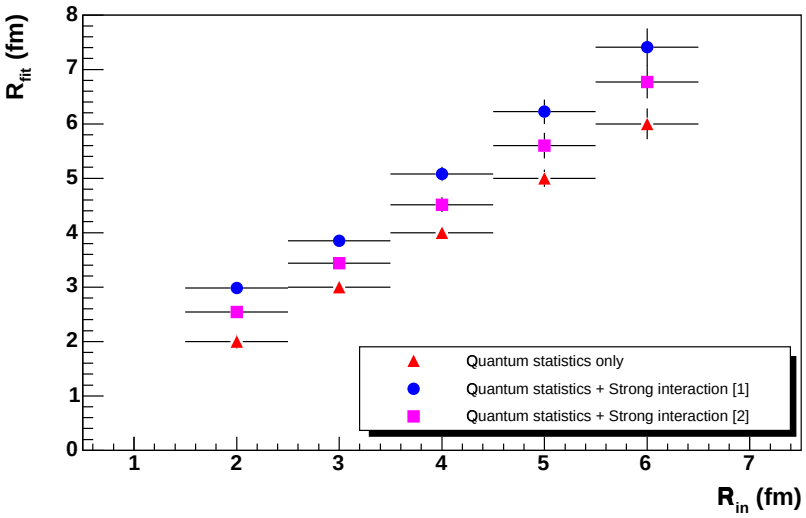

Figure 9.12: The effect of the strong interaction is to make the source sizes bigger than would be obtained by considering Bose-Einstein correlations only. ([1]) coupling constants and widths from ref. [102], ([2]) coupling constants and widths from ref. [103].

the f^0 and a^0 resonances [105]. As a result, it is quite difficult to determine systematic uncertainties at this stage.

9.7 M_t dependence of R_{inv}

As a result of collective expansion HBT radii show a dependence on the transverse pair momentum[68, 106, 107]. Such dependence could also come from temperature gradients in the source and also from contributions from resonance decays. Models with a hydrodynamic expansion predict that the radius parameters from a three dimensional analysis of HBT scale as $\frac{1}{M_t}$ where $M_t = \sqrt{p_t^2 + m^2}$. The NA44 experiment at CERN has reported a common M_t scaling for pions and kaons [108, 109]. Even

1^{st} bin	included	excluded
$Ref.$	R_{inv}	R_{inv}
[102]	5.02 ± 0.85 $(stat.) \pm 0.89$ $(sys.)$ fm	4.85 ± 0.83 $(stat.) \pm 0.51$ $(sys.)$ fm
[103]	5.60 ± 0.85 $(stat.) \pm 0.89$ $(sys.)$ fm	5.18 ± 0.83 $(stat.) \pm 0.51$ $(sys.)$ fm

Table 9.4: R_{inv} after correcting for the strong interaction using a linear fit to the correlation between the input and output radii obtained with Gaussian fits to the theoretical correlation functions. Systematic errors are not included for the effect of the strong interaction

though one dimensional, it is instructive to see if the one dimensional HBT radii measured in STAR also follow M_t scaling at least qualitatively.

Figure(9.13) shows the one dimensional M_t dependence of R_{inv} for $\pi\pi, K^0_s K^0_s$ correlations. The triangles are for the charged pions. The others are the neutral kaon points. The star is for the case of quantum statistical correlations only. The value of R_{inv} for K^0_s is big given the large mean transverse mass ($M_t \approx 980$ MeV/c^2) of the pair compared to what one would expect for the charged pions at the same M_t. However, after taking into account the effect of the strong interaction between K^0 and $\bar{K^0}$ the neutral kaons seems to follow the m_T systematics of the pions. The square and solid circle correspond to the two sets of coupling strength and width parameters from references [103] and [102] respectively.

9.8 How important is the f^0 resonance to K^0_s K^0_s HBT ?

Contributions from resonance decays are small and effects of coulomb interaction are absent. One question that arose recently is whether the decay of the f^0 has any effect on K^0_s K^0_s HBT. According to the Review of Particle Physics [104], the mass of the $f^0(980)$ scalar resonance is $980 \pm 10 MeV$ which is very close to the $K\bar{K}$

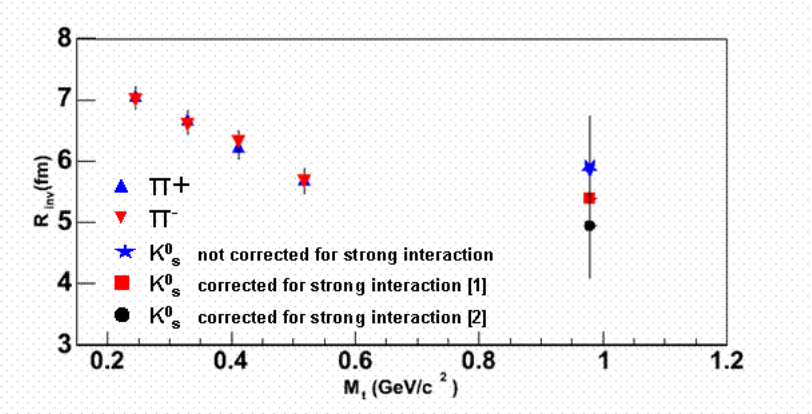

Figure 9.13: The invariant radius R_{inv} as a function of M_t. Statistical and systematic errors are shown for the pions. The neutral kaon K_s^0 points have only statistical errors. ([1]) coupling constants and widths from ref. [103], ([2]) coupling constants and widths from ref. [102].

threshold and the width ranges from $40 - 100 MeV$. It is believed that the $f^0(980)$ is most probably a Briet-Wigner-like resonance with a narrow width $\Gamma \sim 52$ MeV. The dominant decay mode is $\pi\pi$. This section discusses a Mont Carlo study to determine how the decay of the f^0 into kaons affects the correlation signal for the K^0. A worst case scenario, in which the f^0 decays only to kaons, is considered as the branching ratio for the $K\bar{K}$ is as yet unknown. If one assumes that the mass distribution of the f^0 has a Briet-Wigner or Lorentzian form

$$f(M) = \frac{1}{2\pi} \frac{\Gamma}{(M - M_0)^2 + \frac{\Gamma^2}{4}} \tag{9.6}$$

where M_0 and Γ are the mass and width of the f^0 respectively. Figure (9.14) shows the mass distribution based on Eq. (9.6). One can see that those f^0s which fall in the shaded region can decay to a $K\bar{K}$ pair. With the f^0 being around the $K\bar{K}$ threshold one expects daughter particles to have small relative momenta. This suggests the

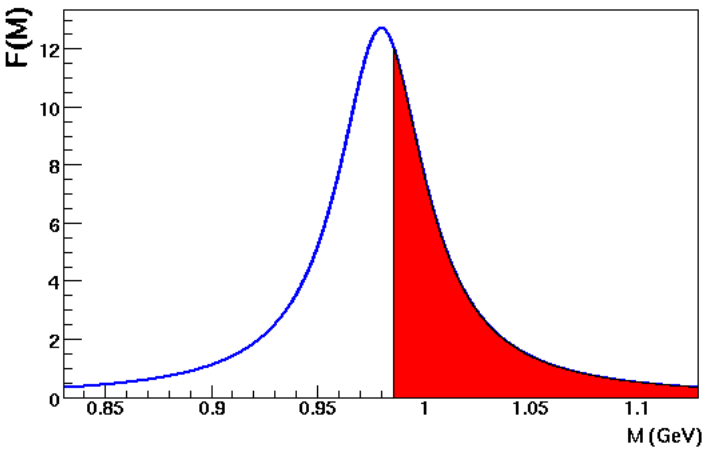

Figure 9.14: The f^0 mass distribution assuming a Briet-Wigner form.

neutral kaon correlation function may have an additional enhancement in the low q region if there is a significant production of f^0 in STAR. Since the $K\bar{K}$ threshold is higher the contribution of the f^0 is expected to be small. Still one has to consider worst case scenario based on a thermal momentum distribution for the particles.

The density of particles with rest mass m at temperature T is given by

$$n_i = \frac{g}{2\pi^2} \int_0^\infty \frac{p^2 dp}{e^{(E_i(p)-\mu_i)/T} \pm 1} \tag{9.7}$$

where $E_i(p) = \sqrt{p^2 + m^2}$. The plot in Figure (9.15) shows the ratio f^0/K_s^0 as a function of temperature assuming zero chemical potential based on the above expression.It can be seen that there is about one f^0 for every ten K_s^0 for the temperature range from 110 MeV to 170 MeV. In order to select the momentum of a particle by randomly picking a number between 0 and 1, one needs to construct a normalized

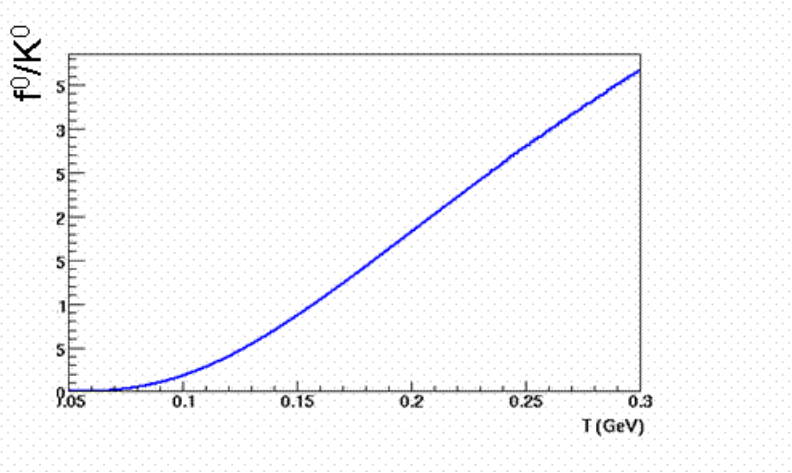

Figure 9.15: The ratio $\frac{f^0}{K_s^0}$ at $\mu = 0$ as a function of temperature.

distribution function, with p_{max} some cut off in momentum,

$$F(p) = \frac{1}{F(p_{max})} \sum_{i=1}^{p_{max}} f(p) \tag{9.8}$$

where $f(p)$ is the thermal (Bose-Einstein) momentum distribution

$$f(p) = \frac{dN}{dp} = \frac{4\pi p^2}{E} \frac{1}{e^{(E(p)-\mu)/T} - 1} \tag{9.9}$$

One generates next a random number to decide whether the f^0 decays to K^+K^- or $K_s^0K_s^0$ or $K_l^0K_l^0$. If this number is less than $\frac{1}{4}$, the particle is decayed into $K_s^0K_s^0$. The number of primary K_s^0 is kept fixed for simplicity and the f^0's are generated until $f^0/K_s^0 = c$ where $0 < c < 1$ is some specified number. Using $f(M_i)$, the Briet-Wigner mass distribution given by Eq. (9.6), the mass of the f^0 is picked by means of a normalized mass distribution function

$$F(M) = \frac{1}{F(M_n)} \sum_{i=1}^{n} f(M_i) \tag{9.10}$$

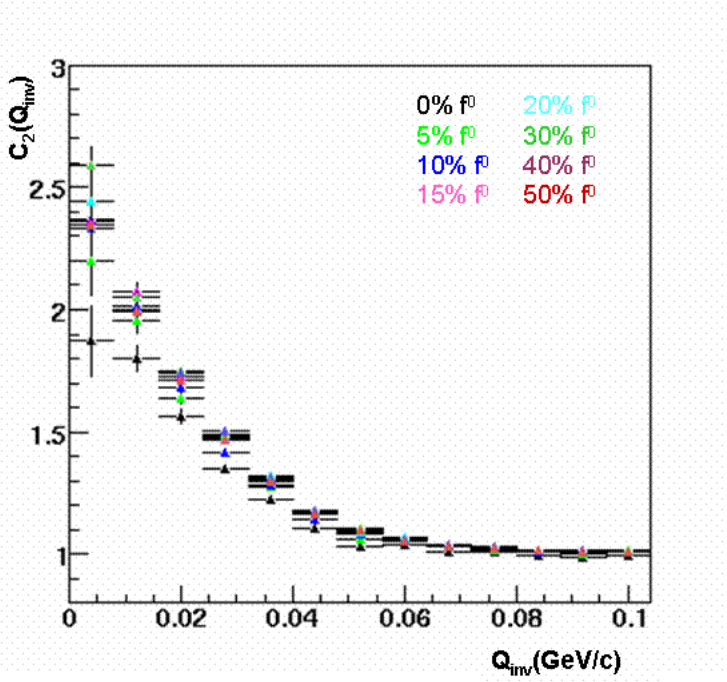

Figure 9.16: The effect of the f^0 on the neutral kaon correlation.

Since the decay K_s^0 from the same f^0 are produced at the same space-time point, there would be no Bose-Einstein correlations between them. Correlations come only from momentum conservation in this case. From the width of the f^0, we see that its lifetime ranges between τ_{min} and τ_{max} where

$$\tau_{min} = \frac{1}{100} MeV^{-1} = \frac{1}{100}(197fm) = 1.97fm$$
$$\tau_{max} = \frac{1}{40} MeV^{-1} = \frac{1}{40}(197fm) = 4.93fm \qquad (9.11)$$

This suggests that there should be Bose-Einstein correlation between the K_s^0's coming from different f^0s for the source radius we are considering which is about $6fm$. Figure (9.16) shows the correlation functions with different percentages of the f^0s added to a supposedly direct sample of neutral kaons. One can see that the correlation functions

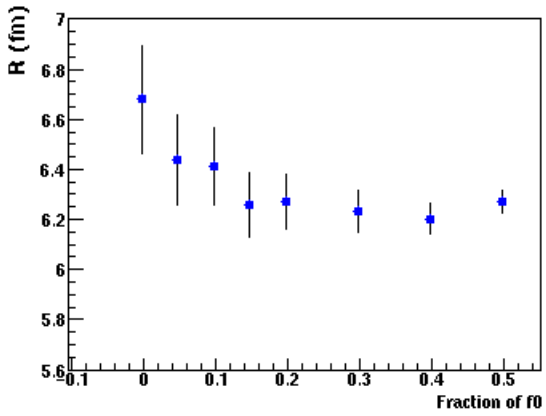

Figure 9.17: The dependence of R_{inv} on the ratio $\frac{f^0}{K^0_s}$.

are enhanced in the low Q_{inv} region due the presence of the f^0s relative to that of the pure case. The invariant radius as a function of the f^0 fraction is shown in Figure (9.17). The effect of the f^0 resonance would be to reduce the radius parameters by about 0.2 fm for $\frac{f^0}{K^0} = 10\%$

CHAPTER 10

CONCLUSIONS

Experiments at the Relativistic Heavy Ion Collider (RHIC) at the Brookhaven National Laboratory (BNL) have been studying Au-Au collisions at $\sqrt{s_{NN}} = 200$ GeV, their main objective being the creation of a new state of matter (i.e. the QGP) and carrying out a detailed investigation of its properties should one be formed. To this end the experiments at RHIC employ sophisticated detector systems to take their measurements.

Heavy ion collision experiments rely on charged particle tracking beginning with the hits they leave behind on the detectors. It is necessary to make sure that the detectors perform according to their design specifications. For the SVT detector at STAR C++ codes have been developed for a SLOW SIMULATOR which generates hits and calculates the evolution of their signals and a CLUSTER FINDER which reconstructs the hits formed by a track crossing the SVT drift detectors. The codes offer the capability to study tracking efficiency, position resolution, effects of diffusion, Coulomb repulsion, trapping and de-trapping processes.

The space time structure of the hot reaction zone and its response to a phase transition is one of the many observables being studied at RHIC. A delayed expansion as a result of a phase transition into a hadronic phase, and hence a large spatial size

and long duration of particle emission, is one of the many predicted signatures of QGP formation.

Two particle intensity interferometry provides a means of determining the space-time structure and dynamical properties of the region from which particles are emitted. The method relies on the symmetrization (anti-symmetrization) of the two particle wave function if the particles are bosons (fermions). In addition to the interference arising from this quantum statistics effect, correlations can come from final state interactions like Coulomb repulsion or strong interaction which complicates analysis of charged particle correlations.

Pion interferometry has been a particularly useful tool in correlation studies since most of the particles produced in relativistic heavy ion collisions are pions owing to their smaller mass compared to other hadrons. Resonance decays are a big problem in pion interferometry. Kaon HBT on the other hand suffers less from resonance contributions and could provide a cleaner signal for correlation studies than pions. Higher multi-particle correlation effects that might play a role for pions, should be of minor importance for kaons since the kaon density is considerably smaller than the pion density at RHIC. Kaon interferometry has become a possibility as a result of the high statistics data being made available from the RHIC collider. While one has to deal with Coulomb effects for the charged kaons, neutral kaon correlations offer an alternative over their charged particle counterparts since Coulomb effects are absent for them.

The strong interaction has been found to have an important effect on the nature of the interference correlations in the detection of pairs of neutral kaons. Using a static spherical Gaussian source as a model, a simulation of the correlations coming from the

strong interaction the K^0 and $\bar{K^0}$ particles together with Bose-Einstein interference indicates larger source sizes than is obtained with only quantum statistics.

We have presented the first measurement on neutral kaon correlations in heavy ion collisions. The value of λ is consistent with unity confirming the fact that the source is mostly chaotic as measured by STAR using three pion correlations. Our results serve as a valuable cross-check of charged pion measurements which are mainly affected by contributions from resonance decays and final state interactions. This is also an important first step towards a full 3-dimensional analysis of neutral kaon correlations as high statistics data from RHIC will be available in the near future.

One needs to make a careful measurment of the f^0 yield at RHIC in order to unambigously determine its effect on the neutral kaon correlations.

BIBLIOGRAPHY

[1] S. Weinberg, *Gravitation and Cosmology* (Wiley, New York, 1972)

[2] H. V. Klapdor-Kliengrothaus and A. Staudt, *Non-Accelerator particle physics* (IoP, London, 1998)

[3] J. Adams *et al.*, STAR collaboration, Phys. Rev. Lett. 91 (2003) 262301

[4] F. Halzn and A. D. Martin, Quarks and Leptons, John Wiley and Sons, Inc., New York (1984)

[5] I. J. R. Aitchison and A. J. G. Hey, Gauge Theories in particle physics, Adam Hilger, Bristol, England (1989)

[6] R. P. Feynmann, Phys. Rev. Lett. 23 (1969) 1415

[7] G. Miller *et al.*, Phys. Rev. D5 (1972) 528

[8] J. S. Poucher *et al.*, Phys. Rev. Lett. 32 (1974) 118

[9] J. D. Bjorken, Phys. Rev. Lett. 16 (1966)408

[10] J. D. Bjorken, Phys. Rev. 179 (1969)1547

[11] J. D. Bjorken and E. A. Paschos, Phys. Rev. 185 (1969) 1975

[12] P.V. Landshodd and J. C. Plookinghorne, Nucl. Phys. B28919710240

[13] J. Kuti and V. F. Weiskopf, Phys. Rev. D4 (1971) 3418

[14] E. Reya, Phys. Rep. 69 (1981) 195

[15] F. Wilczek, Annu. Rev. Nucl. Part. Sci. 32 (1982) 177

[16] C. N. Yang and R. L. Mills,Phys. Rev. 96 (1954) 191

[17] J. I. Friedmann and H. W. Kendall, Annu. Rev. Nucl. Sci. 22 (1972) 203

[18] D. J. Gross and F. Wilczek, Phys. Rev. D8 (1973) 3633

[19] H. D. Politzer, Phys. rep. 14 (1974) 129

[20] E V Shuryak, Sov. Phys. JETP 47 (1978) 212

[21] C. Adler *et al.*, Phys. Rev. Lett. 90 (2003) 082302, J. Adams *et al.*, STAR collaboration, Phys. Rev. Lett. 90 (2003) 032301, J. Adams *et al.*, Phys. Rev. Lett. 91 (2003) 172304

[22] K. Adox *et al.*, PHENIX Collaboration, Phys. Rev. Lett. 88 (2002) 022301, K. Adox *et al.*, PHENIX Collaboration, Phys. Lett. B 561 (2003) 82

[23] Karsch and E. Laermann, hep-lat/0305025

[24] T. Matsui and H. Satz, Phys. Lett. B178 (1986) 416

[25] M. C. Abreu, et al. (NA50 collaboration), Phys Lett. B 477 (2000) 28

[26] A. Capella, E. G. Ferreiro, and A. B. Kaidalov, Phys. Rev. Lett. 85 (2000) 2080

[27] L. Gerland *et al.*, J. Phys. G27 (2001) 695

[28] H. Satz, Rep. Prog. Phys. 63 (2000) 1511

[29] R.C. HWA and K. KAJANTIE,phys rev. D32 (1985) 1109

[30] S. Raha and B. SINHA, phys. Rev. Lett 58 (1987) 101

[31] Aggrawal, M.M., *et al.* (WA98) collaboration), Phys. Rev. Lett 85 (2000) 3595

[32] Gallmeister, K., Kampfer, B.,and Pavlenko, O. P., Phys. Rev. C62 (2000) 057901

[33] S. margetis *et al.*, Annu. rev. Nucl. Part. Sci. 50 (2000) 299

[34] P. KOCH, B. MULLER and J. Rafelski, Strangeness in Relativistic heavy ion collisions, Phys. Rep. 142 (1986) 167

[35] S. A. Volsohin and A. M. Poskanzer, Phys. Lett. B474 (2000) 27

[36] P. Kolb, J. Sollfrank, U. Heinz, preprint hep-ph/0006129

[37] J. -Y. Ollitrault, Nucl. Phys. A638 (1998) 195c

[38] D. Teany and E. Shuryak, Phys. Rev. Lett. 83 (1999) 4951

[39] P. Kolb, J. Sollfrank, U. Heinz, Phys. Lett. B459 (1999) 667

[40] H. Heiselberg and A. -M. Levy, Phys. Rev. C59 (1999) 2716

[41] M. Gyulassy and M. Plumer, Phys. Lett. B243 (1990) 432

[42] M. Gyulassy and X.-N. Wang, Nucl. Phys. B420 (1994) 583

[43] J. Dunlop *et al.*, STAR collaboration, Nucl. Phys. A698 (2002) 515c

[44] E. Shuryak, hep-ph/0312227

[45] S. Pratt, Phys Rev. D33 (1986) 72

[46] S. Pratt, Phys Rev. D33 (1986) 1314

[47] Y. Hama, S.s.Padula, Phys. Rev. D37 (1988) 3237

[48] G. F. Bertsch, Nucl Phys. A498 (1989) 173c

[49] C. Adler *et al.*,Phys. Rev. Lett. 86 (2001) 4778

[50] S. Johnson *et al.*, PHENIX Collaboration, Nucl. Phys. A698 (2002) 603

[51] T. J. Humanic, Nucl.Phys. A715 (2003) 641

[52] M. N. Harakeh *et al.*, NATO ASI Series B: Physics Vol. 359 (1997) 179

[53] H, -Thomas Elze et al New states of Matter in Hadronic Interactions, AIP conference proceedings, Vol. 631 (2002)3

[54] K. Rajagopal, AIP Conf.Proc.602:339-351,2001, Nucl. Phys. A702 (2002) 25

[55] K. G. Wilson, Phys. Rev. D10 (1974) 2445

[56] D. G. Richards, nucl-th/0006020

[57] F. Karsch, hep-ph/0106019

[58] J. Kogut and L. Susskind, Phys. Rev. D11 (1975) 395

[59] F. Karsch, E. Laermann and A. Peikert, Phys. Lett. B478 (2000) 447

[60] R. Hanbury Brown and R. Q. Twiss, Nature, 178 (1956) 1046

[61] G. Goldhaber, S. Goldhaber, W. Lee and A. Pias, Phys. Rev. 120 (1960) 300

[62] V. G. grishin, G. I. kopylov and M. I. Podgoretskii, Sov. J. Nucl. Phys. 13 (1971) 638

[63] C. -Y. Wong, Introduction to High-Energy Heavy Ion Collisions, World Scientific (1994) 431

[64] M. Gyulassy, S.K. Kauffmann, L.W. Wilson, Phys. Rev. C20 (1979) 2267

[65] U. Heinz, Correlations and clustering in subatomic physics, NATO ASI series B359 (1997) 137

[66] S. Pratt, Phys. Rev. C56 (1997) 1095

[67] M. I. Podgoretskii, Sov. J. Nucl. Phys. 37 (1983) 272

[68] S.V. Akkelin and Y. M. Sinyukov, Phys Lett B356 (1995) 525

[69] S. Chapman *et al.*, Phys. Rev. C52 (1995) 2694, U. Heinz *et al.*, Phys. Lett. B382 (1996) 181

[70] H. Heiselburg, Phys Lett B379 (1995) 27

[71] U. A. Wiedmann and U. Heinz, nucl-th/9707001

[72] M. Gell-Mann and A. Pias Phys. Rev. 97 (1955) 5

[73] G. Alexander and H.J.Lipkin, Phys. Lett. B456 (1990) 270

[74] L. Ray, private communication

[75] M. Adamczyk *et al.*, Nucl. Inst. Meth. A499 (2003) 603

[76] B. B. Back *et al.*, Nucl. Inst. Meth. A499 (2003) 437

[77] K. Adox *et al.*, Nucl. Inst. Meth. A499 (2003) 469

[78] K. H. Ackermann *et al.*, Nucl. Inst. Meth. A499 (2003) 624

[79] J.W. Harris et al, Nucl. Phys. A566 (1994) 277c

[80] K. H. Ackermann *et al.*, Nucl. Inst. Meth. A499 (2003) 766

[81] K. H. Ackermann *et al.*, Nucl. Inst. Meth. A499 (2003) 640

[82] E. Gatti et al, Nuclear Instruments and Methods in Physics Research A226 (1984) 129

[83] P. Rehak et al, Nuclear Instruments and Methods in Physics Research A248 (1986) 367

[84] E. Gatti et al, Nuclear Instruments and Methods in Physics Research A253 (1987) 393

[85] G. Lo Curto et al., STAR Note 355 (1998)

[86] V. L. Rykov et al., STAR Note 170 (1994)

[87] V. L. Rykov et al., STAR Note 170 (1994)

[88] V. L. Rykov, private communication

[89] R. bellwied *et al.*, Nuclear Instruments and Methods in Physics Research A439 (2000) 507

[90] M. Gyulassy and S. Padula, Phys. rev. C41 (1990) 21

[91] J. P. sullivan *et al.*, Phys. Rev. Lett. 70 (1993) 3000

[92] PHOBOS Collaboration, B. B. Back *et al.*,Phys. Rev. Lett. 85 (2000) 3100 ; nucl-ex/0108009

[93] STAR Collaboration, C. Adler *et al.*, Phys. Rev. Lett. 87 (2001) 082301

[94] PHENIX Collaboration, S. C. Johnson *et al.*, NUcl. Phys. A698 (2002) 603 ; W. A. Zajc *et al.*, nucl-ex/0106001

[95] C. Greiner *et al.*, Phys. Rev. Lett. 58 (1987) 1825 ; C. Spieles *et al.*, Phys. Rev. Lett. 76 (1996) 1776

[96] S. Soff *et al.*, J. Phys. G23 (1997) 2095; D. Ardouin *et al.*, Phys. Lett. B446 (1999) 191

[97] F. Antinori et al. Nucl. Phys. A661 91999) 130c

[98] G. Alexander and H.J.Lipkin, Phys. Lett. B456 (1990) 270

[99] G. Abbiendi *et al.*, OPAL Collaboration, Priprint hep-ex/0001045

[100] D. Busklic *et al.*, ALEPH Collaboration, CERN-PPE/94-74

[101] R. Lednicky and V. L. Lyuboshits, Sov. J. Nucl. Phys. 35 (1982) 770

[102] A. D. Martin, E. N. Ozmutlu and E. J. Squires, Nuclear Physics B121 (1977) 514

[103] D. Morgan and M. R. Pennington, Phys. Rev. D48 (1993) 1185

[104] Review of Particle Physics, The European Physics Journal C15 (2000) 418

[105] V. Baru *et al.*, hep-ph/0308129

[106] U. A. Wiedmann, P. Scotto, U. Heinz, Phys Rev. C53 (1996) 918

[107] T. Csorgo and B. Lorstad, Phys. Rev. C54 (1996) 1390

[108] H. Beker *et al.*, Phys. Rev. Lett. 74 (1995) 3340

[109] I. G. Bearden *et al.*, nucl-ex/0107005